UNIVERSIDAD DE CHILE
FACULTAD DE CIENCIAS FÍSICAS Y MATEMÁTICAS
DEPARTAMENTO DE GEOLOGÍA

GEOCHRONOLOGY AND GEOCHEMISTRY OF ZIRCON FROM PLUTONIC COMPLEXES OF THE COASTAL CORDILLERA IN NORTHERN CHILE

TESIS PARA OPTAR AL GRADO DE DOCTOR EN CIENCIAS, MENCIÓN GEOLOGÍA

JOSÉ JOAQUÍN MAXIMILIANO JARA DONOSO

PROFESOR GUÍA:
FERNANDO BARRA PANTOJA

PROFESOR CO-GUÍA:
MARTIN REICH MORALES

MIEMBROS DE LA COMISIÓN:
DIEGO MORATA CÉSPEDES
JOSÉ CEMBRANO PERASSO

Este trabajo ha sido financiado por los proyectos FONDECYT 1140780 y 1190105 y el Núcleo Milenio Trazadores de Metales

SANTIAGO DE CHILE
2021

RESUMEN DE LA TESIS PARA OPTAR AL GRADO DE: Doctor en Ciencias, mención Geología.
POR: José Joaquín Maximiliano Jara Donoso
FECHA: Junio 2021
PROFESOR GUÍA: Fernando Barra Pantoja

GEOCHRONOLOGY AND GEOCHEMISTRY OF ZIRCON FROM PLUTONIC COMPLEXES OF THE COASTAL CORDILLERA IN NORTHERN CHILE

The Coastal Cordillera represents the first stage of the Andean orogeny that started nearly 200 Ma ago with subduction reactivation after an anorogenic period. However, recent studies have questioned the tectonic regime of the pre-Andean cycle, proposing an uninterrupted extensional subduction since Early Carboniferous. Consequently, the nature of the pre-Andean tectonic cycle and the onset of the Andean orogeny are under debate. Moreover, even though there is strong evidence that support a multistage development of the early Andean continental arc, few works attempted to understand the petrological and geochemical changes experienced by this arc through time. The main goal of this work is to contribute to the understanding of the evolution of the early Andean Cordillera of northern Chile by identifying magmatic compositional changes using key petrological and geochemical signatures from intrusive rocks and correlate them with the tectonic changes that have been reported in previous studies to provide new insights on the Mesozoic evolution of the southwestern margin of Gondwana.

In Chapter 2, I present the first zircon U-Pb/trace element dataset of plutonic complexes from the Coastal Cordillera of northern Chile, providing new constraints on the early evolution of the Andean orogeny. The oldest event in the study area (Cerros del Vetado pluton; ~247 Ma) is interpreted as a transitional magmatism belonging to the pre-Andean tectonic cycle; a controversial result respect to recently published articles. In contrast, the following event (Quebrada Quiscuda stock; ~211 Ma) presents typical characteristics of I-type, subduction related magmatism and similar zircon geochemical signatures with Jurassic to Early Cretaceous plutons. Based on these results, I propose that the Andean orogeny started at least 10 Ma before previous estimates, i.e., at 210 Ma during the Norian stage. Our results also indicate that plutons from the first stage of the Andean orogeny (latest Triassic-Early Cretaceous) were formed from a rather depleted mantle sources in a changing subduction regime, with less evolved signatures before the transition from extensional to transtensional settings (~150-130 Ma). Following this transition, magmas became enriched possibly from subduction contributions. In Chapter 3 a more detail sampling over a larger area provides additional constraints on the magmatic evolution of the early Andean continental arc and by inference the tectonic regime that controls the magmatic activity. Expanding the study area and the findings of the previous chapter, the chemistry and ages of the zircon from the plutonic complexes allowed us to: i) reject a stable tectonic framework for this period; ii) correlate the changes in whole-rock and zircon chemistry of the samples over time with the tectonic regime; and iii) characterize the magmatic conditions of each substage in the tectonic cycle. As a result, six plutonic episodes were identified between Late Triassic and earliest Late Cretaceous (215-94 Ma), each related to particular substages in the evolution of the arc. These episodes were defined based on their geochronological and geochemical features, are better identified and characterized by their zircon petrochronology, and could be associated with tectonic changes in the continental margin. Therefore, an “external forcing” model with mantle-derived inputs is argued for the episodic plutonism of this extensional continental arc.

Finally, Chapter 4 briefly discusses and summarizes the main findings of this research and succinctly explores its potential implications for future studies.

RESUMEN DE LA TESIS PARA OPTAR AL GRADO DE: Doctor en Ciencias, mención Geología.
POR: José Joaquín Maximiliano Jara Donoso
FECHA: Junio 2021
PROFESOR GUÍA: Fernando Barra Pantoja

GEOCRONOLOGÍA Y GEOQUÍMICA DE CIRCONES DE COMPLEJOS PLUTÓNICOS DE LA CORDILLERA DE LA COSTA DEL NORTE DE CHILE

La Cordillera de la Costa representa el producto de la primera etapa de la orogénesis andina, la cual habría iniciado hace alrededor de 200 millones de años atrás con la reactivación de la subducción luego de un período anorogénico. Sin embargo, estudios recientes han cuestionado el régimen tectónico del ciclo pre-Andino, proponiendo un régimen de subducción extensional ininterrumpido desde el Carbonífero Temprano al Triásico Tardío. En consecuencia, la naturaleza del ciclo tectónico pre-Andino es un tema de debate. Más aún, a pesar de la cuantiosa evidencia que apunta a que el arco continental andino temprano se desarrollo en múltiples etapas, existen escasos trabajos para entender los cambios petrológicos y geoquímicos experimentados por éste a través del tiempo. El objetivo de esta tesis es contribuir al entendimiento de la evolución tectono-magmática de la Cordillera de la Costa del norte de Chile. Se busca identificar tendencias en las señales petrológicas y geoquímicas claves de las rocas intrusivas y correlacionarlas con los cambios tectónicos del arco continental que han sido reportados en estudios estructurales previos, para entregar nuevos antecedentes acerca de la evolución del margen suroccidental de Gondwana durante el Mesozoico.

En el Capítulo 2 se presenta la primera serie de datos de edades U-Pb y elementos traza en circones de complejos plutónicos de la Cordillera de la Costa del norte de Chile, entregando nueva evidencia sobre la evolución temprana de la orogénesis andina. El evento más antiguo en el área de estudio (plutón Cerros del Vetado; ~247 Ma) es interpretado como un magmatismo transicional del ciclo tectónico pre-Andino; un resultado controversial respecto a trabajos recientes. En contraste, el segundo evento (stock Quebrada Quiscuda; ~211 Ma) presenta típicas características de magmatismo relacionado a subducción, y similares signaturas geoquímicas en sus circones con respecto a los plutones del Jurásico y del Cretácico Temprano. Basado en estos resultados, se propone que la orogénesis andina comenzó al menos 10 millones de años antes de lo previamente estimado, alrededor de 210 millones de años atrás en el período Noriano. Los resultados también indican que los plutones de la primera etapa de la orogénesis andina se formaron a partir de una fuente mantélica relativamente deprimida en un régimen de subducción cambiante, presentándose las signaturas menos evolucionadas antes de la transición desde un régimen extensional a uno transtensional (~150-130 Ma). Luego de esta transición, los magmas se enriquecieron posiblemente producto de la contribución desde el proceso de subducción.

El Capítulo 3 profundiza nuestro entendimiento de la evolución magmática temprana del arco continental andino y del régimen tectónica responsable de la actividad magmática. Expandiendo el área de estudio y los hallazgos del capítulo previo, la química y las edades de los circones permiten: i) rechazar un marco tectónico estable para este período; ii) correlacionar los cambios tectónicos con la química de roca total y de circones en el tiempo; y iii) caracterizar las condiciones magmáticas de cada subetapa del ciclo tectónico. Como resultado, seis episodios plutónicos fueron identificados entre el Triásico Tardío y el inicio del Cretácico Tardío (215-94 Ma). Estos episodios pueden ser interpretados en términos de sus características geocronológicas y geoquímicas, son identificados y caracterizados de mejor forma por la petrocronología de circones, y pueden ser asociados a cambios significativos en el arco continental. De este modo, un modelo de "control externo" al arco con aportes derivados del manto sería el responsable del magmatismo episódico de este arco extensional.

Finalmente, el Capítulo 4 discute brevemente y resume los principales hallazgos de la investigación, y explora brevemente sus potenciales implicancias para futuros estudios.

“A mi familia”

ACKNOWLEDGEMENTS

I would like to acknowledge my advisor Professor Fernando Barra for believing in me despite my background in other areas of knowledge outside the earth sciences and supporting me during the hard times in this process. Also, I would like to thank Professor Martin Reich for his motivation and knowledge shared. Their guidance was fundamental for developing this research. In addition, I recognize professors Diego Morata and José Cembrano for their insightful comments, additional guidance, and encouragement.

My sincere appreciation also goes to Dr. Mathieu Leisen and MSc. Rurik Romero for their assistance with LA-ICP-MS analyses. I thank my fellow officemates of the "Millennium Crew" for their stimulating discussions, for their help with samples preparation and analysis, and for sharing with me part of their lives during the last years. I am also grateful to many university faculty members and staff who helped me throughout the Ph.D. I specially thank Karin Rojas, Blanca Baccola and Maritza Acuña, who gave me support and guidance throughout administrative issues.

This Ph.D. has been primarily funded by ANID through a Ph.D. scholarship and FONDECYT projects #1140780 and #1190105. Additional financial and operational support from the Millennium Nucleus for Metal Tracing Along Subduction (NMTM) is recognized.

Last but first in my thoughts, I would like to thank my family: to my kids Bauti and Maxi, their existence is all I need to go ahead in life; to my wife Cecy, my life partner who stood by me during this complex process; to my brother Sebastián, who always has believed in me; and to my parents Margarita and Raúl, who made me a curious person and shared their interest and love for understanding how the world is and works.

TABLE OF CONTENTS

TABLES INDEX

FIGURES INDEX

CHAPTER 1. INTRODUCTION

1.1. GENERAL OVERVIEW AND MOTIVATION

Continental arcs are dynamic systems were oceanic lithosphere subducts beneath continents, producing mainly an episodic magmatism driven by the hydrous melting of the mantle wedge (DeCelles et al., 2009; Grove et al., 2009; Wörner et al., 2018). These systems are important to understand several geologic processes, among them: continental growth mechanisms (Reymer and Schubert, 1984); compositional variation of batholiths (Gromet and Silver, 1987); recycling processes during subduction (Scholl and von Huene, 2007); timing of continental magmatism (DeCelles et al., 2009; Paterson and Ducea, 2015); and metallogenesis of magmatic-hydrothermal deposits (Hedenquist and Lowenstern, 1994; Blundell, 2002). In this regard, the Andean Cordillera has been key to better understand the evolution of Gondwana´s and South America's southwestern margin (Coney and Evenchick, 1994; Parada et al., 2007) and the formation of magmatic-hydrothermal ore deposits (Sillitoe, 2010; Simon et al., 2018; Sillitoe, 2008).

Traditionally, the evolution of continental arcs has been traced by the geochemical and isotopic composition of their igneous units (Pearce and Peate, 1995; Haschke et al., 2006; Kemp and Hawkesworth, 2014), which coupled to field observations and specific analyses such as geophysical and structural studies, allows to better comprehend their geologic history. Nevertheless, continental arcs are affected by post-magmatic metamorphic or metasomatic events (e.g., Barton and Hanson, 1989; Battles and Barton, 1995; Lucassen and Franz, 1996; Sorensen et al., 1998; Rossel et al., 2015), hindering the sole use of traditional whole-rock geochemical tools to this purpose. Consequently, a number of petrogenetic approaches, mostly based on the chemical composition of accessory mineral phases, have been developed (Grimes et al., 2015; Nasdala et al., 2017; Bruand et al., 2020).

The early Andean Cordillera, also known as the Coastal Cordillera, is one of three main morphotectonic provinces in Chile and is located at the western edge of South America extending for more than 1,500 km (Sernageomin, 2002). It represents the product of the first stage of the Andean orogeny that started nearly 200 Ma, with subduction reactivation after an anorogenic period triggered by the latest pre-Pangea terrane collision (Charrier et al., 2007). However, recent studies have questioned the tectonic regime of the pre-Andean cycle, alternatively proposing an uninterrupted extensional subduction setting with slab rollback and retreating of the magmatic arc to the trench between the upper Early Carboniferous to Late Triassic (Del Rey et al., 2016; 2019; Coloma et al., 2017; Oliveros et al., 2020). Consequently, the nature of the pre-Andean tectonic cycle and the timing for the onset of the early Andean continental arc are currently under debate (Oliveros et al., 2020). Additionally, the early Andean continental arc was historically thought to be formed during more than 100 million years of subduction in a rather stable extensional regime (Coira et al., 1982; Mpodozis and Ramos, 1989). However, recent structural studies have showed that during its evolution this continental arc experienced different tectonic substages due to: i) variations in the subduction angle and convergence vectors and rates in an extensional regime; or ii) changes in subduction regimes from transtensional to extensional settings with variable coupling degrees between plates (Dallmeyer et al., 1996; Scheuber and González, 1999; Grocott and Taylor, 2002; Seymour et al., 2020; and references therein).

Despite the tectonic and structural evidence supporting a multistage development of the early Andean Cordillera, few works have attempted to understand the petrological and geochemical changes experienced by this magmatic arc through time. A majority of previous

petrologic studies have focused on the isotopic composition of volcanic and intrusive units, trying to identify the characteristics of its magmatic source (e.g., Berg and Baumann, 1985; Lucassen and Thirlwall, 1998; Lucassen et al., 2006); whereas others have used traditional petrogenetic tools to understand the processes that generated particular igneous units (e.g., Rogers and Hawkesworth, 1989; Vergara et al., 1995; Parada et al., 1999; Marschik et al., 2003; Morata and Aguirre, 2003; Oliveros et al., 2007; Rodriguez et al., 2019). However, few attempts have been made to relate the composition of plutonic complexes to regional tectonic/subduction parameters.

Therefore, several questions regarding the evolution of the early Andean Cordillera are remain poorly contrained and several scientific questions remain unanswered among them:

- Are there some differences between the pre-Andean and early Andean magmatism?
- If so, what are their distinctive chemical characteritics?
- When was the early Andean continental arc established?
- Which are the geochemical characteristics of the igneous units within the early Andean Cordillera?
- Has the early Andean magmatic arc developed in a rather transient state or through episodic magmatism, as proposed for compressional continental arcs?
- What are the effects of the reported long-lasting extensional to transtensional subduction process in the magmatic source of this arc developed in an attenuated continental crust?
- Could the tectonic changes in the arc be traced by using whole-rock geochemistry of igneous units, or other geochemical proxies are necessary?

These are the main questions that are addressed in the present Ph.D. thesis.

1.2. THEORETICAL FRAMEWORK

1.2.1. Geological evolution of the Coastal Cordillera in northern Chile

The early Andean Cordillera of Chile (21°-35°S) represents a major morphotectonic domain associated with a long-lived subduction process along the southwestern margin of Gondwana (Haschke et al., 2002; Parada et al., 2007). Its magmatism is related to this convergent margin that would have started roughly 200 Ma ago and represents the onset of the Andean orogeny. This tectonic cycle pre-dates the compressional arc-orogenic system characteristic of modern Andes (Elger et al., 2005; Garzione et al., 2008), and it was developed after the Permian-Triassic anorogenic period that would have resulted from a terrane collision (terrane 'X') that led to an arrested or very slow subduction period (Mpodozis and Kay, 1992; Charrier et al., 2007). During the Jurassic to Early Cretaceous times, magmatism was produced in a variable extensional to transtensional tectonic regime associated with the oblique subduction of the cold and dense Aluk (Phoenix) plate beneath southwestern Gondwanaland (Coira et al., 1982; Scheuber and González, 1999; Parada et al., 2007). This process resulted in a rollback of the oceanic plate, retreat of the trench and thinning of the continental crust (Grocott and Taylor, 2002; Charrier et al., 2007). Consequently, plutonic complexes were emplaced into the attenuated Paleozoic basement in a series of belts parallel to the trench in the present-day Coastal Cordillera (Scheuber et al., 1994; Dallmeyer et al., 1996; Vásquez et al., 2011). As a result, back-arc (21-27°S) or intra-arc (28-35°S) basins were developed to the east, within the modern Chilean Precordillera and High Andes (Ramos, 2010; Rossel et al., 2015). These back/intra-arc areas resulted in response to the progressive thinning of the continental crust produced by the

extensional forces (Mpodozis and Ramos, 1989; Charrier et al., 2007). Most of the Jurassic volcanism was subaquatic (Vergara et al., 1995) and the intrusion of plutonic bodies thermally affected the rocks outcropping in the coastal range (Grocott et al., 1994; Dallmeyer et al., 1996). This led to variable degrees of hydrothermal alteration and/or regional low-grade metamorphism. Finally, at the end of the Early Cretaceous the arc and back/intra-arc arrangement changed to a compressional subduction setting that led to basin inversions and the migration of the magmatic arc to its present location in the main Andean Cordillera (Mpodozis and Ramos, 1989).

1.2.2. Zircon geochemistry as a petrogenetic tool in igneous environments

Most of the volcanic and plutonic units in the Coastal Cordillera have suffered variable degrees of alteration due to subsequent metasomatic and/or metamorphic processes, mobilizing some major, minor and trace elements in the process (Hervé et al., 2007). As a result, the original composition of these units has been partially or totally obliterated, limiting their petrological study by using traditional tools (Rossel et al., 2015). Under this scenario, tectonic and petrogenetic tools based on the composition of more stable minerals could be valuable to understand the tectonic and magmatic evolution of this morphotectonic domain.

Zircon is an accessory mineral phase found in igneous rocks and in some clastic sedimentary and metamorphic rocks (Finch and Hanchar, 2003). Due to its capacity to incorporate significant amounts of U anf Th over common Pb during formation, growth and/or recrystallization, it is widely recognized as a prime chronometer for geological processes (Schone, 2014). Moreover, zircon apparent simple but flexible structure ($[Zr,Hf]SiO_4$) is capable to incorporate a number of minor and trace elements, and therefore to be used in the development of new provenance and petrogenetic studies to unravel sources, growth conditions and interaction processes in different geological environments (Cherniak et al., 1997; Cherniak and Watson, 2000; Hoskin and Ireland, 2000). In particular, igneous zircons are a key repository of U, Th, Hf, Y and rare earth elements (Bea, 1996; Hoskin and Schaltegger, 2003), being the relationship between U and Th the main focus of historical provenance and genetic studies due to the routinely measurement of isotopic ratios for U-Pb geochronology (Wang et al., 2011). In addition, the relatively recent development of simultaneous geochronology/trace elements geochemistry in zircons by LA-ICP-MS (Li et a., 2000) and an increasing access to electron microprobe equipment (Breiter et al., 2014) has prompted the surge of a number of indicators to understand different aspects of tectono-magmatic and petrogenetic processes (Grimes et al., 2015; Balica et al., 2020). During the last couple of decades, zircon chemistry has been used to develop provenance tracers or tectonic discriminating indicators (e.g., Belousova et al, 2002; Grimes et al., 2007; 2015; Breiter et al., 2014; Carley et al., 2014; McKay et al., 2018), in building magmatic oxygen fugacity proxies (e.g., Ballard et al., 2002; Trail et al., 2012; Smythe and Brenan, 2016; Loucks et al., 2020) and to estimate magma crystallization temperatures (e.g., Watson et al., 2006; Ferry and Watson, 2007; Schiller and Fritz, 2019). As a result, zircon petrogenetic tools coupled with zircon U-Pb geochronology have been increasingly applied to study specific magmatic events (e.g., Claiborne et al., 2010; Carley et al., 2014; Xu et al., 2018) and the formation of magmatic-hydrothermal mineral deposits (e.g., Buret et al., 2016; Gardiner et al., 2017; Large et al., 2018; Pizarro et al., 2020), and to better understand global geological processes (e.g., Breiter et al., 2014; Grimes et al., 2015; Gao et al., 2016; McKay et al., 2018; Balica et al., 2020); although few works have attempted to integrate them in regional studies or to assess the geologic evolution of magmatic arcs (Balica et al., 2020).

1.3. CASE STUDY

This thesis focuses on the transition zone (26° to 30°S) between two segments of the Coastal Cordillera of Chile. This is an area that has been extensively studied in terms of its structural systems (e.g., Brown et al., 1993; Dallmeyer et al., 1996; Scheuber and González, 1999; Grocott and Taylor, 2002; Seymour et al., 2020), being key to the current understanding about the geodynamic evolution of the southwestern margin of Gondwana during the Mesozoic (Mpodozis and Ramos, 1989; Charrier et al., 2007; Ramos, 2010). Nevertheless, it is rather understudied in terms of the geochemical and petrological characteristics of its plutonic complexes, and in terms of the tectono-magmatic evolution of the continental arc. Limited and somewhat outdated geological and geochronological data (mainly K-Ar and $^{40}Ar/Ar^{39}$ in hornblende, biotite or whole-rock) for this part of the coastal range is available in maps and reports from the National Geological and Mining Service of Chile (Sernageomin by its Spanish acronym). On the other hand, data on the petrological and geochemical characteristics of its intrusive rocks is scarce. Most of previous petrologic research in the Coastal Cordillera have dealt with the isotopic nature of the magmatic source in the early Andean continental arc (e.g., Berg and Baumann, 1985; Lucassen and Thirlwall, 1998; Lucassen et al., 2006) and/or the study of particular igneous units north (e.g., Lucassen and Franz, 1994; Kramer et al., 2005; Oliveros et al., 2007) within (Marschik et al., 2003; Girardi, 2014) or south (e.g., Vergara et al., 1995; Parada et al., 1999; Morata and Aguirre, 2003; Vásquez et al., 2011) of the study area. This situation provides a unique opportunity to explore the relationship between magmatic processes and tectonic changes during a long period in an area thought to be representative of this morphotectonic domain. Further information on the geological background of the study area and sampling details is provided in Chapter 2 and Chapter 3.

1.4. HYPOTHESES

I. The pre-Andean and Andean magmatism of the early Andean Cordillera were generated under different tectonic regimes; the former was associated with an anorogenic period in late Permian to Late Triassic and the latter to the establishment of a continental arc in the earliest Jurassic. Therefore, they could be distinguished based on the geochemical signature of their igneous units, i.e., pre-Andean magmatism showing source enrichment and crustal inputs due to its transitional nature, and early Andean magmatism having a more depleted mantle source and scarce crustal contribution related to its extensional subduction origin.

II. The early Andean Cordillera of northern Chile was formed during a multistage extensional to transtensional subduction setting that led to episodic magmatism. These changes in subduction parameters and/or regimes are reflected in the whole-rock geochemistry and zircon petrochronology of its plutonic rocks. As a result, Jurassic units show an increasingly depleted mantle source and diminishing subduction contribution, whereas Early Cretaceous ones present a depleted mantle source that was gradually enriched by sediment melts and slab derived fluids after the transition from an arc-normal extensional to an oblique transtensional tectonic regime.

1.5. OBJECTIVE OF THE THESIS

The main goal of this thesis is to contribute to the understanding of the tectono-magmatic evolution of the early Andean Cordillera of northern Chile between 26°-30°S by using traditional

whole-rock geochemical data and applying a zircon petrochronology approach. The aim is to identify the temporal trends in key petrological and geochemical signals from its intrusive rocks and correlate them with the tectonic changes that have been reported in previous structural studies to better constrain the evolution of southwestern margin of Gondwana during the Mesozoic.

1.5.1. Specific goals

I. Constrain the onset of the early Andean Cordillera in the study area, based on the relationship between new zircon U-Pb geochronological data and geochemical evidence obtained from intrusive units of the pre-Andean and early Andean tectonic cycles.
II. Reappraise the periodic emplacement of plutons along adjacent trench-parallel belts with eastward decreasing ages in the early Andean Cordillera.
III. Establish the petrogenetic processes that generated the intrusive rocks in the study area.
IV. Evaluate the correspondence between whole-rock and zircon geochemical signatures of intrusive units of the study area and the changes in the tectonic setting during the development of the different plutonic pulses in the Coastal Cordillera.
V. Assess the nature of the episodic magmatism in the early Andean Cordillera and contrast it with the sources of cyclical magmatism in other continental arcs developed under compressional tectonic settings.

1.6. THESIS STRUCTURE

This thesis is divided in four chapters and one appendix:

Chapter I states the motivation and research questions to be addressed in this research. It also provides a general overview of the research problem, geological background, and presents the hypothesis, objectives and methods.

Chapter II provides whole-rock and zircon data of representative plutonic units of the pre-Andean and early Andean magmatism, providing further constraints on the onset of the Late Triassic-Early Cretaceous continental arc; and establishes the petrogenetic processes that generated the intrusive units of the early Andean Cordillera assessing the nature of its magmatism. These outcomes are based on the analysis of the first comprehensive record of U-Pb ages and geochemistry of zircon from plutonic complexes of the early Andean Cordillera. This chapter was published in Gondwana Research.

Chapter III assesses the evolution of the extensional early Andean continental arc by correlating the new geochronologic and trace element analyses of zircon from plutonic complexes with the current structural and tectonic knowledge of the Coastal Cordillera. This chapter was *submitted* for publication in Nature Communications.

Chapter IV summarizes the findings of this research and its major implications.

1.7. BIBLIOGRAPHY

Balica, C., Ducea, M. N., Gehrels, G. E., Kirk, J., Roban, R. D., Luffi, P., Chapman, J. B., Triantafyllou, A., Guo, J., Stoica, A. M., Ruiz, J., Balintoni, I., Profeta, L., Hoffman, D. and Petrescu, L. (2020). A zircon petrochronologic view on granitoids and continental evolution. Earth and Planetary Science Letters **531**, 116005.

Ballard, J.R., Palin, M.J. and Campbell, I.H. (2002). Relative oxidation states of magmas inferred from Ce(IV)/Ce(III) in zircon: application to porphyry copper deposits of northern Chile. Contributions to Mineralogy and Petrology **144**, 347-364.

Barton, M.D. and Hanson, R.B. (1989). Magmatism and the development of low-pressure metamorphic belts: Implications from the western United States and thermal modeling. Geological Society of America Bulletin **101**, 1051-1065.

Battles, D. A. and Barton, M. D. (1995). Arc-related sodic hydrothermal alteration in the western U. S. Geology **23**, 913-916.

Bea, F. (1996). Residence of REE, Y, Th and U in granites and crustal protoliths; implications for the chemistry of crustal melts. Journal of Petrology **37**, 521-552.

Belousova, E.A., Griffin, W.L., O'Reilly, S.Y. and Fisher, N.J. (2002). Igneous zircon: trace element composition as an indicator of source rock type. Contribution in Mineralogy and Petrology **143**, 602-622.

Berg, K. and Baumann, A. (1985). Plutonic and metasedimentary rocks from the Coastal Range of northern Chile: Rb-Sr and U-Pb systematic. Earth and Planetary Science Letters **75**, 101-115

Blundell, D.J. (2002). The timing and location of major ore deposits in an evolving orogen: the geodynamic context. In Blundell, D.J., Neubauer, F. and von Quadt, A., eds., The timing and location of major ore deposits in an evolving orogen: London. The Geological Society, 1-12.

Breiter, K., Lamarão, C.N., Borges, R.M.K. and Dall'Agnol, R. (2014). Chemical characteristics of zircon from A-type granites and comparison to zircon of S-type granites. Lithos **192-195**, 208-225.

Bruand, E., Fowler, M., Storey, C., Laurent, O., Antoine, C., Guitreau, M., Heilimo, E. and Nebel, O. (2020). Accessory mineral constraints on crustal evolution: elemental fingerprints for magma discrimination. Geochemical perspectives Letters **13**, 7-12.

Buret, Y., von Quadt, A., Heinrich, C., Selby, D., Wälle, M. and Peytcheva, I. (2016). From a long-lived upper-crustal magma chamber to rapid porphyry copper emplacement: reading the geochemistry of zircon crystals at Bajo de la Alumbrera (NW Argentina). Earth and Planetary Science Letters **450**, 120-131.

Carley, T.L., Miller, C.F., Wooden, J.L., Padilla, A.J., Schmitt, A.K., Economos, R.C., Bindeman, I.N. and Jordan, B.T. (2014). Iceland is not a magmatic analog for the Hadean: Evidence from the zircon record. Earth and Planetary Science Letters **405**, 85-97.

Charrier, R., Pinto, L. and Rodríguez, M. P. (2007). Tectonostratigraphic evolution of the Andean Orogen in Chile. In Moreno, T., and Gibbons, W., eds., The geology of Chile: London. The Geological Society, 21-114.

Cherniak, D.J., Hanchar, J.M. and Watson, E.B. (1997). Rare-earth diffusion in zircon. Chemical Geology **134**, 289-301.

Cherniak, D.J. and Watson, E.B. (2000). Pb diffusion in zircon. Chemical Geology **172**, 5-24.

Claiborne, L.L, Miller, C.F., Flanagan, D.M., Clynne, M.A. and Wooden, J.L. (2010). Zircon reveals protracted magma storage and recycling beneath Mount St. Helens. Geology **38**, 1011-1014.

Coira, B., Davidson, J., Mpodozis, C. and Ramos, V. (1982). Tectonic and magmatic evolution of the Andes of northern Argentina and Chile. Earth Science Reviews **18**, 303-332.

Coloma, F., Valin, X., Oliveros, V., Vásquez, P., Creixell, C., Salazar, E. and Ducea, M.N. (2017). Andean Geology **44**, 147-178.

Coney, P. J. and Evenchick, C. A. (1994). Consolidation of the American Cordilleras. Journal of South American Earth Sciences **7**, 241-262.

Dallmeyer, R.D., Brown, M., Grocott, J., Taylor, G. and Treloar, P. (1996). Mesozoic magmatic and tectonic events within the Andean plate boundary zone, north Chile: constraints from $^{40}Ar/^{39}Ar$ minerals ages. Journal of Geology **104**, 19-40

DeCelles, P. G., Ducea, M.N., Kapp, K, and Zandt, G. (2009). Cyclicity in cordilleran orogenic systems. Nature Geoscience **2**, 251-257.

Del Rey, A., Arriagada, C., Dekart, K. and Martínez, F. (2016). Resolving the paradigm of the late Paleozoic-Triassic Chilean magmatism: Isotopic approach. Gondwana Research **37**, 172-181.

Del Rey, Dekart, K., Planavsky, N., A., Arriagada, C. and Martínez, F. (2019). Tectonic evolution of the southwestern margin of Pangea and its global implications: Evidence from the mid Permian–Triassic magmatism along the Chilean-Argentine border. Gondwana Research **76**, 303-321.

Elger, K., Oncken, O. and Glodny, J. (2005). Plateau-style accumulation of deformation: Southern Altiplano. Tectonics **24**, TC4020.

Ferry, J.M. and Watson, E.B. (2007). New thermodynamic models and revised calibrations for the Ti-in-zircon and Zr-in-rutile thermometers. Contributions in Mineralogy and Petrology **154**, 429-437.

Finch, R.J. and Hanchar, J.M. (2003). Structure and chemistry of zircon and zircon group minerals. Reviews in Mineralogy and Geochemistry **53**, 1-25.

Gao, P., Zheng, Y.-F. and Zhao, Z.F. (2016). Distinction between S-type and peraluminous I-type granites: Zircon versus whole-rock geochemistry. Lithos **258-259**, 77-91.

Gardiner, N.J., Hawkesworth, C.J., Robb, L.J., Whitehouse, M.J., Roberts, N.M., Kirkland, C.L., Evans, N.J., 2017. Contrasting Granite Metallogeny through the Zircon Record: A Case Study from Myanmar. Scientific Reports 7, 748.

Garzione, C. N., Hoke, G. D., Libarkin, J. C., Withers, S., MacFaddon, B., Eiler, J., Ghosh, P., and Mulch, A. (2008). Rise of the Andes. Science **320**, 1304-1307.

Grimes, C.B., John, B.E., Kelemen, P.B., Mazdab, F., Wooden, J.L., Cheadle, M.J., Hanghøj, K. and Schwartz, J.J. (2007). The trace element chemistry of zircons from oceanic crust: a method for distinguishing detrital zircon provenance. Geology **35**, 643-646.

Grimes, C.B., Wooden, J.L., Cheadle, M.J. and John, B.E. (2015). "Fingerprinting" tectono-magmatic provenance using trace elements in igneous zircon. Contributions in Mineralogy and Petrology **170**, 1-26.

Grocott, J., Brown, M., Dallmeyer, R., Taylor, G. and Treloar, P. (1994). Mechanisms of continental growth in extensional arcs: an example from the Andean plate boundary zone. Geology **22**, 391-394.

Grocott, J. and Taylor, G.K. (2002). Magmatic arc fault systems, deformation partitioning and emplacement of granitic complexes in the Coastal Cordillera, northern Chilean Andes (25°30'S to 27°00'S). Journal of the Geological Society of London **159**, 425-442.

Gromet, L. P. and Silver, L. T. (1987). REE variations across the Peninsular Ranges Batholith; implications for batholithic petrogenesis and crustal growth in magmatic arcs. Journal of Petrology **28**, 75-125.

Grove, T. L., Till, C. B., Lev, E., Chatterjee, N. and Médard, E. (2009). Kinematic variables and water transport control the formation and location of arc volcanoes. Nature **459**, 694-697.

Haschke, M., Günther, A., Melnick, D., Echtler, H., Reutter, K.J., Scheuber, E. and Oncken, O. (2006). Andean tectonic evolution inferred from spatial and temporal variations in arc magmatism. In: Oncken O, Chong G, Franz G, Giese P, Götze HJ, Ramos VA, Strecker MR, Wigger P (eds) The Andes—active subduction orogeny. Frontiers in Earth Sciences. Springer: Berlin.

Haschke, M., Siebel, W., Guenther, A. and Scheuber, E. (2002). Repeated crustal thickening and recycling during the Andean Orogeny in North Chile (21°-26°S). Journal of Geophysical Research **107**, B1.

Hedenquist, J.W. and Lowenstern, J.B. (1994). The role of magmas in the formation of hydrothermal ore deposits. Nature **370**, 519-527.

Hervé, F., Faúndez, V., Calderón, M., Massone, H. and Willner, A. (2007). Metamorphic and plutonic basement complexes. In The Geology of Chile, Gibbons, W., Moreno, T., eds. The Geological Society, Special Publication, 5-19. London.

Hoskin, P.W.O. and Ireland, T.R. (2000). Rare earth element chemistry of zircon and its use as a provenance indicator. Geology **28**, 627-630.

Hoskin, P.W.O. and Schaltegger, U. (2003). The composition of zircon and igneous and metamorphic petrogenesis. Reviews in Mineralogy and Geochemistry **53**, 27-62.

Kemp, A.I.S. and Hawkesworth, C.J. (2014). Growth and Differentiation of the Continental Crust from Isotope Studies of Accessory Minerals. In Holland, H. and Turekian, K. "Treatise on Geochemistry, 2nd Edition", **4**, 379-421. Elsevier.

Large, S. J. E., von Quadt, A., Wotzlaw, J.-F., Guillong, M., and Heinrich, C. A. (2018). Magma Evolution Leading to Porphyry Au-Cu Mineralization at the Ok Tedi Deposit, Papua New Guinea: Trace Element Geochemistry and High-Precision Geochronology of Igneous Zircon, Economic Geology **113**, 39-61.

Li, X., Liang, X., Sun, M., Liu, Y. and Tu, X. (2000). Geochronology and geochemistry of single-grain zircons: simultaneous in-situ analysis of U-Pb age and trace elements by LAM-ICP-MS. European Journal of Mineralogy **12**, 1015-1024.

Loucks, R.R., Fiorentini, M.L. and Henríquez, G.J. (2020). New magmatic oxybarometer using trace elements in zircon. Journal of Petrology **61**, egaa034.

Lucassen, F. and Franz, G. (1996). Magmatic arc metamorphism: Petrology and temperature history of metabasic rocks in the Coastal Cordillera of northern Chile. Journal of Metamorphic Geology **14**, 249-265.

Lucassen F. and Thirlwall, M.F. (1998). Sm–Nd formation ages and mineral ages in metabasites from the Coastal Cordillera, northern Chile. Geological Rundschau **86**, 767-774.

Lucassen, F., Kramer, W., Bartsch, V., Wilke, H.G., Franz, G., Romer, R.L. and Dulski, P. (2006). Nd, Pb and Sr isotope composition of juvenile magmatism in the Mesozoic large magmatic province of northern Chile (18°-27°S): indications for a uniform subarc mantle. Contributions to Mineralogy and Petrology **152**, 571-589.

Marschik, R., Fontignie, D., Chiaradia, M. and Voldet, P. (2003). Geochemical and Sr–Nd–Pb–O isotope composition of granitoids of the Early Cretaceous Copiapó plutonic complex (27°30'S), Chile. Journal of South American Earth Science **16**, 381-398.

McKay, M. P., Jackson, W.T., Jr. and Hessler, A. (2018). Tectonic stress regime recorded by zircon Th/U. Gondwana Research **57**, 1-9.

Morata, D. and Aguirre, L. (2003). Extensional Lower Cretaceous volcanism in the Coastal Range (29°20'-30°S), Chile: geochemistry and petrogenesis. Journal of South American Earth Sciences **16**, 459-476.

Mpodozis C. and Ramos V.A. (1989). The Andes of Chile and Argentina. In Geology of the Andes and its Relation to Hydrocarbon and Mineral Resources, Ericksen, G.E., Cañas-Pinochet, M.T., Reinemud, J.A. (eds). Circumpacific Council for Energy and Mineral Resources. Earth Sciences Series **11**, 59-90. Houston, Texas.

Mpodozis, C. and Kay, S.M. (1992). Late Paleozoic to Triassic evolution of the Gondwana margin, evidence from Chilean Frontal Cordillera batholiths (28°S to 31°S). The Geological Society of America, Bulletin **104**, 999-1014.

Nasdala, L., Broska, I., Harlov, D.E. and Macdonald, R. (2017). Recent progress in the study of accessory minerals. Mineralogy and Petrology **111**, 431-433.

Oliveros, V., Morata, D., Aguirre, L., Féraud, G. and Fornari, M. (2007). Jurassic to Early Cretaceous subduction-related magmatism in the Coastal Cordillera of northern Chile (18°30'-24°S): geochemistry and petrogenesis. Revista Geológica de Chile **34**, 209-232.

Oliveros, V., Vásquez, P., Creixell, C., Lucassen, F., Ducea, M.N., Ciocca, I., González, J., Espinoza, M., Salazar, E., Coloma, F. and Kasemann, S.A. (2020). Lithospheric evolution of the Pre- and Early Andean convergent margin, Chile. Gondwana Research **80**, 202-227.

Parada, M.A., Nystrom, I. and Levi, B. (1999). Multiple sources for the Coastal batholith of central Chile (31-34°S): geochemical and Sr-Nd isotopic evidence and tectonic implications. Lithos **46**, 505-521.

Parada, M. A., López-Escobar, L., Oliveros, V., Fuentes, F., Morata, D., Calderon, M., Aguirre, L., Féraud, G., Espinoza, F., Moreno, H., Figueroa, O., Muñoz-Bravo, J., Troncosco-Vásquez, R. and Stern, C. R. (2007). Andean magmatism. In Moreno, T. and Gibbons, W., eds., The geology of Chile: London. The Geological Society, 115-146.

Paterson, S.R. and Ducea, M.N. (2015). Arc magmatic tempos: Gathering the evidence. Elements **11**, 91-98.

Pearce, J.A. and Peate, D.W. (1995). Tectonic implications of the composition of volcanic arc magmas. Annual Review of Earth and Planetary Science **23**, 251-285.

Pizarro, H., Campos, E., Bouzari, F., Rousse, S., Bissig, T., Grégoire, M. and Riquelme, R. (2020). Porphyry Indicator Zircons (PIZs): Application to exploration of Porphyry Copper Deposits. Ore Geology Reviews **126**, 103771.

Ramos, V.A. (2010). The tectonic regime along the Andes: present-day and Mesozoic regimes. Geological Journal **45**, 2-25.

Reymer, A. and Schubert, G. (1984). Phanerozoic addition rates to the continental crust and crustal growth. Tectonics **3**, 63-77.

Rodríguez, N., Díaz-Alvarado, J., Fernández, C., Fuentes, P., Breitkreuz, C. and Tassinari, C.C.G. (2019). The significance of U-Pb zircon ages in zoned plutons - the case of the Flamenco pluton, Coastal Range batholith, northern Chile. Geoscience Frontiers **10**, 1073-1099.

Rogers, G. and Hawkesworth, C.J. (1989). A geochemical traverse across the North Chilean Andes: evidence for crust generation from the mantle wedge. Earth and Planetary Science Letters **91**, 271–285.

Rossel, P., Oliveros, V., Ducea, M. and Hernandez, L. (2015). Across and along arc geochemical variations in altered volcanic rocks: Evidence from mineral chemistry of Jurassic lavas in northern Chile, and tectonic implications. Lithos **239**, 97-113.

Scheuber, E., Bogdanic C., T., Jensen, A. I., and Reutter, K. J. (1994). Tectonic development of the North Chilean Andes in relation to plate convergence and magmatism since the Jurassic. In Reutter, K. J., Scheuber, E., and Wigger, P. J., eds., Tectonics of the southern

Central Andes; structure and evolution of an active continental margin: Berlin. Springer-Verlag, 121-139.

Scheuber, E. and González, G. (1999). Tectonics of the Jurassic-Early Cretaceous magmatic arc of the north Chilean Coastal Cordillera (22°-26°S): A story of crustal deformation along a convergent plate boundary. Tectonics **18**, 895-910.

Schiller, D. and Fritz, F. (2019). Application of Ti-in-zircon thermometry to granite studies: problems and possible solutions. Contributions in Mineralogy and Petrology **174**, 51.

Schone, B. (2014). U-Th-Pb geochronology. In Treatise on Geochemistry, 2nd Edition, Holland, H. and Turekian, K. (eds.). Elsevier, 341-378.

Scholl, D. W. and von Huene, R. (2007). Crustal recycling at modern subduction zones applied to the past: Issues of growth and preservation of continental basement crust, mantle geochemistry, and supercontinent reconstruction. Geological Society of America Memoirs **200**, 9-32.

Sernageomin, 2002. Mapa geológico de Chile, 1:1.000.000. Servicio Nacional de Geología y Minería: Santiago.

Seymour, N. M., Singleton, J. S., Mavor, S. P., Gomila, R., Stockli, D. F., Heuser, G. and Arancibia, G. (2020). The relationship between magmatism and deformation along the intra-arc strike-slip Atacama fault system, northern Chile. Tectonics **39**, e2019TC005702.

Sillitoe, R.H. (2008). Special paper. Major gold deposits and belts of the North and South American Cordillera: distribution, tectonomagmatic settings, and metallogenic considerations. Economic Geology **103**, 663-688.

Sillitoe, R.H. (2010). Porphyry copper systems. Economic Geology **105**, 3-41.

Simon, A.C., Knipping, J., Reich, M., Barra, F., Deditius, A., Bilenker, L., Childress, T.A. (2018). Kiruna-type iron oxide-apatite (IOA) and iron oxide copper-gold (IOCG) deposits form by a combination of igneous and magmatic-hydrothermal processes: evidence from the Chilean Iron Belt. Society of Economic Geology, Special Publications **21**, 89-114.

Smythe, D.J. and Brenan, J.M. (2016). Magmatic oxygen fugacity estimated using zircon-melt partitioning of cerium. Earth and Planetary Science Letters **453**, 260-266.

Sorensen, S.S., Dunne, G.C., Hanson, R.B., Barton, M.D., Becker, J., Tobisch, O.T. and Fiske, R.S. (1998). From Jurassic shores to Cretaceous plutons: Geochemical evidence for paleoalteration environments of metavolcanic rocks, eastern California. GSA Bulletin **110**, 326-343.

Trail, D., Watson, E.B. and Tailby, N.D. (2012). Ce and Eu anomalies in zircon as proxies for the oxidation state of magmas. Geochimica et Cosmochimica Acta **97**, 70-87.

Vásquez, P., Glodny, J., Franz, G., Frei, D. and Romer, R.L. (2011). Early Mesozoic plutonism of the Cordillera de la Costa (34°-37°S), Chile: constraints on the onset of the Andean Orogeny. Journal of Geology **119**, 159-184.

Vergara, M., Levi, B., Nystrom, J. and Cancino, A. (1995). Jurassic and Early Cretaceous island arc volcanism, extension, and subsidence in the Coast Range of central Chile. Geological Society of America Bulletin **107**, 1427-1440.

Wang, X., Griffin,W.L., Chen, J., Huang, P. and Li, X. (2011). U and Th contents and Th/U ratios of zircon in felsic and mafic magmatic rocks: improved zircon-melt distribution coefficients. Acta Geologica Sinica **85**, 164-174.

Watson, E.B., Wark, D.A. and Thomas, J.B. (2006). Crystallization thermometers for zircon and rutile. Contributions to Mineralogy and Petrology 151, 413-433.

Wörner G., Mamani M. and Blum-Oeste, M. (2018). Magmatism in the Central Andes. Elements **14**, 237-244.

Xu, Z., Zheng, Y. and Zhao, Z (2018). Zircon evidence for incorporation of terrigenous sediments into the magma source of continental basalts. Scientific Reports **8**, 178.

CHAPTER 2. GEOCHRONOLOGY AND PETROGENESIS OF INTRUSIVE ROCKS IN THE COASTAL CORDILLERA OF NORTHERN CHILE: INSIGHTS FROM ZIRCON U-PB DATING AND TRACE ELEMENT GEOCHEMISTRY

José Joaquín Jara[1,2,3,*], Fernando Barra[1,3], Martin Reich[1,3], Diego Morata[1,3], Mathieu Leisen[1,3], Rurik Romero[1,3]

[1]Departamento de Geología y Centro de Excelencia en Geotermia de los Andes (CEGA), FCFM, Universidad de Chile, Plaza Ercilla 803, Santiago, Chile.
[2]Departamento de Ingeniería de Minería, Pontificia Universidad Católica de Chile, Av. Vicuña Mackenna 4860, Santiago, Chile.
[3]Millennium Nucleus for Metal Tracing Along Subduction, FCFM, Universidad de Chile, Plaza Ercilla 803, Santiago, Chile

(*) Corresponding author: jjjara@uc.cl
Keywords: zircon U-Pb geochronology; zircon trace element geochemistry; whole-rock geochemistry; Andean evolution; Coastal Cordillera, northern Chile.

2.1. ABSTRACT

Two models have been proposed to explain the early Andean evolution of the southwestern margin of Gondwana; a model that assumes continuous subduction-related magmatism since the Carboniferous and a second involving subduction cessation during the pre-Andean stage (~280-200 Ma) followed by subsequent reactivation at ca. 200 Ma. Here we provide new constraints regarding the onset of the Andean tectonic cycle and the transition between pre-Andean and early Andean stages (210-100 Ma) by performing a comprehensive study of the geochronology and petrogenesis of plutonic complexes from the Coastal Cordillera of northern Chile. We present the first zircon U-Pb geochronology and trace element dataset of intrusive rocks combined with whole-rock geochemistry for the early Andean stage. The oldest unit identified is a syenogranite dated at 246.7±3.9 Ma with a subduction signature, i.e., slightly peraluminous, enriched in LILE over HFSE, negative Nb-Ta and positive Pb anomalies, and strong REE fractionation, but also shows anorogenic features with an alkali-rich composition and high enrichment in rare earth and HFS elements compared to chondritic values. These characteristics are interpreted as representing a transitional, anorogenic event from the pre-Andean stage. In contrast, the second oldest magmatic event was dated at 211.4±1.2 Ma and has a chemical composition consistent with Andean-related magmatism and its zircon composition is similar to those from Late Triassic-Early Cretaceous units. Consequently, we conclude that the Andean orogeny started at ca. 210 Ma, before earlier estimates. Our study also supports works that indicate episodic high-flux magmatism and the eastward migration of the magmatic arc during the Mesozoic. Furthermore, the whole-rock Th/Yb and zircon U/Yb ratios show a trend from the Late Triassic to Late Jurassic of increasing depletion of the mantle source. However, during the Early Cretaceous more variable and enriched signatures are observed, possibly related to changes in the tectonic regime.

2.2. INTRODUCTION

Cordilleran arcs are dynamic systems formed by the subduction of oceanic lithosphere under continental crust and where hydrous melting of the metasomatized mantle wedge produces widespread magmatism of mostly intermediate to silicic composition (e.g., Grove et al., 2009; DeCelles et al., 2009; Wörner et al., 2018; among others). A comprehensive knowledge of Cordilleran arc systems is important to understand the growth and evolution of the continental crust, the compositional variation of plutonic units that form batholiths, the materials recycled during subduction processes, the episodic nature of magmatism, and the formation, temporality and location of magmatic-hydrothermal mineral deposits (e.g., Reymer and Schubert, 1984; Gromet and Silver, 1987; Hedenquist and Lowenstern, 1994; Blundell, 2002; Scholl and von Huene, 2007; DeCelles et al., 2009; Chapman and Ducea, 2019). Batholiths exposed along the Coastal Cordillera in north and central Chile provide an opportunity to unravel the tectonic and magmatic evolution of a relatively young Cordilleran arc in the southwestern Gondwana margin during the Mesozoic (Coney and Evenchick, 1994; Parada et al., 2007).

The Coastal Cordillera is a major morphotectonic unit composed mostly of Mesozoic volcanic, plutonic, and sedimentary rocks formed during the first stage of the Andean orogeny (Charrier et al., 2007). This domain has been interpreted as the result of subduction reactivation at the beginning of the Jurassic after an anorogenic event during the Triassic (Coira et al., 1982; Mpodozis and Ramos, 1990; Mpodozis and Kay, 1992). However, recent studies have questioned this framework and alternatively proposed a continuous subduction setting from latest Carboniferous to Jurassic with a retreating magmatic arc due to slab foundering and rollback during the Triassic (Del Rey et al., 2016; 2019; Coloma et al., 2017; Oliveros et al., 2017; Espinoza et al., 2019).

Several igneous units in the Coastal Cordillera of northern Chile present variable degrees of alteration due to metasomatic events related to the formation of ore deposits (Maksaev et al., 2007; 2010) and superimposed low-grade metamorphism (Hervé et al., 2007). In those cases, the primary composition of these rocks has been partially or totally modified, limiting petrological interpretations using traditional approaches (Oliveros et al., 2007; Parada et al., 2007; Rossel et al., 2015). In recent years, the development of in-situ analytical techniques such as laser ablation ICP-MS (LA-ICP-MS) on refractory mineral phases has been increasingly used to obtain precise geochronological and chemical information of magmatic systems as an alternative and/or complementary tool for traditional petrogenetic methods (e.g., Belousova et al., 2002; Grimes et al., 2015; Gao et al., 2016; Padilla et al., 2016; McKay et al., 2018; Wall et al., 2018). Zircon ($ZrSiO_4$) is ubiquitous in most intermediate to felsic igneous rocks and is highly resistant to hydrothermal alteration and to metamorphism of low- to intermediate-grade (Finch and Hanchar, 2003). Its structure can accommodate various elements, such as Hf, U, Th and REE, allowing its use as a petrogenetic indicator (Hoskin and Schaltegger, 2003; Belousova et al., 2002; Grimes et al., 2007). In addition, zircon is one of the main repositories for U in igneous systems and incorporates little or no common Pb, making it an excellent chronometer of magmatic processes (Hoskin and Schaltegger, 2003; Schoene, 2014).

The purpose of this study is to provide new insights on the evolution and onset of the Early Andean cycle by combining U-Pb geochronology and zircon trace element analyses with whole-rock geochemistry. We focus on intrusive rocks of the Coastal Cordillera between 26° and 28°S (Fig. 1), a segment which has been key to understand the structural and tectonic evolution of the Gondwana margin during the Mesozoic (Scheuber and González, 1999; Grocott and

Taylor, 2002; Seymour et al., 2020), but mostly understudied in terms of the petrogenesis and geochronology of its plutonic complexes.

2.3. GEOLOGICAL BACKGROUND

2.3.1. Tectonic setting of the Coastal Cordillera

The Coastal Cordillera of northern Chile (21°-35°S) is a major morphotectonic unit that comprises mainly Mesozoic volcanic, plutonic and sedimentary rocks, formed in a long-lived, subduction-related setting along the southwestern margin of Gondwana (Haschke et al., 2002; Parada et al., 2007). Magmatism in the Coastal Cordillerais related to the initiation of the Andean tectonic cycle, which is thought began in the Early Jurassic (Charrier et al. 2007), when subduction was reactivated after a period of rifting (Scheuber et al., 1994; Charrier et al., 2007). This magmatism was produced under various extensional and transtensional tectonic settings associated with the oblique subduction of the cold and dense Phoenix plate beneath southwestern Gondwana (Fig. 1) (Coira et al., 1982; Scheuber and González, 1999; Parada et al., 2007), which also caused the rollback of the oceanic plate, retreat of the trench and progressive thinning of the continental crust (Grocott and Taylor, 2002; Charrier et al., 2007). As a result, a series of magmatic belts parallel to the trench were formed in the present-day Coastal Cordillera and intra-arc (28°-35°S) or back-arc (21°-27°S) basins were developed to the east within the modern Chilean Precordillera and High Andes (Mpodozis and Ramos, 1990; Charrier et al., 2007; Rossel et al., 2015). The high magmatic flux rates during the Jurassic to Early Cretaceous produced thick basaltic to andesitic Middle Jurassic volcanic sequences (Rogers and Hawkesworth, 1989; Oliveros et al., 2006; 2007) and subsequent large, north-south elongated plutonic bodies (Dallmeyer et al., 1996; Parada et al., 2007). The emplacement of these plutonic bodies between the Late Jurassic and late Early Cretaceous thermally affected Middle Jurassic volcanic rocks (Grocott et al., 1994; Dallmeyer et al., 1996), which were locally altered by hydrothermal fluids or underwent regional low-grade metamorphism of sub-greenschist- to greenschist-facies (Levi et al., 1989; Aguirre et al., 1999; Oliveros et al., 2006; Parada et al. 2007).

By the late Early Cretaceous, the back- and intra-arc configuration changed to the so called “Andean-type” subduction tectonic regime, leading to basin inversions and migration of the magmatic arc to its current position in the Andes (Mpodozis and Ramos, 1990).

2.3.2. The Coastal Cordillera in the Atacama Region

Geology of the study area. In the study area (Fig. 1), the pre-Mesozoic margin is represented by a discontinuous metamorphic belt of Carboniferous to Permian age, i.e., the Chañaral Epimetamorphic Complex (Hervé et al., 2007). Scarce sedimentary sequences and intrusive bodies of Permian to Triassic age are interpreted as the products of rift-aborted basins in an extensional regime (Suárez and Bell, 1992; Charrier et al., 2007). Located near the current coastline, a discontinuous belt of Late Triassic to Early Jurassic intrusive complexes have been considered as the first products of the Andean orogeny. To the east, thick basaltic to andesitic Middle Jurassic volcanic units, such as La Negra Formation, are intruded by Late Jurassic to Early Cretaceous plutonic complexes arranged in belts parallel to the trench and with eastward decreasing ages (Dallmeyer et al., 1996; Parada et al., 2007). In addition, basaltic to andesitic volcanic and volcanoclastic rocks with minor marine strata from the Punta del Cobre Formation (Late Jurassic-Early Cretaceous), were deposited over the Middle Jurassic volcanic rocks (Marschik and Fontbote, 2001; Charrier et al., 2007). Thick carbonate sequences overlying the

Punta del Cobre Formation represent the development of a discrete marine back-arc basin during the Early Cretaceous (Chañarcillo Basin; Martínez et al., 2013). Lastly, an extensional event of Albian to Cenomanian age (~102 to 98 Ma) led to subsidence and the development of aborted marginal basins, which are represented by volcanic and sedimentary rocks formed in a continental environment (e.g., Cerrillos Formation; Mpodozis and Allmendinger, 1993; Charrier et al., 2007).

The main structural feature in the study area is the Atacama Fault System (AFS; Fig. 1), a major structure that extends along the main axis of the Coastal Cordillera and has been active intermittently at least since Middle to Late Jurassic times (Grocott et al., 1994; Seymour et al., 2020). The AFS comprises several structures in concave segments with mainly sinistral strike slip movements and variable extension or shortening periods (Scheuber and Andriessen, 1990; Brown et al., 1993; Seymour et al., 2020). In the study area, Grocott and Taylor (2002) estimated a main transition from normal to strike-slip activity of the AFS at ca. 132 Ma, and Dallmeyer et al. (1996) between 130 and 125 Ma; however, some authors suggested a transition during the Late Jurassic (~150 Ma), at least for the northern section of the AFS (Scheuber et al., 1995; Scheuber and González, 1999). This stage of slip movements would have ceased ca. 110 Ma, coincidentally with the eastward migration of the magmatic arc (Seymour et al., 2020).

Plutonic complexes in the study area. Several plutonic complexes are present in the area. In this section we provide a brief description of the studied complexes indicating main lithologies and reported radiometric ages (Table 2.1). The oldest pluton in the study area is the Cerros del Vetado pluton located 15 km from the coast of Chañaral (Fig. 1). This stock has a leucocratic monzo- to syenogranite composition and a reported U-Pb age of 217±12 Ma (Berg and Baumann, 1985). More recently, Maksaev et al. (2014) dated two samples by using SHRIMP zircon U-Pb geochronology obtaining ages of 237.0±4.0 Ma for a biotite-bearing monzogranite sample and 246.5±4.0 Ma for a leucocratic syenogranite with biotite, muscovite and minor amphibole.

Along the coast of Chañaral, four plutonic units were selected. The Barquito complex comprises a small group of plutons with granodiorite to monzogranite compositions located a few km south of Chañaral (Fig. 1). Previous K-Ar dates of biotite and a Rb-Sr whole-rock isochron yielded ages between 204 and 193 Ma (Godoy and Lara, 1998). The Flamenco stock, located 20 km south of Chañaral, is a subcircular body composed mainly by granodiorites with pyroxene, amphibole and biotite. Several radiometric ages, including zircon U-Pb, $^{40}Ar/^{39}Ar$ and K-Ar of biotite and amphibole, and Rb-Sr isochron ages, ranging from 202±4 to 182±5.4 Ma have been reported (Godoy and Lara, 1999). The Relincho intrusive, located 35 km south of Chañaral, has a similar morphology and composition as the Flamenco unit. Reported biotite and amphibole $^{40}Ar/^{39}Ar$ and K-Ar, and Rb-Sr isochron ages for Relincho range between 193 and 189 Ma (Godoy and Lara, 1999). The Quebrada Quiscuda, a granitic stock situated near the coastline north of Chañaral has not been previously dated.

Plutonic complexes east of Chañaral include Las Ánimas, Las Tazas and Sierra Áspera. Las Ánimas complex is an elongated, north-south oriented body and includes two-pyroxene quartz diorites and subordinated microdiorites and tonalites. This stock was emplaced to the east of the Permian-Triassic Chañaral Epimetamorphic Complex (Fig. 1) and to the west of the AFS, at ca. 160-150 Ma (several methods; Vivallo et al., 2008). Further east, Las Tazas plutonic complex is a tabular, granodioritic body with amphibole and biotite that has reported ages of 133±2 Ma ($^{40}Ar/^{39}Ar$ in amphibole; Dallmeyer et al., 1996), 128.7±2.8 Ma (Rb-Sr isochron;

Godoy and Lara, 1998), and 132.1±1.9 Ma (U-Pb in zircon; Seymour et al., 2020). The easternmost Sierra Áspera complex, an irregular unit composed mostly of pyroxene-bearing diorites was emplaced between 130 and 125 Ma based on biotite K-Ar and Rb-Sr isochron ages (Godoy and Lara, 1998).

Several Early Cretaceous plutonic complexes are present near the city of Copiapó (Fig. 1); among them Sierra Chicharra, La Brea Diorite, La Borracha, Sierra Atacama Diorite, and Sierra Pajas Blancas Granodiorite. The oldest unit is the Sierra Chicharra complex, a north-northeast elongated unit composed of quartz diorites with amphibole and biotite and minor tonalites and granodiorites. Previous K-Ar and $^{40}Ar/^{39}Ar$ dating of amphibole and biotite places its age between 128 and 125 Ma (Arévalo, 2005a). La Brea Diorite, situated northeast of Sierra Chicharra and along the main trace of the AFS, is composed of clinopyroxene and amphibole-bearing diorites with K-Ar ages of 123±4 (amphibole) and 119±3 Ma (biotite) (Arévalo, 2005a,b). La Borracha pluton is in fault contact with La Brea Diorite and comprises quartz monzodiorites and quartz monzonites with amphibole and minor biotite; minor monzogranites and diorites have also been described. Several amphibole and biotite K-Ar ages have been published (Arévalo, 2005a), ranging from 114 to 103 Ma. Sierra Atacama Diorite is a N-S elongated pluton composed of diorites, quartz diorites and monzodiorites with clinopyroxene, amphibole and biotite. Two previous $^{40}Ar/^{39}Ar$ biotite ages of 116.8±0.8 (Blanco et al., 2003) and 104.0±0.6 Ma (Arévalo, 2005a,b) constrained its age to the late Early Cretaceous. The Sierra Pajas Blancas complex includes a series of irregular stocks of amphibole and biotite-bearing granodiorites, with minor granites and quartz monzodiorites that intruded the Sierra Chicharra and La Brea plutons between 108±3 and 103±3 Ma (biotite K-Ar ages; Arévalo, 2005a).

2.4. SAMPLES AND METHODS

Sampling of outcropping plutonic rocks was carried out for whole-rock composition as well as zircon U-Pb geochronology and trace element concentration analyses. Sampling considered three main groups of samples chosen to represent the diversity of plutonic complexes in the study area: (1) a W-E transect across the Coastal Cordillera near Chañaral (26°20'S; Fig. 1), which included 10 zircon and 6 whole-rock samples; (2) selected plutons of Late Triassic to Late Jurassic age (3 zircon and 2 whole-rock samples); and (3) an extensive sampling of Early Cretaceous plutonic rocks that involved 17 zircon and 8 whole-rock samples. About 5 to 15 kg were collected at each site. Sample locations are shown in Figure 1 and detailed in Table 2.2.

All samples were first studied by polarized light microscopy to determine the modal mineralogy and the degree of alteration. Samples were later processed for mineral separation, but only those less altered were selected for whole-rock composition analyses. Whole-rock analyses were performed at the GeoAnalytical Laboratory, Washington State University, USA. A description of their methods is provided in the SM1 file. Clean, unaltered rock chips (100 to 300 g) were ground in an agate mill. Concentrations of major and minor elements were determined by XRF, whereas trace elements were determined using ICP-MS.

Approximately 5 to 10 kg of sample were processed for zircon mineral separation by conventional procedures at the Department of Geology, University of Chile. Crushing and grinding were carried out using a jaw crusher and a disc mill, followed by sieving. Heavy, non-magnetic mineral concentrates were obtained by using gravity and magnetic separation methods. Approximately 100 zircon grains per sample were handpicked under a binocular microscope and mounted in epoxy resin. Plešovice (Sláma et al., 2008) or SL2 (Gehrels et al., 2008) reference

materials were used as a primary standard and SL2 or 91500 (Wiedenbeck et al., 1995) as a secondary standard for geochronology purposes, whereas the USGS NIST 610 was used as a primary standard for trace element measurements. Mounts were polished before analysis at the CEGA Mass Spectrometry Laboratory, University of Chile. Cathodoluminescence (CL) images of zircon crystals were obtained by using a FEI Quanta 250 scanning electron microscope (SEM) coupled with a Centaurus sensor. These images were used to assess the internal structure of zircon crystals. Simultaneous U-Pb geochronology and trace element concentrations were performed by laser ablation, inductively coupled plasma mass spectrometry (LA-ICP-MS). Analyses were conducted by using an Analyte G2 193 nm ArF excimer laser ablation system coupled to a iCAP-Q ICP-MS. Detailed analytical procedures and data reduction are described in Liu et al. (2010) and are briefly summarized here. A spot size of 50 μm was used to be able to run coupled U-Pb dating and trace element analyses. Each analysis comprised 20 s of background measurement followed by 50 s of data acquisition. The time-dependent drifts of U-Pb isotopic ratios and trace elements concentrations were corrected using a linear or exponential interpolation for every 5 and every 15 analyses, respectively. The reproducibility of the U-Pb geochronology was evaluated by comparison with the secondary reference material (Wiedenbeck et al., 1995). Off-line selection and integration of signals, time-drift corrections and quantitative calibrations were performed using Iolite (Paton et al., 2011). Concordia diagrams and weighted mean calculations were constructed using Isoplot 4.0 (Ludwig, 2010). Uncertainties of individual analyses are quoted at the 2σ confidence level and include measured and propagated errors.

2.5. RESULTS

Modal composition determined by petrographic studies and the $^{206}U/^{238}Pb$ weighted mean age of the main rock types of the plutonic units are summarized in Table 2.2. U-Pb and trace element data for all zircon grains (n=1163) are reported in the Table SM2. Samples selected for zircon U-Pb geochronology/trace element geochemistry as well as whole-rock composition analyses (n=16) are highlighted in Table 2.2 and differentiated from those for which only zircon U-Pb dating and elemental analysis (n=14) were performed.

Studied samples mostly include diorites (n=9) and granodiorites (n=14), with rare monzogranites (n=3), monzodiorites (n=2), syenogranites (n=1) and gabbros (n=1). Plagioclase, hornblende and quartz are the main mineralogical components of the intrusive rocks (Table 2.2). Biotite is present in some units as a minor phase and clinopyroxene is commonly partially replaced by hornblende. Titanite and magnetite are common accessory minerals. Most samples show granular phaneritic textures, but porphyritic textures are also observed. No evidence of deformation was observed in the samples. When present, alteration is minor and represented by selective replacement of mafic minerals by chlorite, actinolite and/or epidote, and scarce albitization or sericitization of plagioclase. The only exception is a sample from sierra Áspera (JJJD_22), which shows moderate albitization and argilization of plagioclase and pervasive replacement of mafic minerals by secondary biotite, chlorite and epidote; thus, it is distinguished in diagrams presenting whole-rock geochemical data.

2.5.1. U-Pb geochronology

All new LA-ICP-MS zircon U–Pb ages obtained in this study are reported in Table 2.2 and shown in Figure 1. Analyzed zircon crystals are inclusion-free, mostly transparent and prismatic with sizes ranging from 50 to 500 μm, a length to width ratio between 1.0 and 5.0 reflecting typical morphologies of magmatic zircon (Corfu et al., 2003). Cathodoluminescence

(CL) images commonly reveal oscillatory zoning across the rims with homogeneous cores (Fig. 2). Spot analyses were performed on the rims of zircon grains and the obtained $^{206}Pb/^{238}U$ weighted mean value is interpreted as the crystallization age of the dated intrusion. The $^{206}Pb/^{238}U$ age is preferred over the less precise $^{207}Pb/^{206}Pb$ age for young (<1.5 Ga) zircon grains (Gehrels et al., 2008; Spencer et al., 2016). Weighted mean age plots are shown in Figure 3 for plutonic complexes of the Chañaral transect; and in Figure 4 for other intrusions. Concordia diagrams for plutonic complexes of the Chañaral transect are shown in Figure SM3.1; and in Figure SM3.2 for other intrusions.

The Cerros del Vetado syenogranite is the oldest sample in our study, with a weighted mean age of 246.7±3.9 Ma (Fig. 3A), in agreement with a previously reported SHRIMP zircon U-Pb age of 246.5±4.0 Ma (Maksaev et al., 2014), and indicating an Early to Middle Triassic age for the emplacement of this complex. Additionally, it presents four concordant zircon ages between ~320 and ~300 Ma (Fig. SM3.1A). Two Barquito samples near the coast of Chañaral (Fig. 1) were analyzed in this study. A monzogranite with biotite and amphibole that yield a weighted mean age of 202.8±1.5 Ma, which also presented one concordant zircon age of 228±12 Ma (Fig. SM3.1B) and an amphibole and biotite-bearing granodiorite dated at 189.6±1.1 Ma (Fig. 3C). These ages are broadly consistent with less precise reported ages (204-193 Ma; Table 2.1). Further east along transect (Fig. 1), the Las Ánimas sample, an amphibole diorite to quartz diorite with minor pyroxene and biotite, yield a weighted mean age of 150.2±0.6 Ma (Fig. 3D), within range of previous ages (160-150 Ma; Table 2.1). The Las Tazas (sample JJJD_19; Fig. 1) is an amphibole and biotite granodiorite dated at 131.7±0.5 Ma (Fig. 3E). The easternmost samples collected from the transect are from the Sierra Áspera complex. Five samples from this complex were analyzed: a pyroxene diorite with minor amphibole (JJJD_32: 127.5±0.4 Ma); an amphibole and pyroxene quartz monzodiorite with minor biotite (JJJD_23: 129.6±0.8 Ma); two amphibole granodiorites (JJJD_40 and JJJD_22), which yielded ages of 127.0±0.7Ma and 125.4±0.7 Ma (Fig. 3F), respectively, and one monzogranite hosting amphibole and biotite (JJJD_33: 125.5±0.8 Ma).

In addition to the samples from the Chañaral transect, nine other plutonic complexes were investigated (Table 2.2; Fig. 1). Outside the transect, the oldest sample is a biotite-bearing granodiorite from Quebrada Quiscuda, located near the coast, north of Chañaral. This pluton yielded an age of 211.3±1.2 Ma (Fig.4A). Two other plutons located along the coast were sampled: Flamenco and Relincho. The Flamenco pluton is composed by a pyroxene, amphibole and biotite-bearing granodiorite yielding a weighted mean age of 194.4±0.8 Ma, in good agreement with the main magmatic event reported for this pluton by Rodríguez et al. (2019) (SHRIMP zircon U-Pb; 195-185 Ma). A biotite and amphibole-bearing quartz diorite from Relincho was dated here at 192.4±0.9 Ma (Fig. 4B), consistent with less precise dates (193-189 Ma) published by Godoy and Lara (1999) (Table 2.1).

Several Early Cretaceous plutonic complexes were dated in this study. Two amphibole-bearing granodiorites with different textures from La Brea Diorite were sampled (JJJD_01 and JJJD_02; Fig. 1, Table 2.2). Sample JJJD_02 yielded a weighted mean age of 135.2±0.5 Ma (Fig. 4C), and sample JJJD_01 yield an age of 124.6±1.1 Ma, the latter consistent with published ages between 123-117 Ma (Arévalo, 2005a,b). Two granodiorite samples from the Sierra Chicharra complex located southwest from La Brea Diorite yield similar ages of 126.9±1.1 Ma and 125.3±1.2 Ma (Fig. 4D). These ages are also consistent with data reported by Arévalo (2005a,b) (128-125 Ma; Table 2.1).

Five new U-Pb ages for monzodiorite to quartz monzodiorite samples collected from La Borracha pluton constrained its crystallization age between 116.7±0.4 (JJJD_24) and 111.6±0.7 Ma (JJJD_04; Fig. 4F) (Table 2.2). In addition, one sample obtained from an aplitic dike was dated at 105.0±3.0 Ma (JJJD_36; Fig. 4G), possibly representing a late magmatic event. The crystallization ages for five samples from the Sierra Atacama Diorite range between 114.8±0.5 and 111.6±0.6 Ma (Table 2.2). Finally, the Sierra Pajas Blancas Granodiorite is the youngest plutonic complex sampled in this study. The three granodiorites define a broad range of ca. 11 Ma, with ages between 110.4±2.8 and 99.2±0.7 Ma (Fig. 4H).

2.5.2. Whole-rock geochemistry

Samples were grouped in function of their zircon U-Pb weighted mean age and are identified in all figures according to the International Stratigraphic Chart color codes (Fig. 5; IUGS, 2013). Major and trace element concentrations are provided in Table 2.3. Additionally, compiled whole-rock analyses of intrusive rocks from the Coastal Cordillera of Chile are included in the figures and listed in the Table SM4.

The total alkali vs silica diagram (Fig. 5A) shows that the plutonic complexes in the study area range in composition from gabbro/diorite to granodiorite/monzogranite, consistent with previous studies performed in the Coastal Cordillera (Parada et al., 2007; Vivallo et al., 2008; Oliveros et al., 2020). This compositional range is also observed in the QAP plot (Fig. SM3.3). All samples plot in the sub-alkaline field with the exception of the alkali-rich Early to Middle Triassic Cerros del Vetado sample and the altered diorite from Sierra Áspera (125 Ma) (Fig. 5A). The intrusive rock samples have Low-K to high-K signatures in the SiO_2 vs K_2O diagram (Fig. 5B) and a magnesian affinity in the SiO_2 vs FeO*/(FeO*+MgO) diagram of Frost et al. (2001) (Fig. 5C). However, the Early to Middle Triassic syenogranite sample differs from the other by its shoshonitic composition. In the alumina saturation index diagram (Fig. 5D), samples have a metaluminous to slightly peraluminous composition and all the igneous rocks with a Triassic intrusion age are slightly peraluminous. Finally, in the discrimination diagrams of Pearce et al. (1984), all samples plot in the volcanic arc related granitoids (VAG) field, although the Early to Middle Triassic syenogranite plots in the within plate (Y+Nb vs Rb, Fig. SM3.4), syn-collisional orogenic (Yb+Ta vs Rb, Fig. SM3.5), and oceanic ridge (Yb vs Ta, Fig. SM3.6; Y vs Nb, Fig. SM3.7) granitic rocks fields.

Chondrite-normalized rare earth elements are displayed in Figure 6A-D. All plutonic complexes show higher enrichment in LREE than HREE (LaN/YbN = 1.93–9.06). Variable negative Eu-anomalies are present in most samples (EuN/Eu* = 0.25–1.05) (Table 2.3). However, the magnitude of this anomaly does not appear to be related to the degree of differentiation of the rocks, i.e., no correlation between Eu-anomalies and SiO_2, Zr or Hf contents is observed. Overall, the Early to Middle Triassic Cerros del Vetado sample exhibits the most enriched signature (LaN = 121 and YbN = 37), and the largest negative Eu-anomaly (EuN/Eu* = 0.25) (Table 2.3). In contrast, Late Triassic and Early Jurassic samples show moderate REE enrichment and slightly negative Eu-anomalies (Fig. 6A). The Late Jurassic Las Ánimas complex has higher REE enrichment, less pronounced slope in light to middle REE (LaN/DyN = 1.97), and a large negative Eu-anomaly compared to the Late Triassic and Early Jurassic rocks (Fig. 6B). Valanginian to Aptian (140-113 Ma) samples have variable degrees of REE enrichment and Eu-anomalies (Fig. 6B-C). In contrast, Albian-Cenomanian (~113-94 Ma) plutonic complexes show less enriched patterns and no anomalies.

Primitive mantle-normalized trace element patterns are also presented in Figure 6. All the studied samples present higher enrichment in LILE than in HSFE. Large ion lithophile elements show some variability, but a trend with Cs > Rb, Th, K > Ba > Sr can be recognized. In contrast, HFSE patterns are more consistent among samples. Nb-Ta, P and Ti negative anomalies are observed for most samples along with Pb positive anomalies. Rubidium show a positive correlation with KO2, and a similar but scattered relationship is observed for Zr and Hf (Fig. SM3.8). A well-defined negative trend from mafic to felsic compositions are found for Sr, P and Ti, and in compatible elements such as Sc and V. Chromium and Ni, which are generally more compatible, show a roughly defined negative correlation with silica (Fig. SM3.8). The syenogranite from the Early to Middle Triassic Cerros del Vetado complex is enriched in LILE, HFSE and REE compared to the Late Triassic and Early Jurassic samples, and presents similar but more pronounced Nb-Ta, P, Ti and Pb anomalies (Fig 6A). In contrast, the quartz diorite from the Early Jurassic Relincho intrusive shows no significant P and Ti negative anomalies. Samples from Valanginian-Hauterivian plutonic complexes (140 to 130 Ma; Fig. 6B) show similar patterns to the Late Jurassic diorite from Las Ánimas complex, but in the latter the Nb-Ta and P negative anomalies are more pronounced. On the other hand, Barremian to Cenomanian intrusive rocks (130 to 94 Ma) show higher variability but follow the same general trend (Fig. 6C,D).

2.5.3. Zircon geochemistry

A summary of the zircon minor and trace elements analyses, selected ratios and statistical descriptions are presented by age groups in Table 2.4. All results are reported in the Table SM2. The median is preferred as an indicator of the central tendency because of bias to lower values and the influence of outliers (Grimes et al., 2015). A total of 1064 measurements were made. Significant variations in some of elements were found, including (percentiles 5% to 95%): Hf (7060-18269 ppm), Y (277-5342 ppm), U (41-4906 ppm), Th (19-1321 ppm) and total REE (288-4291 ppm). Zircon grains have typically a moderate U content (median below 1000 ppm) and Th/U ratios above 0.4 and below 1.5, with the exception of the Early to Middle Triassic (~247 Ma) syenogranite that has a high U concentration and low Th content (median U = 1450 ppm, median Th/U = 0.24). Despite this difference, all zircon grains in the study appear to be magmatic in origin and do not show geochemical evidence of metamorphic, hydrothermal overprint, or radiation induced damage (Fig. 7A-C), which is consistent with the observed zoning in zircon crystals (Fig. 2).

Chondrite-normalized zircon trace elements patterns are shown in Fig. 8A-D. The studied samples display the typical trend for continental arc samples (Hoskin and Schaltegger, 2003), with extreme enrichment in HREE relative to LREE (YbN/SmN = 33–187; YbN/GdN = 11–39) and positive Ce and negative Eu anomalies (median CeN/CeN* = 6.98–99.6; EuN/EuN* = 0.02–0.53). The Early to Middle Triassic zircons have the broadest LREE contents (Fig. 8A), slightly positive Ce (CeN/CeN* = 1.66–17.2) and the largest negative Eu anomalies among all zircon (EuN/EuN* = 0.01–0.07). Late Triassic and Early Jurassic zircon grains display a similar behavior but a narrower concentration range, higher positive Ce (CeN/CeN* = 6.3–377.7) and less pronounced negative Eu anomaly (EuN/EuN* = 0.18–0.65). They show the most fractionated patterns among all samples with a median YbN/SmN = 178–187 (Fig. 8A). The Late Jurassic diorite from Las Ánimas complex shows a similar trend but zircon grains are considerably more enriched, with a median REE content of 2413 ppm, i.e., two to four times those of all other samples (593–1681 ppm; Table 2.4). Zircon grains from this sample also have the highest positive Ce anomalies among all samples (CeN/CeN* = 99.6) (Fig. 8B). Valanginian to Aptian (~140-113 Ma) zircon grains show HREE concentrations similar to those of Late

Triassic-Early Jurassic age but more enriched in LREE (Fig. 8B,C), resulting in considerably lower degree of fractionation between HREE and MREE (YbN/SmN = 21–25). Cerium and Eu anomalies are also present with moderate values (median CeN/CeN* = 60.2; median EuN/EuN* = 0.21). Albian (~113-105 Ma) zircon grains present strong positive Ce anomalies (median CeN/CeN* = 79.6), whereas Cenomanian (~99 Ma) samples display less pronounced negative Eu anomalies (EuN/EuN* = 0.53). Both Albian and Cenomanian (~113-99 Ma) samples are only slightly fractionated (YbN/SmN = 22-39; Fig. 8D).

Grimes et al. (2015) proposed several plots to trace the origin of zircon grains (Fig. 9), identifying four major settings: mid-ocean ridge (MOR-type; gray field), ocean island (OI-type; orange field), continental arc (Cont. Arc-type; green field), and post-collisional setting (yellow field). Most of the analyzed zircon grains plot in the "continental field" area defined in Grimes et al. (2007). In the Hf vs U/Yb diagram (Fig. 9A), in which the U/Yb ratio is used as a proxy for the degree of enrichment of the magmatic source and the Hf content as an indicator of melt fractionation, the Early to Middle Triassic zircon grains display higher U/Yb ratios than Late Triassic and Early Jurassic samples for similar fractionation degrees. On average, Jurassic samples have the most depleted source signature among all the studied plutonic complexes (U/Yb = 0.13–0.35 for Hf = 10940–17142 ppm), and plot close to the continental-oceanic boundary of Grimes et al. (2007) (dashed line in Fig. 9A-D). However, zircon grains from the Late Jurassic diorite show a more evolved signature, with higher Hf and Yb contents compared to Early Jurassic zircon grains (Fig. 9A,B). Early Cretaceous samples have a wide range of U/Yb values ranging from 0.13 to 1.60 (Fig. 9B-D); suggesting a more enriched source than Late Triassic and Jurassic samples. Similar results are obtained from the Nb/Yb vs U/Yb graph (Fig. 9E-H), in which the studied zircon grains plot in the lower end of the magmatic arc zircon array.

2.6. DISCUSSION

2.6.1. The pre-Andean magmatism and the onset of the Andean orogeny

The pre-Andean stage comprises the time span between the final assembly of Gondwana and the initiation of the Early Jurassic magmatism developed in the Coastal Cordillera (Charrier et al., 2007). The tectonic regime during this period is one of the most controversial subjects in the southwestern evolution of the Gondwana continent. Traditionally, the tectonic setting and its associated magmatism have been interpreted as a consequence of an orogenic collapse that occurred after the accretion of an exotic terrane, i.e., the "Equis terrane", during the middle Permian (Mpodozis and Ramos, 1990; Mpodozis and Kay, 1992). As a result, subduction ceased or was considerably reduced (Charrier et al., 2014), triggering rifting on the continental margin (Mpodozis and Kay, 1992; Hervé et al., 2014). Nevertheless, recent studies have proposed an extensional regime in a continuous subduction process since the latest Early Carboniferous (Vásquez et al., 2011; Del Rey et al., 2016; 2019; Coloma et al., 2017; Oliveros et al., 2020). Based on a compilation of zircon ages and isotopic analyses of rocks from the coastal and frontal ranges in north and central Chile, Del Rey et al. (2016) identified a continuous increase in εHf and decrease in $\delta^{18}O$ values between 330 and 210 Ma. Those authors suggested that a slab rollback and changes in the subduction angle were responsible for the location and type of magmatism during the pre-Andean stage (270 to 210 Ma). This interpretation was further supported by whole-rock chemical data reported by Coloma et al. (2017) and Del Rey et al. (2019), and where they concluded that Permian to Triassic igneous rocks from the Coastal and Frontal ranges (28 to 30°S) were the product of typical magmatism related to a convergent margin with only minor transitional A-type units. These transitional rocks were produced by

asthenospheric upwelling, decompression and melting of the lower continental crust just before or during foundering and rollback of the slab that led to the westward migration of the magmatic arc from the Frontal to the Coastal range during the Triassic.

In this study, we dated three Triassic intrusive complexes emplaced during the pre-Andean stage: the Early to Middle Triassic Cerros del Vetado complex (~247 Ma), and the Late Triassic Quebrada Quiscuda (~211 Ma) and Barquito (~203 Ma) plutons. The syenogranite sample from Cerros del Vetado plots in the alkali-calcic and shoshonitic fields in the MALI (Fig. SM3.9), and the SiO_2 vs K_2O (Fig. 5B) diagrams, respectively. This sample also shows a slightly peraluminous composition (Fig. 5D) and displays an enriched REE pattern and a much stronger negative Eu anomaly with a higher enrichment in LILE, Nb-Ta and strong Ba and Sr negative anomalies in comparison with other studied units (Fig. 6A,E). In addition, zircon grains from this syenogranite sample are enriched in REE, more fractionated and have the weakest positive Ce and the strongest negative Eu anomalies of all the samples analyzed in this study (Fig. 8A and Table 2.4). Moreover, four older concordant zircon ages are interpreted as an inherited component and are further evidence for crustal assimilation. In terms of the tectonic setting, the results are not conclusive. The geochemical features of this pluton, i.e. shoshonitic, weakly peraluminous, relatively flat REE chondrite-normalized patterns and strong negative Eu anomaly, resembles those of El León, El Colorado and Chollay intrusive units (28°10'S 69°30'W; Table SM5), which have similar ages (260-242 Ma) but are located in the Frontal Andes near the Chilean-Argentinean border; the latter are high-K calc-alkaline instead of shoshonitic, but share all other characteristics. These units were studied by Mpodozis and Kay (1992), Coloma et al. (2017) and Del Rey et al. (2019), who classified them as highly fractionated I- and S-type granitoids or transitional A-type granitoids formed by crustal anatexis during rollback and steepening of the slab (Fig. 8 in Coloma et al., 2017; Fig. 7 in Del Rey et al., 2019).

Figure 10 shows several classification diagrams that compare samples from those units (i.e., El León, El Colorado and Chollay plutons) with the syenogranite from Cerros del Vetado. These diagrams show that most samples, including Cerros del Vetado, present a relatively flat REE pattern with a marked negative Eu anomaly (Fig. 10A), an enrichment in LILE over HFSE, and positive K and Pb, and negative Ba, Nb-Ta, Sr and Ti anomalies (Fig. 10B). These samples plot either in the upper part of the fields of I- and S-type granites or the A-type granite field in the classification diagrams of Whalen et al. (1987) (Fig. 10C,D; Fig. SM3.10). In the diagrams of Eby (1992), the Frontal Andes samples are classified as A2-type granites but the Early to Middle Triassic syenogranite from this study plots at the limit or outside the defined fields due to its high Y/Nb ratio (Fig. 10D,E; Fig. SM3.11). Finally, in the recently proposed Nb/Ta discrimination plots of Ballouard et al. (2020) (Fig. 10F; Fig. SM3.12), the syenogranite from Cerros del Vetado plots at the limit between the fields of muscovite-bearing peraluminous granites and A2-type granites. Overall, the data show that the syenogranite from Cerros del Vetado pluton shares some geochemical characteristics with upper Permian-lower Triassic Frontal Cordillera units showing a geochemical signature transitional between that of A-type and evolved I-type granitoids (Table SM5). Further work is required to precisely determine if these geochemical signatures represent an anorogenic magmatic event or a high degree fractionation process. Nevertheless, in the conceptual model of Coloma et al. (2017) and Del Rey et al. (2019) the Cerros del Vetado pluton, and any other intrusive unit in the Coastal Cordillera domain, should have: i) typical I-type, subduction related characteristics due to its location to the west of the primary axis of the Permian-Late Triassic magmatic arc positioned in the Frontal Cordillera; and ii) an emplacement age younger than those of the igneous units in the Frontal Cordillera; which is not the case. In

addition, if subduction was uninterrupted from the Permian to Late Triassic, igneous units with similar characteristics and ages to Cerros del Vetado should be present north and south of this pluton but so far these have not been recognized in the area. Therefore, the preferred explanation for the age, location and whole-rock geochemistry of Cerros del Vetado pluton is that it was generated by a transitional anorogenic magmatic event.

Conversely, the whole-rock chemistry of the Late Triassic Quebrada Quiscuda and Barquito complexes are consistent with an origin in a continental magmatic arc. They are calc-alkaline, magnesian and metaluminous to slightly peraluminous (Fig. 5A-D); and present high LILE relative to HFSE contents, Nb-Ta throughs and Ti anomalies, and REE fractionation, suggesting that they were formed by subduction related magmatism (Fig. 6A,E). In addition, their zircon REE patterns are similar to those of the Early Jurassic intrusive rocks of the Coastal Cordillera (Fig. 8A) and plot in the continental arc field in tectonic discrimination diagrams (Fig. 9A,B). Consequently, these results support recent studies that propose the onset of Andean magmatism in the Late Triassic (Vásquez et al., 2011; Rodríguez et al., 2019), before previously estimations (~200-190 Ma; Charrier et al., 2007).

Zircon bivariate diagrams were constructed in order to identify geochemical signals that could be used to discriminate between pre-Andean and Andean magmatic events (Fig. 11). A continuous subduction model from the Permian to Late Triassic as proposed by Del Rey et al. (2016), should be reflected not only in their zircon isotopic signatures but in the zircon trace element data presented in this study. Zircon grains from the Late Triassic (~210 Ma) to lower Early Cretaceous (~130 Ma; Hauterivian) have low U/Yb ratios, spanning between 0.1 to 0.5 (Fig. 11A), suggesting that their source was slightly enriched compared to a N-MORB magma (Grimes et al., 2007; 2015; Fig. 9A). However, during that time span their negative Eu anomaly decreased from 0.6 to 0.1. In contrast, Early to Middle Triassic zircon grains exhibit a more enriched source (U/Yb = 0.5–1.1) and are characterized by weak positive Ce and strong negative Eu anomalies (Ce/Ce* < 25; Eu/Eu* < 0.06) (Fig. 11B).

Additionally, in the Th/U vs Eu/Eu* plot (Fig. 11C), zircon grains from the Cerros del Vetado syenogranite display low Th/U values that differ significantly from Late Triassic to Early Cretaceous samples. Overall, based on whole-rock and zircon geochemical analyses, most studied plutonic units appear to have been formed under a subduction tectonic regime and hence, are representative of the Andean orogeny. The only exception is the Early to Middle Triassic Cerros del Vetado syenogranite, which has a different, unique chemistry in comparison with all other samples studied here and is interpreted as a pre-Andean magmatic event not related to a subduction regime.

2.6.2. Geochronology and petrogenesis of the Andean intrusive rocks in the Coastal Cordillera of northern Chile

This is the first systematic study based on zircon U-Pb geochronology from plutonic complex of the Coastal Cordillera that covers the entire time span of the early stage of the Andean orogeny (210 to 95 Ma). Our results provide further evidence for: i) the episodic nature of intrusion events in arc cordilleras (DeCelles et al., 2009); and ii) the eastward migration of the Jurassic to Early Cretaceous magmatic arc of the Andes (Mpodozis and Ramos, 1990; Grocott and Taylor, 2002; Ramos, 2010), which was previously determined based mostly on imprecise K-Ar and limited $^{40}Ar/^{39}Ar$ thermochronology (Fig. 1 and 12A,B; Fig. SM3.13). In general, $^{40}Ar/^{39}Ar$ ages are consistent with our new precise zircon U-Pb geochronology results and

suggest rapid cooling from ~800 to ~500°C, based on closure temperatures of the U-Pb in zircon and $^{40}Ar/^{39}Ar$ system in biotite and amphibole. Further, the good agreement between U-Pb and $^{40}Ar/^{39}Ar$ dates indicates that intrusive complexes were mostly unaffected by superimposed thermal (magmatic) events.

In the Coastal Cordillera of northern Chile three main plutonic episodes, probably related to high magmatic flux rates, were previously documented at 200-190 Ma, 160-150 Ma, and 130-120 Ma (Berg and Baumann, 1985). Dallmeyer et al. (1996) further constrained these episodes at 202-188 Ma (Late Triassic-Early Jurassic), 160-153 Ma (Late Jurassic) and 130-127 Ma (Hauterivian-Barremian); and defined two additional episodes at 142-138 Ma (Berriasian) and 106-103 Ma (Albian). In this study four of these five episodes were recognized (Fig. 12C). The Late Triassic to Early Jurassic pulse is represented by the Barquito (203-190 Ma), Flamenco (~194 Ma) and Relincho (~192 Ma) plutons, whereas the Quebrada Quiscuda stock (~211 Ma) could be related to this event or correspond to an earlier distinctive episode. The Las Ánimas Late Jurassic (~150 Ma) complex is associated with the second period described in Berg and Baumann (1985) and Dallmeyer et al. (1996). The third pulse identified in Dallmeyer et al. (1996) was determined by dating the Monardes-Moradito complex (27°10'S, 70°35'W), which was not sampled in this study. The middle and late Early Cretaceous episodes, i.e., 142-138 Ma, 130-127 Ma and 106-103 Ma, were documented here but their time spans are slightly longer than those defined by Dallmeyer et al. (1996). Hence, based on our data we propose a mid-Valanginian to early Aptian (135-123 Ma) and a late Aptian to early Cenomanian (117-99 Ma) episode. Our results support the notion that magmatic activity was almost uninterrupted between the Valanginian to Cenomanian with only a short lull in the middle Aptian (~120 Ma) consistent with observations reported by Grocott and Taylor (2002). In addition, we noted that some plutonic complexes, such as the La Borracha plutonic complex and Sierra Pajas Blancas Granodiorite, were formed over periods exceeding 10 Ma.

Whole-rock geochemistry data provide some insights on the source and evolution of the plutonic rocks of the early Andean stage (Fig. 6). These rocks are characterized by: i) an enrichment in LILE over HFSE; ii) fractionation of REE; iii) the presence of a Nb-Ta trough; iv) a Pb positive and variable P and Ti negative anomalies; and v) predominantly metaluminous to slightly peraluminous, calc-alkaline affinities with minor low- or high-K characteristics (Fig. 5A-D). These features have also been recognized in other igneous units from the Coastal Cordillera (Marschik et al., 2003; Kramer et al., 2005; Oliveros et al., 2007; 2020; Vásquez et al., 2011), and are interpreted as representative of magmas related to a subduction regime (Pearce, 1982). This conclusion is also supported by the tectonic discrimination diagrams presented here (Fig. SM3.4-7), and zircon trace element data that show high zircon HREE over LREE chondritic normalized contents and distinct positive Ce and negative Eu anomalies, which are characteristic of continental arcs rocks (Fig. 9). Regarding the source of magmatism in the Coastal Cordillera, some researchers have suggested a juvenile, depleted mantle source for the Jurassic magmas based on Sr, Pb and Nd isotopic signatures, with minor contributions from slab sediments or crustal assimilation during arc evolution (e.g., Lucassen and Thirlwall, 1998; Kramer et al., 2005; Lucassen et al., 2006; Oliveros et al., 2007; 2020). In this study our new data using zircon geochronology and trace element geochemistry is used to better constrain the Late Triassic to Early Cretaceous magmatic evolution and although the dataset is relatively small, some general trends can be described.

The Andean orogeny started during the Late Triassic with magmatism generated by subduction in a rather attenuated crust (Scheuber et al., 1994; Charrier et al., 2007). The crustal

thickness for this period was estimated by using whole-rock Sr/Y (~18) and LaN/YbN (~7.7) ratios of Late Triassic samples, yielding an estimated Moho depth between ~30 and ~45 km (Fig. 13A). On the other hand, Oliveros et al. (2020) recently reported crustal thickness of ~10 and 40 km, based on those same ratios. Our results are not comparable with the latter because more precise determination of the crustal thickness requires a larger dataset and is based on the elemental composition of volcanic rocks (Profeta et al., 2015). Nevertheless, it provides a preliminary approximation to understand the conditions under which the early stage Andean magmatism developed. After the onset of Andean tectonic cycle, the thickness of the continental crust was reduced due to extensional to transtensional conditions during this period (Mpodozis and Ramos, 1990; Scheuber and González, 1999; Seymour et al., 2020). As a result, intrusive rocks of the Coastal Cordillera have less differentiated compositions than their Cenozoic counterparts (Parada et al., 2007; Rossel et al., 2020), and show a progressive depletion of the magmatic source with scarce crustal contamination and/or fluids contributions from the slab (Kramer et al., 2005; Lucassen et al., 2006). Consequently, the Jurassic quartz diorite from Relincho pluton display lower whole-rock Th/Yb (~2.1) and Ba/La (~11) ratios than Late Triassic rocks, i.e., ~3.9 and ~18, respectively (Fig. 13B-D). This depleting trend appears to continue at least until the Late Jurassic, as recorded by a less enriched sample from Las Ánimas plutonic complex (Th/Yb = 0.99; Ba/La = 13; Fig. 13B,C), and is consistent with the strong arc normal extensional setting characteristic of this period (Scheuber and González, 1999; Grocott and Taylor, 2002) resulting in a crustal thickness of about 20 km (Sr/Y ~13; LaN/YbN ~2.7). These results are further supported by compositional trends in other whole-rock ratios (Fig. SM3.14).

In addition, a similar trend could be interpreted from the zircon trace element dataset. A decrease in the zircon U/Yb ratio from the Late Triassic (0.26) to Jurassic (0.21-0.24; Fig. 9A,B and 11A) reflects the depletion experienced by the mantle source of the magmatic arc (Grimes et al., 2007; 2015). Furthermore, the strong increase in negative zircon Eu-anomalies, from 0.46 to 0.18, during the same period suggest that fluid and sediment contributions from subduction diminished, forming possibly less oxidized magmas (Trail et al., 2012). This result is also consistent with an increase in crystallization temperatures recorded by the zircon Ti contents (Table 2.4), which almost double from 6.5 ppm in the Late Triassic rocks to over 12 ppm in the diorite sample from Las Ánimas pluton.

The previously described scenario appears to change in the Early Cretaceous, when more variable and enriched signatures are observable in the studied samples (Fig. 11 and 13). Even though the dispersion of whole-rock and zircon values could be related to the differentiation degree of the sampled rocks, an average increase in whole-rock Ba/La and Th/Yb and zircon U/Yb ratios point out to a greater contribution of fluids and sediments to the magmatic source. On average, Jurassic samples from Relincho and Las Ánimas plutons have a Ba/La ratio of ~12, considerably lower than those obtained for Early Cretaceous rocks (Ba/La~20, excluding monzonites and the Sierra Áspera altered sample).

Regarding the Th/Yb ratio, it is highly dependent on the differentiation degree of the samples. Jurassic samples have Th/Yb ratios of ~1.6, similar to low silica (SiO_2 < 65%) Early Cretaceous samples (~1.4). However, the average Th/Yb ratio for the more differentiated rocks (SiO_2 ≥ 65%) is three times higher (~4.4) for Early Cretaceous samples. A similar trend is observed in the zircon U/Yb ratios, where the Late Jurassic Las Ánimas sample shows a median zircon U/Yb ratio of 0.24, about half the value determined for Early Cretaceous rocks (~0.52).

These observations could be explained by a change from strong arc normal extensional to oblique transtensional tectonic setting. Based on structural studies on the Atacama Fault system, several authors have suggested that this change would have occurred between 150 and 125 Ma (Dallmeyer et al., 1996; Scheuber and González, 1999; Grocott and Taylor, 2002; Seymour et al., 2020), coincident with the timing after which the studied rocks present more disperse and enriched signatures.

2.7. CONCLUSIONS

We performed the first regional, geochemical study using coupled U-Pb dating and minor/trace elements analysis in zircon grains from Mesozoic intrusive rocks in the Coastal Cordillera of northern Chile. The new data contributes to our understanding of the evolution of the southwestern margin of Gondwana during the Mesozoic and the onset of the Andean tectonic cycle. Based on our geochemical data, the following conclusions can be presented:

i. A transitional A-type, rift related magmatism appears to be the most plausible explanation for the location, age and geochemical characteristics of the Early to Middle Triassic Cerros del Vetado syenograinte. However, the recently proposed hypothesis of a continuous subduction regime from the latest Early Carboniferous cannot be completely ruled out with the current evidence. Thus, further studies regarding the petrogenesis of Early to Middle Triassic plutons along the Coastal Cordillera are needed.

ii. The Quebrada Quiscuda stock (211.3±1.2 Ma) has characteristics typical of an Andean -related magmatism, and its zircon geochemical composition is similar to those from Jurassic to latest Early Cretaceous intrusive units analyzed here. Therefore, the initiation of the Andean orogeny, in this part of the Coastal Cordillera, could be traced at least to ca. 210 Ma, about 10 Ma before previous estimates.

iii. The reported episodic magmatism of Late Triassic to latest Early Cretaceous age in the Coastal Cordillera is further supported by new precise geochronological data presented in this study. These results also corroborate the progressive eastward migration of the magmatic arc during the early stage of the Andean orogeny in northern Chile.

iv. The studied plutonic units appear to have been sourced from a rather depleted mantle source in an extensional to transtensional subduction regime. As a result, most of them have typical calc-alkaline, metaluminous to slightly peraluminous affinities of I-type granitoids. As the arc evolved and migrated to the east, variable slab-derived fluids and sediment-melt contributions were recorded in the whole-rock and zircon geochemistry. Less enriched signatures were identified in rocks from the latest Jurassic and the earliest Cretaceous, probably reflecting the transition from an extensional to transtensional setting. After this period, the geochemical signature of the magmas indicates contributions from slab-derived fluids and/or the crustal contamination perhaps related to this tectonic setting change.

Finally, this study illustrates the potential use of zircon U-Pb dating coupled to minor/trace element analysis in assessing the evolution of magmatic arcs.

2.8. BIBLIOGRAPHY

Aguirre, L., Féraud, G., Morata, D., Vergara, M., Robinson, D., 1999. Time Interval between volcanism and burial metamorphism and rate of basin subsidence in a Cretaceous Andean extensional setting. Tectonophysics 313, 433-447.

Arévalo, C., 2005a. Carta Copiapó, Región de Atacama. Servicio Nacional de Geología y Minería: Santiago.

Arévalo, C., 2005b. Carta Los Loros, Región de Atacama. Servicio Nacional de Geología y Minería: Santiago.

Ballouard, C., Massuyeau, M., Elburg, M.A., Tappe, S., Viljoen, F., Brandenburg, J.T., 2020. The magmatic and magmatic-hydrothermal evolution of felsic igneous rocks as seen through Nb-Ta geochemical fractionation, with implications for the origins of rare-metal mineralizations. Earth-Science Reviews 203, 103115.

Belousova, E.A., Griffin, W.L., O'Reilly, S.Y., Fisher, N.J., 2002. Igneous zircon: trace element composition as an indicator of source rock type. Contribution in Mineralogy and Petrology 143, 602-622.

Berg, K., Baumann, A., 1985. Plutonic and metasedimentary rocks from the Coastal Range of northern Chile: Rb-Sr and U-Pb systematic. Earth and Planetary Science Letters 75, 101-115.

Blanco, N., Godoy, E., Marquard, C., 2003. Cartas Castilla y Totoral Bajo, Región de Atacama. Servicio Nacional de Geología y Minería: Santiago.

Blundell, D.J., 2002. The timing and location of major ore deposits in an evolving orogen: the geodynamic context. In Blundell, D.J., Neubauer, F. and von Quadt, A., eds., The timing and location of major ore deposits in an evolving orogen: London, The Geological Society, p. 1-12.

Brown, M., Díaz, F., Grocott, J., 1993. Displacement history of the Atacama fault system 25°00'-27°00'S, northern Chile. Geological Society of America Bulletin 105, 1165-1174.

Carley T.L., Miller C.F., Wooden J.L., Padilla A.J., Schmitt A.K., Economos R.C., Bindeman I.N., Jordan B.T., 2014. Iceland is not a magmatic analog for the Hadean: evidence from the zircon record. Earth Planetary Science Letters, 405, 85-97.

Chapman, J.B., Ducea, M.N., 2019. The role of arc migration in Cordilleran orogenic cyclicity. Geology 47 (7), 627-631.

Charrier, R., Pinto, L., and Rodríguez, M. P., 2007, Tectonostratigraphic evolution of the Andean Orogen in Chile. In Moreno, T., and Gibbons, W., eds., The geology of Chile: London, The Geological Society, p. 21-114.

Charrier, R., Ramos, V.A., Tapia, F., Sagripanti, L., 2014. Tectono-stratigraphic evolution of the Andean Orogen between 31° and 37° S (Chile and Western Argentina). Geological Society of London, Special Publication 399, 13–61.

Coira, B., Davidson, J., Mpodozis, C., Ramos, V., 1982. Tectonic and magmatic evolution of the Andes of northern Argentina and Chile. Earth Science Reviews 18, 303-332.

Coloma, F., Valin, X., Oliveros, V., Vásquez, P., Creixell, C., Salazar, E., Ducea, M.N., 2017. Geochemistry of permian to triassic igneous rocks from northern Chile (28°-30°15'S): Implications on the dynamics of the proto-Andeanmargin. Andean Geology 44, 147–148.

Coney, P. J., and Evenchick, C. A., 1994, Consolidation of the American Cordilleras: Journal of South American Earth Sciences, v. 7, p. 241-262.

Corfu, F., Hanchar, J.M., Hoskin, P.O.W., Kinny, P., 2003. Atlas of zircon textures. Reviews in Mineralogy and Geochemistry 53 (1), 469-500.

Dallmeyer, R.D., Brown, M., Grocott, J., Taylor, G., Treloar, P., 1996. Mesozoic magmatic and tectonic events within the Andean plate boundary zone, north Chile: constraints from 40Ar/39Ar minerals ages. Journal of Geology 104, 19-40.

DeCelles, P. G., Ducea, M.N., Kapp, K., and Zandt, G., 2009, Cyclicity in Cordilleran orogenic systems: Nature Geoscience, v. 2, p. 251-257.

Del Rey, A., Arriagada, C., Dekart, K., Martínez, F., 2016. Resolving the paradigm of the late Paleozoic-Triassic Chilean magmatism: Isotopic approach. Gondwana Research 37, 172-181.

Del Rey, Dekart, K., Planavsky, N., A., Arriagada, C., Martínez, F., 2019. Tectonic evolution of the southwestern margin of Pangea and its global implications: Evidence from the mid Permian–Triassic magmatism along the Chilean-Argentine border. Gondwana Research 76, 303-321.

Eby, G.N., 1992. Chemical subdivision of the A-type granitoids: petrogenetic and tectonic implications. Geology 20, 641-644.

Elger, K., Oncken, O., and Glodny, J., 2005, Plateau-style accumulation of deformation: Southern Altiplano: Tectonics, v. 24, no. 4, p. TC4020.

Espinoza, M., Montecino, D., Oliveros, V., Astudillo, N., Vásquez, P., Reyes, R., Celis, C., González, R., Contreras, J., Creixell, C., Martínez, A. 2019. The synrift phase of the early Domeyko Basin (Triassic, northern Chile): Sedimentary, volcanic and tectonic interplay in the evolution of an ancient subduction -related rift basin. Basin Research, 31, 4-32.

Finch, R.J., Hanchar, J.M., 2003. Structure and chemistry of zircon and zircon group minerals. Reviews in Mineralogy and Geochemistry 53 (1), 1-25.

Gao, P., Zheng, Y.-F., Zhao, Z.-F., 2016. Distinction between S-type and peraluminous I-type granites: Zircon versus whole-rock geochemistry. Lithos, 258-259, 77-91.

Garzione, C. N., Hoke, G. D., Libarkin, J. C., Withers, S., MacFaddon, B., Eiler, J., Ghosh, P., and Mulch, A., 2008, Rise of the Andes: Science, v. 320, p. 1304-1307.

Gehrels, G.E., Valencia, V., and Ruiz, J., 2008, Enhanced precision, accuracy, efficiency, and spatial resolution of U-Pb ages by laser ablation-multicollector-inductively coupled plasma-mass spectrometry: Geochemistry Geophysics Geosystems 9, Q03017.

Godoy, E., Lara, L., 1998. Hojas Chañaral y Diego de Almagro, Región de Atacama. Servicio Nacional de Geología y Minería: Santiago.

Godoy, E., Lara, L., 1999. Hoja Puerto Flamenco, Región de Atacama. Servicio Nacional de Geología y Minería: Santiago.

Gordon, S.M., Whitney, D.L., Teyssier, C., Fossen, H., 2013. U–Pb dates and trace-element geochemistry of zircon from migmatite, Western Gneiss Region, Norway: Significance for history of partial melting in continental subduction. Lithos 170-171, 35-53.

Grimes, C.B., John, B.E., Kelemen, P.B., Mazdab, F., Wooden, J.L., Cheadle, M.J., Hanghøj, K., Schwartz, J.J., 2007. The trace element chemistry of zircons from oceanic crust: a method for distinguishing detrital zircon provenance. Geology 35, 643-646.

Grimes, C.B., Wooden, J.L., Cheadle, M.J., John, B.E., 2015. “Fingerprinting” tectono-magmatic provenance using trace elements in igneous zircon. Contributions in Mineralogy and Petrology 170 (46), 1-26.

Grocott, J., Brown, M., Dallmeyer, R., Taylor, G., Treloar, P., 1994. Mechanisms of continental growth in extensional arcs: an example from the Andean plate boundary zone. Geology 22, 391-394.

Grocott, J., Taylor, G.K., 2002. Magmatic arc fault systems, deformation partitioning and emplacement of granitic complexes in the Coastal Cordillera, northern Chilean Andes (25°30'S to 27°00'S). Journal of the Geological Society of London 159, 425-442.

Gromet, L. P., and Silver, L. T., 1987, REE variations across the Peninsular Ranges Batholith; implications for batholithic petrogenesis and crustal growth in magmatic arcs: Journal of Petrology, v. 28, no. 1, p. 75-125.

Haschke, M., Siebel, W., Guenther, A., and Scheuber, E., 2002, Repeated crustal thickening and recycling during the Andean Orogeny in North Chile (21°-26°S): Journal of Geophysical Research, v. 107, no. B1, p. doi: 10.1029/2001JB000328.

Hawkesworth, C.J., Kemp, A.I.S., 2006. Using hafnium and oxygen isotopes in zircons to unravel the record of crustal evolution. Chemical Geology 226, 144-162.

Hedenquist, J.W., Lowenstern, J.B., 1994. The Role of Magmas in the Formation of Hydrothermal Ore Deposits. Nature, v. 370, 519-527.

Hervé, F., Faúndez, V., Calderón, M., Massone, H., Willner, A., 2007. Metamorphic and plutonic basement complexes. In The Geology of Chile (Gibbons, W., Moreno, T., editors). The Geological Society, Special Publication, 5-19. London.

Hervé, F., Fanning, C.M., Calderón, M., Mpodozis, C., 2014. Early Permian to Late Triassic batholiths of the Chilean Frontal Cordillera (28°–31°S): SHRIMP U–Pb zircon ages and Lu–Hf and O isotope systematics. Lithos 184-187, 436-446.

Hoskin, P.W.O., 2005. Trace-element composition of hydrothermal zircon and the alteration of Hadean zircon from the Jack Hills, Australia. Geochimica et Cosmochimica Acta 69, 637-648.

Hoskin, P.W.O., Schaltegger, U., 2003. The composition of zircon and igneous and metamorphic petrogenesis. Reviews in Mineralogy and Geochemistry 53 (1), 27-62.

Irvine, T.N., Baragar, W.R.A., 1971. A guide to the chemical classification of the common volcanic rocks. Canadian Journal of Earth Science 8, 523-548.

IUGS (International Union of Geological Sciences), 2013. International Chronostratigraphic Chart, v 2013/01.

Jackson, S.E., Pearson, N.J., Griffin, W.L., Belousova, E.A., 2004. The application of laser ablation inductively coupled plasma-mass spectrometry to in situ U-Pb zircon geochronology. Chemical Geology 211 (1-2), 47-69.

Knipping, J.L., Bilenker, L.D., Simon, A.C., Reich, M., Barra, F., Deditius, A.P., Lundstrom, C., Bindeman, I., Munizaga, R., 2015. Giant Kiruna-type deposits form by efficient flotation of magmatic magnetite suspensions. Geology 43, 591-594.

Kojima, S., Trista-Aguilera D., Hayashi, K., 2009. Genetic aspects of the manto-type copper deposits based on geochemical studies of north Chilean deposits. Resource Geology, 87-98.

Kramer, W., Siebel, W., Romer, R. L., Haase, G., Zimmer, M., Ehrlichmann, R., 2005. Geochemical and isotopic characteristics and evolution of the Jurassic volcanic arc between Arica (18°30'S) and Tocopilla (22°S), North Chilean Coastal Cordillera. Chemie der Erde - Geochemistry, 65 (1), 47-78.

Leisen, M., Romero, R., Barra, F., Morata, D., 2018. Geocronología U-Pb de circones mediante ablación láser acoplado a un ICP-MS multicolector o a un cuádrupolo: Comparaciones y limitaciones. In XV Congreso Geológico Chileno, Concepción, Chile.

Levi, B., Aguirre, L., Nyström, J., Padilla, H., Vergara, M., 1989. Low grade regional metamorphism in the Mesozoic–Cenozoic volcanic sequences of the Central Andes. Journal of Metamorphic Petrology 7, 487-495.

Liu, Y., Hu, Z., Zong, K., Gao, C., Gao, S., Xu, J., Chen, H., 2010. Reappraisement and refinement of zircon U-Pb isotope and trace element analyses by LA-ICP-MS. Chinese Science Bulletin 55 (15), 1535-1546.

Lucassen, F., Thirlwall, M.F., 1998. Sm-Nd formation ages and mineral ages in metabasites from the Coastal Cordillera, northern Chile. Geol Rundsch 86, 767-774.

Lucassen, F., Kramer, W., Bartsch, V., Wilke, H.G., Franz, G., Romer, R.L., Dulski, P., 2006. Nd, Pb and Sr isotope composition of juvenile magmatism in the Mesozoic large magmatic province of northern Chile (18°-27°S): indications for a uniform subarc mantle. Contributions to Mineralogy and Petrology 152: 571-589.

Ludwig, K., 2010. Isoplot/Ex version 4.1, a geochronological toolkit for Microsoft Excel. Berkeley Geochronology Center, Special Publication 4.

Maksaev, V., Townley, B., Palacios, C., Camus, F. 2007. Metallic ore deposits. In Moreno, T., Gibbons, W. (Eds) The Geology of Chile. The Geological Society, London: 179-199. London.

Maksaev, V., Munizaga, F., Tassinari, C., 2014. Timing of the magmatism of the paleo-Pacific border of Gondwana: U-Pb geochronology of Late Paleozoic to Early Mesozoic igneous rocks of the north Chilean Andes between 20° and 31°S. Andean Geology 41 (3), 447-506.

Marschik, R., Fontboté, L. 2001. The Punta del Cobre Formation, Punta del Cobre–Candelaria area, northern Chile. Journal of South American Earth Sciences, 14(4), 401–433.

Marschik, R., Fontignie, D., Chiaradia, M., Voldet, P., 2003. Geochemical and Sr–Nd–Pb–O isotope composition of granitoids of the Early Cretaceous Copiapó plutonic complex (27°30'S), Chile. Journal of South American Earth Science, 16, 381-398.

Martínez, F., Arriagada, C., Peña, M., Del Real, I., Deckart. K., 2013. The structure of the Chañarcillo Basin: An example of tectonic inversion in the Atacama region, northern Chile. Journal of South American Earth Sciences 42, 1-16.

McKay, M. P., Jackson, W.T., Jr., Hessler, A., 2018. Tectonic stress regime recorded by zircon Th/U. Gondwana Research 57, 1-9.

Middlemost, E.A.K., 1994. Naming materials in the magma/igneous rock system. Earth-Science Reviews 37, 215-244.

Mpodozis, C., Allmendinger, R.W., 1993. Extensional tectonics, Cretaceous Andes, northern Chile (27°S). Geological Society of America Bulletin 105, 1462-1477.

Mpodozis, C., Kay, S.M., 1992. Late Paleozoic to Triassic evolution of the Gondwana margin, evidence from Chilean Frontal Cordillera batholiths (28°S to 31°S). The Geological Society of America, Bulletin 104 (8), 999-1014.

Mpodozis, C., Kay, S.M., Cornejo, P., 2018. Major Late Paleozoic to early Jurassic Magmatic Events and Tectonic Shifts along the Pangean Margin of Northern Chile. In XV Congreso Geológico Chileno, Concepción, Chile.

Mpodozis C, Ramos VA., 1990. The Andes of Chile and Argentina. In Geology of the Andes and its Relation to Hydrocarbon and Mineral Resources, Ericksen, G.E., Cañas-Pinochet, M.T., Reinemud, J.A. (eds). Circumpacific Council for Energy and Mineral Resources. Earth Sciences Series 11, 59–90. Houston, Texas.

Nardi, L.V.S., Formoso, M.L.L., Müller, I.F., Fontana, E., Jarvis, K., Lamarão, C., 2013. Zircon/rock partition coefficients of REEs, Y, Th, U, Nb, and Ta in granitic rocks: uses for provenance and mineral exploration purposes. Chemical Geology 335, 1-7.

Oliveros, V., Féraud, G., Aguirre, L., Fornari, M., Morata, D., 2006. The Early Andean Magmatic Province (EAMP): 40Ar/39Ar dating on Mesozoic volcanic and plutonic rocks from the Coastal Cordillera, northern Chile. Journal of Volcanology and Geothermal Research 157, 311-330.

Oliveros, V., Morata, D., Aguirre, L., Féraud, G., Fornari, M. 2007. Jurassic to Early Cretaceous subduction-related magmatism in the Coastal Cordillera of northern Chile (18°30'-24°S): geochemistry and petrogenesis. Revista Geológica de Chile 34, 209-232.

Oliveros, V., González, J., Espinoza, M., Vásquez, P., Rossel, P., Creixell, C., Sepúlveda, F., Bastías, F., 2017. The early stages of the volcanic arc in the Southern Central Andes, in: Folguera, A., Contreras -Reyes, E., Heredia, N., Encinas, A., Iannelli, S., Oliveros, V., Dávila, F.M., Collo, G., Giambiagi, L.B., Maksymowicz, A., Iglesia Llanos, M.P., Turienzo, M.M., Naipauer, M., Orts, D., Litvak, V.D., Alvarez, O., Arriagada, C. (Eds.), The Evolution of the Chilean -Argentinean Andes. Springer International Publishing, Berlin Heidelberg, pp. 185 –212.

Oliveros, V., Vásquez, P., Creixell, C., Lucassen, F., Ducea, M.N., Ciocca, I., González, J., Espinoza, M., Salazar, E., Coloma, F., Kasemann, S.A., 2020. Lithospheric evolution of the Pre- and Early Andean convergent margin, Chile. Gondwana Research 80, 202-227.

Padilla, A.J., Miller, C.F., Carley, T.L., Economos, R.C., Schmitt, A.K., Coble, M.A., Wooden, J.L., Fisher, C.M., Vervoort, J.D., Hanchar, J.M., 2016. Elucidating the magmatic history of the Austurhorn silicic intrusive complex (southeast Iceland) using zircon elemental and isotopic geochemistry and geochronology. Contributions to Mineralogy and Petrology 171 (69), 1-21. DOI 10.1007/s00410-016-1279-z

Parada, M. A., López-Escobar, L., Oliveros, V., Fuentes, F., Morata, D., Calderon, M., Aguirre, L., Féraud, G., Espinoza, F., Moreno, H., Figueroa, O., Muñoz-Bravo, J., Troncosco-Vásquez, R., and Stern, C. R., 2007, Andean magmatism, in Moreno, T., and Gibbons, W., eds., The geology of Chile: London, The Geological Society, p. 115-146.

Paton, C., Hellstrom, J., Paul, B., Woodhead, J., Hergt, J., 2011. Iolite: Freeware for the visualization and processing of mass spectrometric data. Journal of Analytical Atomic Spectrometry 26, 2508-2518.

Pearce, J.A. 1982. Trace elements characteristics of lavas from destructive plate boundaries. In Thorpe, R.S., ed., Andesites. Orogenic andesites and related rocks. John Willey and Sons: 525-548.

Pearce, J.A., Harris, N.B.W., Tindle, A.G., 1984. Trace element discrimination diagrams for the tectonic interpretation of granitic rocks. Journal of Petrology 25, 956-983.

Peccerillo, R., Taylor, S. R., 1976. Geochemistry of Eocene calc-alkaline volcanic rocks from the Kastamonu area, northern Turkey. Contributions to Mineralogy and Petrology 58, 63-81.

Ramos, V.A., 2010. The tectonic regime along the Andes: present-day and Mesozoic regimes. Geological Journal 45, 2-25.

Reymer, A., and Schubert, G., 1984, Phanerozoic addition rates to the continental crust and crustal growth: Tectonics, v. 3, no. 1, p. 63-77.

Richards, J.P., López, G.P., Zhu, J.J., Creaser, R.A., Locock, A.J., Mumin A.H., 2017. Contrasting tectonic settings and sulfur contents of magmas associated with cretaceous porphyry Cu±Mo±Au and intrusion-related iron oxide Cu-Au deposits in Northern Chile. Economic Geology 102 (2), 295-318.

Rodríguez, N., Díaz-Alvarado, J., Fernández, C., Fuentes, P., Breitkreuz, C., Tassinari, C.C.G., 2019. The significance of U-Pb zircon ages in zoned plutons - the case of the Flamenco pluton, Coastal Range batholith, northern Chile. Geoscience Frontiers 10 (3), 1073-1099.

Rogers, G., Hawkesworth, C.J., 1989. A geochemical traverse across the North Chilean Andes: evidence for crust generation from the mantle wedge. Earth and Planetary Science Letters 91, 271–285.

Rojas, P.A., Barra, F., Reich, M., Deditius, A., Simon, A.C., Uribe, F., Romero, R., Rojo, M., 2018. A genetic link between magnetite mineralization and diorite intrusion at the El Romeral iron oxide-apatite deposit, northern Chile. Mineralium Deposita 53, 947-966.

Rossel, P., Oliveros, V., Ducea, M., Hernandez, L., 2015. Across and along arc geochemical variations in altered volcanic rocks: Evidence from mineral chemistry of Jurassic lavas in northern Chile, and tectonic implications. Lithos 239, 97-113.

Rubatto D., Gebauer, D., 2000. Use of cathodoluminescence for U-Pb zircon dating by ion microprobe: some examples from the Western Alps. In: Pagel, M., Barbin, V., Blanc, P., Ohnenstetter, D. (eds). Cathodoluminescence in geosciences. Springer, Berlin, Heidelberg, New York, 373-400.

Scheuber, E., Andriessen, P.A.M., 1990. The kinematic and geodynamic significance of the Atacama fault zone, northern Chile. Journal of Structural Geology 12, 24-257.

Scheuber, E., Bogdanic C., T., Jensen, A. I., and Reutter, K. J., 1994, Tectonic development of the North Chilean Andes in relation to plate convergence and magmatism since the Jurassic, in Reutter, K. J., Scheuber, E., and Wigger, P. J., eds., Tectonics of the southern Central Andes; structure and evolution of an active continental margin: Berlin, Springer-Verlag, p. 121-139.

Scheuber, E., González, G., 1999. Tectonics of the Jurassic-Early Cretaceous magmatic arc of the north Chilean Coastal Cordillera (22°-26°S): A story of crustal deformation along a convergent plate boundary. Tectonics 18 (5), 895-910.

Scheuber, E., Hammerschmidt, K., Friedrichsen, H., 1995. 40Ar/39Ar and Rb-Sr analyses from ductile shear zones from the Atacama Fault Zone, Northern Chile: the age of deformation. Tectonophysics 250, 61-87.

Scholl, D. W., von Huene, R., 2007. Crustal recycling at modern subduction zones applied to the past: Issues of growth and preservation of continental basement crust, mantle geochemistry, and supercontinent reconstruction: Geological Society of America Memoirs, v. 200, p. 9-32.

Schoene, B., 2014. U-Th-Pb geochronology. In Holland, H. and Turekian, K. "Treatise on Geochemistry, 2nd Edition", 4 (10), 341-378. Elsevier.

Sernageomin, 2002. Mapa Geológico de Chile, 1:1.000.000. Servicio Nacional de Geología y Minería. Santiago, Chile.

Sillitoe, R.H., 2003. Iron oxide-copper-gold deposits: An Andean view. Mineralium Deposita 38, 787-812.

Sláma, J., Košler, J., Condon, D.J., Crowley, J.L., Gerdes, A., Hanchar, J.M., Whitehouse, M.J., 2008. Plešovice zircon - a new natural reference material for U-Pb and Hf isotopic microanalysis. Chemical Geology 249, 1-35.

Spencer, C. J., Kirkland, C.L., Taylor, R.J.M. 2016. Strategies towards statistically robust interpretations of in situ U–Pb zircon geochronology. Geoscience Frontiers, 7 (4), 581-589,

Suárez, M., Bell, C.M., 1992. Triassic rift-related sedimentary basins in northern Chile. Journal of South American Earth Sciences 6 (3), 109-121.

Sun, S.S., McDonough, W.F., 1989. Chemical and isotopic systematics of oceanic basalts; implications for mantle composition and processes. In: Magmatism in the ocean basins. Saunders, A.D. and Norry, M.J. (Editors), Geological Society of London, London 42, 313-345.

Trail, D., Watson, E.B., Tailby, N., 2012. Ce and Eu anomalies in zircon as proxies for oxidation state of magmas. Geochimica et Cosmochimica Acta 97, 70-87.

Vásquez, P., Glodny, J., Franz, G., Frei, D., Romer, R.L., 2011. Early Mesozoic Plutonism of the Cordillera de la Costa (34°–37°S), Chile: constraints on the onset of the Andean Orogeny. Journal of Geology 119 (2), 159–184.

Vivallo, W., Díaz, A., Jorquera, R., 2008. Yacimientos metalíferos de la Región de Atacama. Servicio Nacional de Geología y Minería: Santiago.

Wall, C., Scoates, J.S., Weis, D., Friedman, R.M., Amini, M., Meurer, W.P., 2018. The Stillwater Complex: Integrating zircon geochronological and geochemical constraints on the age, emplacement history and crystallization of a large, open-system layered intrusion. Journal of Petrology 59 (1), 153-190.

Wang, Q., Zhu, D.-C., Zhao, Z.-D., Guan, Q., Zhang, X.-Q., Sui, Q.-L., Hu, Z.-C., Mo, X.-X., 2012. Magmatic zircons from I-, S- and A-type granitoids in Tibet: Trace element characteristics and their application to detrital zircon provenance study. Journal of Asian Earth Sciences, 53, 59-66.

Whalen, J.B., Currie, K.L., Chappell, B.W., 1987. A-Type granites - Geochemical characteristics, discrimination and petrogenesis. Contributions to Mineralogy and Petrology 95 (4), 407-419.

Whitehouse, M. J., Kamber, B. S., 2002. On the overabundance of light rare earth elements in terrestrial zircons and its implications for Earth's earliest magmatic differentiation. Earth and Planetary Science Letters 204, 333-346.

Wiedenbeck, M., Allé, P., Corfu, F., Griffin, W.L., Meier, M., Oberli, F., Quadt, A.V., Roddick, J.C., Spiegel, W., 1995. Three natural zircon standards for U-Th-Pb, Lu-Hf, trace element and REE analyses. Geostandards Newsletter 19 (1), 1-23.

Williams, I.S., Claesson, S., 1987. Isotopic evidence for the Precambrian provenance and Caledonian metamorphism of high grade paragneisses from the Seve Nappes, Scandinavian Caledonides: II. Ion microprobe zircon U-Th-Pb. Contributions to Mineralogy and Petrology 97, 205-217.

Yang, J.H., Cawood, P.A., Du, Y.S., Huang, H., Huang, H.W., Tao, P., 2012. Large Igneous Province and magmatic arc sourced Permian-Triassic volcanogenic sediments in China. Sedimentary Geology, 261-262, 120-131.

2.9. TABLES

Table 2.1. Geographic location, age, and main characteristics of the studied plutonic complexes

Plutonic Complex	UTM Location		General description	Main rock types	Reported age (Ma)	References
	N	E				
Cerros del Vetado	7084602	353526	Ellipsoidal plutonic complex (23x10 km) with NNE main direction, emplaced in the Chañaral Epimetamorphic complex and intruded by the Las Ánimas pluton	Mg, Sg (Amp + Bt ± Msc)	246.5±4.0	Maksaev et al. (2014)
Quebrada Quiscuda	7108935	336018	An enclave in the Pan de Azucar pluton. It is a small, subrounded stock (2x3 km) which intrudes the Chañaral Epimetamorphic complex	Mg, Sg (Msc)	265-250	Godoy and Lara (1998a)
Barquito	7082952	334553	A group of small stocks of variable composition that are in contact with the Chañaral Epimetamorphic complex and the Pan de Azucar pluton	Mg (Bt + Amp)	204-193	Godoy and Lara (1998a)
Flamenco	7067843	330791	Subcircular intrusive body of 15 km in diameter, emplaced in the Chañaral Epimetamorphic complex	Gdt (Px + Amp + Bt) Tn, Md, Dqz (Px + Amp + Bt)	200-190	Godoy and Lara (1998a; 1999); Lara and Godoy (1998); Rodríguez et al. (2019)
Relincho	7030377	321993	Ellipsoidal pluton of 23 km of major axis. Emplaced in the Chañaral Epimetamorphic complex, it is intruded by tonalites from Cuevitas pluton	Tn, Gdt (Bt + Amp) Gn (Bt + Amp), Dqz (Px + Amp)	195-180	Godoy and Lara (1999)
Las Ánimas	7088509	360069	An elongated body outcropping to the west of the AFS for more than 70 km in NS orientation. To the north it intrudes La Negra Fm., and the Chañaral Epimetamorphic complex and Cerros del Vetado and Flamenco plutons to the west	Dqz (Opx + Clpx) Dt, Tn (Amp + Bt)	160-150	Godoy and Lara (1998a; 1999); Lara and Godoy (1998)
La Brea Diorite	6971145	357929	Rhomboidal, NS oriented plutonic complex with 55 km of main axis. To the north is in contact with La Borracha pluton, to the south and east with Bandurrias, Punta del Cobre, Abundancia and Nantoco Fms., and to the west with La Negra Fm. and Sierra de Atacama and Sierra Chicharra plutons	Dqz (Amp + Bt) Tn, Gdt (Amp + Bt)	123-117	Blanco et al. (2003); Arévalo (2005a)
Las Tazas	7089373	367907	Tabular, NS elongated body outcropping for more than 60 km to the west of the main fault of the AFS. To the west it intrudes the Las Ánimas pluton	Gdt (Amp + Bt) Dt (Amp + Bt)	130-125	Godoy and Lara (1998a); Lara and Godoy (1998)
Sierra Áspera	7088040	383423	Irregular, elongated intrusive body (20x13 km) emplaced to the east of the AFS. Intrudes La Negra Fm.	Dt (Px + Amp ± Bt) Gb, Mg, Tn, Gdt (Amp ± Bt)	130-125	Godoy and Lara (1998a)

Sierra Chicharra Diorite	6976912	357123	Elongated, NNE oriented body outcropping for more than 40 km in its main axis. To the north is emplaced between La Negra Fm. and the Cerro Morado pluton. To the west is in contact with Quebrada Poblete units. To the east with La Negra Fm. and La Brea Diorite and Sierra de Atacama plutons	Dqz (Amp + Bt) Tn, Gdt (Amp + Bt)	128-125	Godoy et al. (2003); Arévalo (2005a)
La Borracha	6995003	384649	Rhomboidal, NNW oriented plutonic complex with 57 km of main axis. To the SSW is in contact with La Brea Diorite pluton	Mdqz, Mqz (Amp) Mg (Amp)	114-103	Lara and Godoy (1998); Arévalo (2005a)
Sierra Atacama Diorite	6954416	353391	Elongated, NS pluton (26x9 km), in contact with Punta del Cobre and Nantoco Fms. to the east. To the west it is limited by the AFS and is in contact with Sierra Chicharra pluton	Dt, Md, Mqz (Clpx + Amp + Bt) Gb, Dt (Opx + Clpx)	117-104	Blanco et al. (2003); Arévalo (2005a; 2005b)
Sierra Pajas Blancas Granodiorite	6990033	365171	A group of irregular bodies of limited extension (<8 km^2), which intrude La Negra Fm. and Sierra Chicharra and La Brea Diorite plutonic complexes	Gdt (Amp + Bt)	108-103	Arévalo (2005a)

Notes: UTM coordinates according to Datum WGS84, Zone 19S. Main rock types from: Vivallo et al. (2008), Arévalo (2005a,b), Blanco et al. (2003), Godoy and Lara (1999; 1998) and Sernageomin (2002).

Abbreviations: Qz, quartz; Alkfs, alkali feldespars; Pl, plagioclase; Px, pyroxene; Amp, amphibole; Bt, biotite; Msc, muscovite; Opx, orthopyroxene; Clpx, clinopyroxene; Mg, monzogranite; Sg, sienogranite; Gn, granite; Gdt, granodiorite; Tn, tonalite; Dt, diorite; Gb, gabbro; Dqz, quartz diorite; Md, monzodiorite; Mqz, quartz monzonite; Mdqz, quartz monzodiorite.

Table 2.2. Sample location, main characteristics, and weighted average $^{206}Pb/^{238}U$ age for the studied plutonic complexes.

Sample ID	UTM Location N	E	Plutonic Complexes	Lithology	Textures	Modal composition (%) Qz-Kfeld-Plg-Px-Amp-Bt-Ms	Zircon U-Pb age (Ma) (MSWD; n)
JJJD_28*	7084602	353526	Cerros del Vetado	Sg (Amp ± Bt ± Msc)	Faneritic, inequigranular, euhedral to subhedral (~5 mm, up to 50 mm)	20-45-20-<1-<3-10-3	246.7 ± 3.9 (1.7, 18)
JJJD_39*	7108935	336018	Quebrada Quiscuda	Gdt (Bt ± Msc)	Faneritic, inequigranular, euhedral to subhedral (~3 mm, 30 to <2 mm)	25-13-45-a-a-10-<3	211.3 ± 1.2 (0.15, 33)
JJJD_13*	7082952	334553	Barquito	Mg (Amp ± Bt)	Faneritic, inequigranular, euhedral to anhedral (~10 mm, 30 to < 2 mm)	35-20-25-a-10-10-a	202.8 ± 1.5 (0.93; 29)
JJJD_12	7084268	336955		Gdt (Amp ± Bt)	Faneritic, inequigranular, euhedral to anhedral (~5 mm, 15 to < 0.5 mm)	20-10-45-a-15-25-a	189.6 ± 1.1 (0.62, 43)
JJJD_06	7067843	330791	Flamenco	Gdt (Bt ± Amp ± Px)	Faneritic, inequigranular, euhedral to anhedral (~5 mm, 30 to < 0.5 mm)	18-7-30-10-15-20-a	194.4 ± 0.8 (0.52, 41)
JJJD_05*	7030377	321993	Relincho	Dqz (Bt ± Amp)	Faneritic, inequigranular, euhedral to anhedral (~3 mm, 15 to < 0.5 mm)	5-1-55-a-15-25-a	192.4 ± 0.9 (0.66, 45)
JJJD_20*	7088509	360069	Las Ánimas	Dt / Dqz (Amp ± Px ± Bt)	Faneritic, inequigranular, subhedral to anhedral (~0.5 mm, 5 to < 0.2 mm)	3-5-55-<5-30-<5-a	150.2 ± 0.6 (0.87, 33)
JJJD_02*	6971145	357929	La Brea Diorite	Gdt (Amp ± Bt)	Faneritic, inequigranular, subhedral (~10 mm, 30 to < 1 mm)	15-10-30-a-40-5-a	135.2 ± 0.4 (0.75, 38)
JJJD_01*	6971145	357929		Gdt (Amp ± Bt)	Faneritic, inequigranular, subhedral (~3 mm, 10 to < 1 mm)	27-10-38-a-20-5-a	124.6 ± 1.1 (0.84, 39)
JJJD_19*	7089373	367907	Las Tazas	Gdt (Amp ± Bt)	Faneritic, inequigranular, subhedral to anhedral (<0.2 mm, 0.5 to < 0.2 mm)	18-15-40-a-18-10-a	131.7 ± 0.5 (0.98, 32)
JJJD_23	7088040	383423	Sierra Áspera	Mdqz / Gdt (Amp ± Px ± Bt)	Faneritic, equigranular, subhedral to anhedral (~1.5 mm, 2.5 to < 0.5 mm)	10-5-35-10-35-<5-a	129.6 ± 0.8 (0.88, 44)
JJJD_32	7089136	379615		Dt (Px ± Amp)	Seriated, euhedral to anhedral (~3 mm, up to 30 mm)	2-5-50-40-<3-a-a	127.5 ± 0.4 (0.85, 44)
JJJD_40	7085063	372534		Gdt (Amp ± Bt)	Faneritic, inequigranular, euhedral to anhedral (~5 mm, 30 to < 0.5 mm)	30-5-40-a-18-7-a	127.0 ± 0.7 (0.96, 40)
JJJD_33*	7088123	375297		Mg (Amp ± Bt)	Faneritic, equigranular, euhedral to anhedral (~0.5 mm)	25-20-25-a-22-8-a	125.5 ± 0.8 (0.86, 36)
JJJD_22*	7088040	383423		Gtd (Amp)	Faneritic, inequigranular, euhedral to anhedral (~2 mm, 20 to < 0.5 mm)	18-18-42-a-20-<2-a	125.4 ± 0.7 (1.1, 45)
JJJD_18*	6976912	357123	Sierra Chicharra Diorite	Gdt / Tn (Amp ± Bt)	Faneritic, inequigranular, euhedral to subhedral (~2 mm, 20 to < 0.5 mm)	25-5-35-a-30-5-a	126.9 ± 1.1 (1.5, 36)
JJJD_17	6976912	357123		Gdt (Amp ± Bt)	Faneritic, inequigranular, euhedral to subhedral (~2 mm, 20 to < 0.5 mm)	25-15-30-a-25-5-a	125.3 ± 1.2 (0.95, 32)
JJJD_24*	6995003	384649	La Borracha	Mdqz / Md (Amp ± Bt)	Faneritic, inequigranular, subhedral (~10 mm, 30 to < 1 mm)	4-20-50-a-25-<2-a	116.7 ± 0.4 (1.5, 43)
JJJD_25	6993941	380900		Mdqz (Amp ± Bt)	Seriated, euhedral to anhedral (~1	7-24-47-a-20-<2-a	115.3 ± 0.9

					mm, 10 to < 0.2 mm)		(1.3, 33)
JJJD_03*	7005980	371794		Mdqz / Md (Amp ± Bt)	Seriated, euhedral to subhedral (~1 mm, 15 to < 0.5 mm)	3-17-35-a-40-5-a	113.1 ± 0.7 (2.8, 39)
JJJD_04	7005980	371794		Dqz / Mdqz (Amp ± Bt)	Faneritic, inequigranular, euhedral to subhedral (~5 mm, 15 to < 0.5 mm)	4-<3-18-a-42-33-a	111.6 ± 0.6 (0.86, 23)
JJJD_36*	7010485	371423		Mg / Aplite (Msc ± Bt ± Amp)	Faneritic, equigranular, subhedral to anhedral (~0.1 mm)	40-30-15-a-<2-<2-12	105.0 ± 3.0 (0.11, 37)
JJJD_09*	6954416	353391	Sierra Atacama Diorite	Gb (Amp ± Px ± Bt)	Faneritic, inequigranular, euhedral to subhedral (~10 mm, 20 to < 2 mm)	3-<1-50-15-25-7-a	114.8 ± 0.5 (1.3, 45)
JJJD_11	6955952	354438		Dt / Dqz (Bt ± Amp ± Px)	Faneritic, inequigranular, euhedral to subhedral (~5 mm, 15 to < 1 mm)	2-1-42-10-20-25-a	114.6 ± 0.3 (0.85, 45)
JJJD_08B	6954416	353391		Mdqz (Amp ± Px ± Bt)	Faneritic, equigranular, euhedral to subhedral (~15 mm)	6-7-35-10-35-7-a	114.5 ± 0.6 (0.88, 16)
JJJD_10	6955952	354438		Dqz (Bt ± Amp ± Px)	Faneritic, equigranular, euhedral to subhedral (~10 mm, 20 to < 2 mm)	<3-<3-40-10-20-25-a	113.9 ± 0.5 (1.6, 42)
JJJD_08	6954416	353391		Mdqz (Amp ± Px ± Bt)	Faneritic, inequigranular, euhedral to subhedral (~15 mm, 25 to < 5 mm)	3-5-38-12-35-7-a	111.6 ± 0.6 (0.45, 27)
JJJD_29	6990033	365171	Sierra Pajas Blancas	Gdt (Amp ± Bt)	Seriated, euhedral to anhedral (~1 mm, 10 to < 0.2 mm)	20-7-38-a-25-10-a	110.4 ± 2.8 (0.79, 25)
JJJD_30	6990033	365171		Gdt (Amp ± Bt)	Seriated, euhedral to anhedral (~2 mm, 10 to < 0.5 mm)	20-7-43-a-21-8-a	99.6 ± 1.5 (1.4, 41)
JJJD_31*	6990033	365171		Gdt / Tn (Amp ± Bt)	Seriated, euhedral to anhedral (~1 mm, 5 to < 0.2 mm)	15-5-45-a-25-10-a	99.2 ± 0.7 (1.1, 36)

*: Indicates samples analyzed for zircon U-Pb geochronology/trace element and whole-rock geochemistry.

Abbreviations: Qz, quartz; Alkfs, alkali feldespars; Pl, plagioclase; Px, pyroxene; Amp, amphibole; Bt, biotite; Msc, muscovite; Opx, orthopyroxene; Clpx, clinopyroxene; Mg, monzogranite; Sg, sienogranite; Gn, granite; Gdt, granodiorite; Tn, tonalite; Dt, diorite; Gb, gabbro; Dqz, quartz diorite; Md, monzodiorite; Mqz, quartz monzonite; Mdqz, quartz monzodiorite. a: absent.

Table 2.3. Whole-rock major, minor and trace elements geochemical data for the studied plutonic complexes

Sample	JJJD_28	JJJD_39	JJJD_13	JJJD_05	JJJD_20	JJJD_02	JJJD_19	JJJD_18	JJJ_33
Unit	Cerros del Vetado	Quebrada Quiscuda	Barquito	Relincho	Las Ánimas	La Brea Diorite	Las Tazas	Sierra Chicharra Diorite	Sierra Áspera
Petrography	Syenogranite	Granodiorite	Monzogranite	Quartz diorite	Diorite	Granodiorite	Granodiorite	Granodiorite	Monzogranite
Age	E-M Triassic (247 Ma)	Late Triassic (211 Ma)	Late Triassic (203 Ma)	Early Jurassic (192 Ma)	Late Jurassic (150 Ma)	Valanginian (EKr) (135 Ma)	Hauterivian (EKr) (132 Ma)	Barremian (EKr) (127 Ma)	Barremian (EKr) (126 Ma)
Major oxides (wt%)									
SiO_2	71.03	65.53	74.84	57.00	55.87	67.94	66.11	63.16	71.37
Al_2O_3	15.08	16.62	13.53	20.70	17.63	15.32	16.51	16.90	13.56
FeO*(t)	1.51	3.80	1.76	5.04	3.61	3.71	3.55	3.12	3.18
MnO	0.02	0.07	0.05	0.08	0.14	0.06	0.08	0.07	0.06
MgO	0.39	2.02	0.59	1.69	4.13	1.46	1.43	3.13	0.90
CaO	1.63	4.62	1.80	8.58	9.91	3.79	3.69	7.21	2.45
Na_2O	3.08	4.15	4.12	3.00	5.05	3.73	4.12	4.38	3.29
K_2O	6.06	1.36	2.19	1.01	0.53	2.60	2.60	0.36	3.83
TiO_2	0.24	0.51	0.19	1.04	0.88	0.44	0.44	0.66	0.48
P_2O_5	0.07	0.12	0.06	0.27	0.02	0.09	0.13	0.14	0.07
LOI	0.13	0.87	0.52	0.94	1.61	0.68	0.87	0.66	0.34
Total	99.24	99.66	99.65	99.36	99.37	99.82	99.52	99.78	99.53
Minor and trace elements (ppm)									
Sc	4.95	8.31	3.03	15.01	27.08	9.61	7.20	19.69	9.66
V	17.20	77.31	18.91	161.47	142.96	70.65	70.19	135.14	58.11
Cr	7.80	24.68	5.94	7.82	9.31	5.27	8.81	29.11	5.77
Ni	2.50	13.43	4.36	7.62	12.57	4.78	10.69	9.90	2.99
Cu	3.50	3.98	1.29	18.71	75.34	20.99	42.67	5.45	27.46
Zn	14.60	51.54	36.73	52.67	107.32	19.70	46.83	21.29	26.47
Ga	15.70	19.30	16.43	19.11	19.31	14.93	16.73	18.02	14.23
Rb	255.14	33.29	57.72	31.73	13.19	51.69	70.89	6.82	116.44
Sr	87.65	394.33	173.57	290.88	505.83	256.99	428.02	417.72	159.95
Y	74.95	16.40	13.31	22.98	39.03	26.17	17.20	27.21	44.29
Zr	123.43	134.04	89.20	89.34	72.86	157.62	147.98	126.78	269.55
Nb	7.39	4.54	4.36	6.15	4.00	5.00	4.31	3.65	5.82
Cs	4.81	1.39	1.96	2.14	1.45	1.80	3.07	1.49	1.58
Ba	571.58	268.84	359.87	186.93	190.20	377.20	423.93	78.99	430.45
Hf	3.65	3.77	2.92	2.59	2.17	4.63	4.09	3.55	7.95
Ta	0.79	0.43	0.37	0.49	0.20	0.46	0.36	0.28	0.58
Pb	14.98	5.04	10.50	4.37	14.72	3.82	7.35	1.72	5.71
Th	14.87	5.70	6.14	4.49	3.71	8.68	6.64	3.55	17.70

U	1.94	0.62	0.98	0.88	1.14	1.60	1.89	0.92	2.31
La	28.77	15.86	18.37	16.38	14.71	14.38	17.13	17.35	20.23
Ce	62.20	32.31	37.16	33.17	46.91	32.61	37.07	37.30	47.76
Pr	7.76	3.91	4.32	4.04	6.80	4.35	4.73	4.67	6.56
Nd	29.34	15.04	15.07	15.89	29.30	17.78	18.12	19.26	27.22
Sm	8.04	3.06	2.91	3.81	7.41	4.25	3.81	4.55	6.94
Eu	0.74	0.96	0.61	1.27	1.54	1.00	0.92	1.40	0.86
Gd	9.65	3.00	2.48	4.11	7.61	4.23	3.33	4.65	7.20
Tb	1.89	0.49	0.41	0.70	1.29	0.72	0.53	0.79	1.26
Dy	12.82	3.01	2.41	4.28	7.74	4.58	3.21	5.00	8.05
Ho	2.77	0.62	0.48	0.90	1.59	0.97	0.64	1.03	1.67
Er	7.77	1.76	1.33	2.44	4.24	2.81	1.77	2.91	4.68
Tm	1.08	0.26	0.21	0.35	0.62	0.44	0.26	0.43	0.69
Yb	5.96	1.68	1.40	2.11	3.74	2.84	1.68	2.76	4.35
Lu	0.85	0.27	0.23	0.34	0.59	0.46	0.27	0.45	0.70
ΣREE	179.62	82.23	87.40	89.78	134.08	91.41	93.47	102.57	138.18
Rb/Sr	2.91	0.08	0.33	0.11	0.03	0.20	0.17	0.02	0.73
U/Th	0.13	0.11	0.16	0.20	0.31	0.18	0.28	0.26	0.13
Sr/Y	1.17	24.04	13.04	12.66	12.96	9.82	24.88	15.35	3.61
La_N/Lu_N	3.49	6.15	8.12	4.98	2.58	3.24	6.49	3.98	3.01
Eu_N/Eu^*	0.25	0.97	0.70	0.98	0.63	0.72	0.79	0.93	0.37

Normalizing values are from Sun and McDonough (1989). Eu* = SQRT (Sm_N*Gd_N)

Table 2.3. Whole-rock major, minor and trace elements geochemical data for the studied plutonic complexes (continued)

Sample	JJJD_22	JJJD_01	JJJD_24	JJJD_09	JJJD_03	JJJD_36	JJJD_31
Unit	Sierra Áspera	La Brea Diorite	La Borracha	Sierra Atacama Diorite	La Borracha	La Borracha	Pajas Blancas Granodiorite
Petrography	Granodiorite	Granodiorite	Monzodiorite	Gabbro	Quartz monzodiorite	Syenogranite / Aplite	Granodiorite
Age	Barremian (EKr) (125.4 Ma)	Aptian (EKr) (124.6 Ma)	Aptian (EKr) (116.7 Ma)	Aptian (EKr) (114.8 Ma)	Aptian (EKr) (113.1 Ma)	Albian (EKr) (105.0 Ma)	Cenomanian (LKr) (99.2 Ma)
Major oxides (wt%)							
SiO_2	67.21	69.36	52.69	50.25	56.32	72.37	62.32
Al_2O_3	17.61	15.74	16.75	17.74	18.55	15.15	17.41
FeO*(t)	1.57	1.54	8.55	9.88	5.85	0.82	4.82
MnO	0.45	0.03	0.16	0.16	0.04	0.01	0.12
MgO	0.10	1.70	3.65	4.75	3.67	0.64	1.88
CaO	4.45	5.75	6.36	9.07	6.22	3.10	5.75
Na_2O	5.31	4.42	5.08	3.31	4.68	5.94	3.72
K_2O	0.44	0.22	2.45	1.15	1.63	0.20	2.16
TiO_2	1.80	0.47	1.11	1.17	0.71	0.27	0.45
P_2O_5	0.01	0.10	0.39	0.48	0.10	0.09	0.15
LOI	0.54	0.49	2.07	1.38	1.93	0.99	0.61
Total	99.51	99.82	99.27	99.35	99.70	99.59	99.39
Minor and trace elements (ppm)							
Sc	0.12	10.91	23.83	30.21	17.63	2.98	7.85
V	45.14	38.90	205.13	307.00	182.16	31.84	108.10
Cr	29.90	5.47	17.33	15.94	18.91	4.28	2.00
Ni	3.17	8.36	10.30	13.07	19.11	0.20	0.00
Cu	12.77	8.46	178.00	43.96	82.86	4.48	25.50
Zn	20.69	7.56	61.28	53.86	7.82	1.89	32.80
Ga	17.82	14.83	18.12	20.59	18.71	15.12	18.80
Rb	7.57	3.02	69.73	29.82	51.49	4.02	44.94
Sr	538.38	348.19	372.79	652.13	554.12	398.61	542.50
Y	6.06	28.21	30.74	28.62	15.61	10.70	15.68
Zr	292.70	160.26	245.03	93.41	113.98	131.49	99.10
Nb	6.13	6.12	12.93	3.54	5.05	4.97	3.61
Cs	0.50	0.21	33.33	0.67	1.68	0.64	1.08
Ba	155.15	72.28	922.26	390.29	366.15	191.48	599.24
Hf	7.71	4.77	6.16	2.63	3.17	3.44	2.80
Ta	0.97	0.58	0.86	0.23	0.43	0.46	0.35
Pb	1.68	1.44	8.64	3.11	4.05	1.34	3.78
Th	0.73	9.16	11.95	2.30	9.44	8.99	3.23

U	0.62	1.66	1.95	0.82	1.56	2.00	1.47
La	6.72	8.19	32.71	18.74	15.93	12.59	15.92
Ce	10.90	22.60	67.58	44.15	32.73	25.95	31.82
Pr	1.25	3.52	8.97	6.49	4.15	3.21	4.02
Nd	4.70	15.84	36.43	29.28	16.29	11.70	15.93
Sm	1.01	4.20	7.84	6.97	3.50	2.36	3.36
Eu	1.06	1.01	1.91	1.95	1.14	0.74	1.10
Gd	1.02	4.47	6.77	6.50	3.13	1.99	3.04
Tb	0.17	0.75	1.03	0.97	0.50	0.31	0.47
Dy	1.07	4.95	5.95	5.56	2.95	1.88	2.86
Ho	0.24	1.03	1.20	1.13	0.60	0.39	0.59
Er	0.74	2.95	3.27	2.99	1.70	1.10	1.67
Tm	0.11	0.45	0.48	0.43	0.25	0.17	0.26
Yb	0.79	2.88	3.03	2.56	1.62	1.14	1.69
Lu	0.13	0.48	0.50	0.39	0.26	0.19	0.27
ΣREE	29.92	73.32	177.66	128.10	84.77	63.71	82.99
Rb/Sr	0.01	0.01	0.19	0.05	0.09	0.01	0.08
U/Th	0.85	0.18	0.16	0.36	0.16	0.22	0.46
Sr/Y	88.82	12.34	12.13	22.78	35.49	37.25	34.61
La_N/Lu_N	5.23	1.76	6.85	4.98	6.27	6.75	6.07
Eu_N/Eu^*	3.18	0.71	0.80	0.88	1.05	1.04	1.05

Normalizing values are from Sun and McDonough (1989). Eu* = SQRT (Sm_N*Gd_N)

Table 2.4. Summary of LA-ICP-MS trace element data of zircon grains from the analyzed plutonic complexes

(ppm)	P	Ti*	Cr	Fe	Y	Nb	Hf	Ta	Th	U	La	Ce	Pr	Nd	Sm
Early to Middle Triassic sample: JJJD_28 (n = 19)															
Mean	832	4.81	2.67	63.1	2581	2.24	14487	2.11	135	1892	0.67	5.56	0.49	3.22	5.53
SD	289	2.33	2.61	52.5	837	1.11	1698	1.27	66	1401	1.13	7.08	0.90	4.13	3.13
$P_{5\%}$	558	1.01	0.50	2.0	1673	0.83	12016	0.71	48	870	0.01	0.80	0.01	0.62	2.89
Median	774	4.57	1.90	51.0	2370	1.84	14600	1.96	138	1450	0.12	2.48	0.11	1.31	4.66
$P_{95\%}$	1184	9.22	7.08	156.0	4122	4.63	17150	5.06	264	4906	2.98	18.78	2.65	13.44	12.53
Count (n)	19	19	13	13	19	19	19	19	19	19	15	19	19	19	19
Late Triassic samples: JJJD_39 (n = 33) and JJJD_13 (n = 29)															
Mean	280	6.50	0.74	10.2	962	1.26	11596	0.64	77	134	0.10	9.65	0.05	0.98	2.22
SD	219	2.54	0.48	20.0	432	0.95	2314	0.41	46	93	0.19	4.85	0.07	0.82	1.26
$P_{5\%}$	124	3.63	0.10	0.5	515	0.40	9174	0.23	23	45	0.00	3.30	0.00	0.38	1.00
Median	209	6.01	0.69	4.0	869	0.93	11605	0.53	71	112	0.02	9.05	0.03	0.65	1.88
$P_{95\%}$	716	10.67	1.42	47.8	1762	2.92	14343	1.39	149	305	0.54	18.58	0.14	2.47	4.10
Count (n)	62	62	45	42	62	62	62	62	62	62	26	62	60	62	62
Early Jurassic samples: JJJD_06 (n = 41), JJJD_05 (n = 45) and JJJD_12 (n = 43)															
Mean	249	7.37	0.99	7.7	1165	1.46	13004	0.80	64	100	0.07	6.04	0.06	1.06	2.93
SD	68	2.39	0.62	8.1	510	0.57	1615	0.25	39	45	0.17	2.08	0.06	0.95	2.08
$P_{5\%}$	150	4.03	0.20	0.9	533	0.68	10940	0.43	19	41	0.00	3.11	0.00	0.20	0.78
Median	242	7.16	0.90	5.6	1077	1.35	12740	0.77	56	94	0.02	5.82	0.03	0.74	2.26
$P_{95\%}$	358	11.81	2.19	23.8	2050	2.33	15800	1.23	122	188	0.26	9.75	0.20	3.01	7.12
Count (n)	129	129	82	59	129	129	129	129	129	129	42	129	120	129	129
Late Jurassic sample: JJJD_20 (n = 33)															
Mean	558	12.41	0.83	15.6	3311	2.66	15111	1.46	310	289	0.02	25.08	0.20	4.03	10.29
SD	95	2.58	0.76	24.3	1001	0.79	1501	0.32	157	101	0.03	8.56	0.09	1.87	4.07
$P_{5\%}$	401	8.71	0.10	0.8	2194	1.53	12682	1.03	123	173	0.01	14.34	0.07	1.71	5.53
Median	558	12.10	0.50	7.3	2970	2.63	15230	1.54	253	279	0.01	25.67	0.19	4.07	9.71
$P_{95\%}$	675	17.00	2.15	57.5	5342	3.76	17142	1.92	549	443	0.04	38.61	0.36	7.73	18.49
Count (n)	33	33	19	16	33	33	33	33	33	33	22	33	33	33	33
Valanginian to Hauterivian samples: JJJD_02 (n = 37), JJJD_19 (n = 29) and JJJD_23 (n = 44)															
Mean	332	11.46	1.04	19.6	1533	2.33	12537	1.49	415	399	0.08	20.76	0.19	2.91	6.20
SD	188	4.06	0.75	26.1	1155	1.25	2523	0.76	489	367	0.22	14.10	0.21	3.09	5.92
$P_{5\%}$	152	5.88	0.11	1.2	362	0.83	8531	0.76	76	50	0.00	9.67	0.00	0.11	0.52
Median	279	10.90	0.80	11.0	1156	2.25	12590	1.20	202	238	0.03	14.36	0.11	1.71	4.17
$P_{95\%}$	588	18.38	2.46	73.1	3991	4.77	16746	2.91	1227	1099	0.22	48.28	0.61	9.54	17.64
Count (n)	107	110	67	83	110	110	110	110	110	110	52	110	97	110	110
Barremian to Aptian samples: JJJD_32 (n = 42), JJJD_40 (n = 39), JJJD_18 (n = 36), JJJD_33 (n = 33), JJJD_22 (n = 45), JJJD_17 (n = 32), JJJD_01 (n = 39), JJJD_24 (n=43), JJJD_25 (n = 33), JJJD_09 (n = 45), JJJD_11 (n = 44), JJJD_08B (n = 16), JJJD_10 (n = 42) and JJJD_03 (n = 39)															
Mean	370	12.70	1.00	13.0	1494	2.30	13260	1.20	251	340	0.04	13.00	0.18	3.10	6.50
SD	536	7.60	0.90	25.0	1090	1.20	3442	0.80	288	320	0.06	9.80	0.23	3.70	6.80
P5%	142	4.70	0.10	1.0	429	0.80	7464	0.50	31	54	0.00	4.80	0.01	0.30	0.80
Median	287	10.50	0.80	6.0	1207	2.10	13400	1.00	151	222	0.02	10.00	0.08	1.60	4.20
P95%	711	26.30	2.60	62.0	3393	4.60	18047	2.60	902	1010	0.16	32.10	0.73	11.40	20.40

Count (n)	527	528	324	290	528	528	528	528	528	528	268	528	516	527	528
Albian to Cenomanian samples: JJJD_08 (n = 27), JJJD_04 (n = 23), JJJD_29 (n = 23), JJJD_36 (n = 37), JJJD_30 (n=41) and JJJD_31 (n=36)															
Mean	240	12.50	3.10	23.0	1012	1.70	12330	0.90	243	238	0.20	12.50	0.12	1.70	3.70
SD	117	8.90	4.20	25.0	736	0.90	2658	0.40	451	277	0.70	7.50	0.14	1.80	3.40
P5%	77	3.60	0.10	1.0	298	0.70	8199	0.50	28	51	0.00	4.50	0.01	0.10	0.40
Median	237	9.60	1.50	12.0	785	1.50	12340	0.90	83	137	0.02	11.20	0.07	1.10	2.40
P95%	437	28.20	14.00	77.0	2394	3.20	16249	1.60	1137	847	0.94	25.50	0.39	5.30	10.60
Count (n)	187	182	120	107	187	187	187	187	187	187	97	187	166	186	187

Ti* = ^{49}Ti. Ce_N* = SQRT (La_N*Pr_N); Eu_N* = SQRT (Sm_N*Gd_N); normalizing values are from Sun and McDonough (1989).

Table 2.4. Summary of LA-ICP-MS trace element data of zircon grains from the analyzed plutonic complexes (continued)

	Eu	Gd	Tb	Dy	Ho	Er	Tm	Yb	Lu	ΣREE	Ce_N/Ce_N*	Eu_N/Eu_N*	Th/U	U/Yb	Gd/Yb
Early to Middle Triassic sample: JJJD_28 (n = 19)															
Mean	0.17	38.2	16.5	225	88.3	406	90.8	849	148	1877	7.70	0.03	0.26	0.65	0.05
SD	0.18	14.4	5.3	70	28.3	134	34.3	345	56	671	6.16	0.02	0.12	0.19	0.02
$P_{5\%}$	0.05	21.9	9.5	135	56.1	266	60.5	549	88	1258	1.66	0.01	0.12	0.47	0.03
Median	0.09	37.4	15.7	219	81.7	364	78.1	720	131	1681	6.98	0.02	0.24	0.59	0.04
$P_{95\%}$	0.55	71.6	26.2	319	137.3	662	157.2	1440	276	3066	17.22	0.07	0.50	1.06	0.08
Count (n)	19	19	19	19	19	19	19	19	19	19	15	19	19	19	19
Late Triassic samples: JJJD_39 (n = 33) and JJJD_13 (n = 29)															
Mean	0.87	14.8	5.8	75	32.5	162	38.4	442	85	869	113.4	0.47	0.60	0.29	0.03
SD	0.47	7.8	3.0	38	17.3	88	18.4	238	39	445	114.7	0.09	0.14	0.12	0.01
$P_{5\%}$	0.43	7.1	2.8	40	16.5	82	20.0	214	42	447	9.4	0.35	0.41	0.16	0.02
Median	0.70	12.6	4.9	65	29.4	141	34.5	383	76	758	54.9	0.46	0.60	0.26	0.03
$P_{95\%}$	1.86	27.9	11.9	147	63.4	316	64.7	891	145	1665	347.2	0.65	0.85	0.53	0.05
Count (n)	62	62	62	62	62	62	62	62	62	62	25	62	62	62	62
Early Jurassic samples: JJJD_06 (n = 41), JJJD_05 (n = 45) and JJJD_12 (n = 43)															
Mean	0.67	20.6	8.1	107	43.9	208	46.3	461	93	999	101.2	0.31	0.61	0.22	0.04
SD	0.41	12.6	4.6	57	21.8	94	17.8	148	29	381	125.1	0.12	0.14	0.07	0.02
$P_{5\%}$	0.28	6.1	2.7	36	16.9	85	23.5	270	57	501	6.3	0.18	0.39	0.13	0.02
Median	0.59	18.7	7.2	98	40.2	193	44.6	437	88	957	54.2	0.28	0.57	0.21	0.04
$P_{95\%}$	1.31	41.3	16.0	202	83.3	392	81.6	786	154	1777	377.7	0.52	0.84	0.35	0.07
Count (n)	129	129	129	129	129	129	129	129	129	129	40	129	129	129	129
Late Jurassic sample: JJJD_20 (n = 33)															
Mean	1.60	69.8	26.2	334	131.3	593	124.1	1131	213	2664	137.0	0.18	1.03	0.25	0.06
SD	0.73	27.8	9.9	118	43.6	184	36.6	311	56	795	82.0	0.02	0.20	0.06	0.01
$P_{5\%}$	0.83	39.1	15.4	201	81.5	379	82.2	792	150	1741	65.0	0.15	0.72	0.19	0.05
Median	1.41	62.9	23.4	301	117.1	529	112.5	1022	192	2413	99.6	0.18	1.02	0.24	0.06
$P_{95\%}$	3.17	129.6	47.4	581	221.5	972	200.0	1766	326	4291	299.0	0.20	1.28	0.34	0.07
Count (n)	33	33	33	33	33	33	33	33	33	33	22	33	33	33	33
Valanginian to Hauterivian samples: JJJD_02 (n = 37), JJJD_19 (n = 29) and JJJD_23 (n = 44)															
Mean	0.56	35.4	12.7	152	56.9	249	53.4	494	86	1170	102.6	0.12	1.21	0.77	0.06
SD	0.68	33.0	11.5	132	47.0	195	37.9	313	55	841	107.6	0.07	0.99	0.48	0.02
$P_{5\%}$	0.06	3.8	1.9	25	11.3	56	15.4	177	29	329	20.6	0.05	0.43	0.27	0.02
Median	0.33	23.7	8.9	104	39.3	168	39.1	398	66	851	62.3	0.10	0.96	0.69	0.06
$P_{95\%}$	1.56	106.6	36.8	430	157.1	663	132.3	1130	198	2901	310.9	0.26	3.01	1.60	0.10
Count (n)	108	110	110	110	110	110	110	110	110	110	52	108	110	110	110
Barremian to Aptian samples: JJJD_32 (n = 42), JJJD_40 (n = 39), JJJD_18 (n = 36), JJJD_33 (n = 33), JJJD_22 (n = 45), JJJD_17 (n = 32), JJJD_01 (n = 39), JJJD_24 (n=43), JJJD_25 (n = 33), JJJD_09 (n = 45), JJJD_11 (n = 44), JJJD_08B (n = 16), JJJD_10 (n = 42) and JJJD_03 (n = 39)															
Mean	0.90	36.0	12.0	144	56.0	248	55.0	528	100	1202	88.9	0.22	0.69	0.68	0.06
SD	0.80	38.0	10.0	122	45.0	174	37.0	323	55	809	100.9	0.11	0.22	0.74	0.02
P5%	0.20	6.0	2.0	33	14.0	71	18.0	189	40	393	11.3	0.07	0.39	0.16	0.03
Median	0.60	25.0	9.0	110	43.0	205	47.0	460	91	1015	58.0	0.19	0.68	0.52	0.05
P95%	2.20	89.0	29.0	346	128.0	582	125.0	1123	204	2668	280.7	0.40	1.07	1.52	0.10

Count (n)	528	528	528	528	528	528	528	528	528	528	267	528	528	528	528
Albian to Cenomanian samples: JJJD_08 (n = 27), JJJD_04 (n = 23), JJJD_29 (n = 23), JJJD_36 (n = 37), JJJD_30 (n=41) and JJJD_31 (n=36)															
Mean	0.90	20.0	7.0	84	34.0	160	38.0	409	78	848	103.3	0.40	0.74	0.56	0.05
SD	0.70	16.0	5.0	65	25.0	109	24.0	236	41	521	101.6	0.21	0.36	0.50	0.02
P5%	0.20	4.0	2.0	21	9.0	50	14.0	170	32	306	7.8	0.12	0.39	0.15	0.02
Median	0.70	14.0	5.0	65	26.0	131	32.0	342	67	708	75.5	0.39	0.62	0.44	0.04
P95%	2.40	55.0	18.0	215	84.0	350	84.0	825	152	1788	273.0	0.72	1.63	1.42	0.09
Count (n)	187	187	187	187	187	187	187	187	187	187	93	187	187	187	187

Ti* = ^{49}Ti. Ce_N* = SQRT (La_N*Pr_N); Eu_N* = SQRT (Sm_N*Gd_N); normalizing values are from Sun and McDonough (1989).

2.10. FIGURES

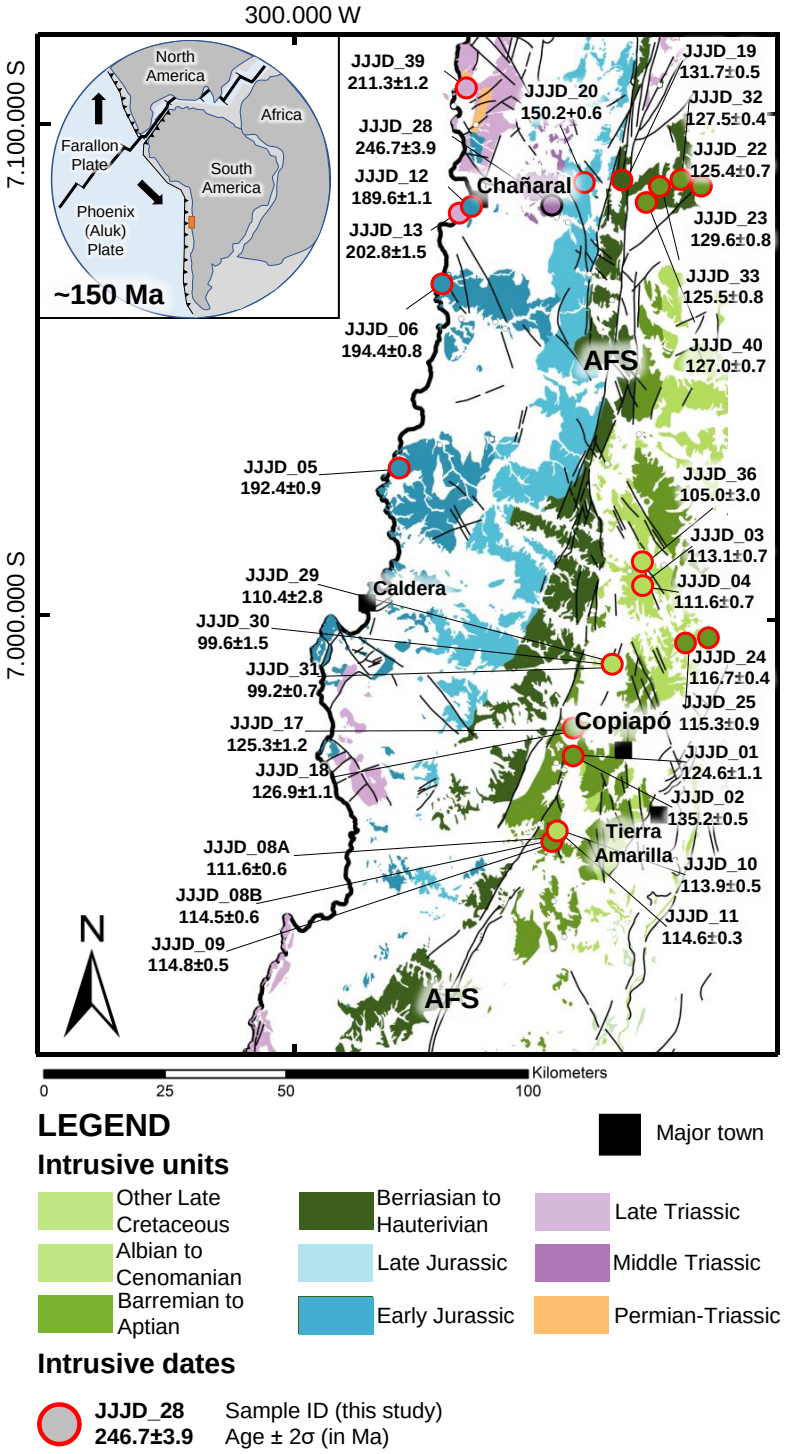

Figure 2.1. Distribution of plutonic complexes in the study area (Modified after Vivallo et al., 2008 and Sernageomin, 2002). Sample locations and their ages are indicated. AFS, Atacama Fault System. Insets show the location of the study area in relation to the geotectonic setting of the Andean margin at ca. 150 Ma.

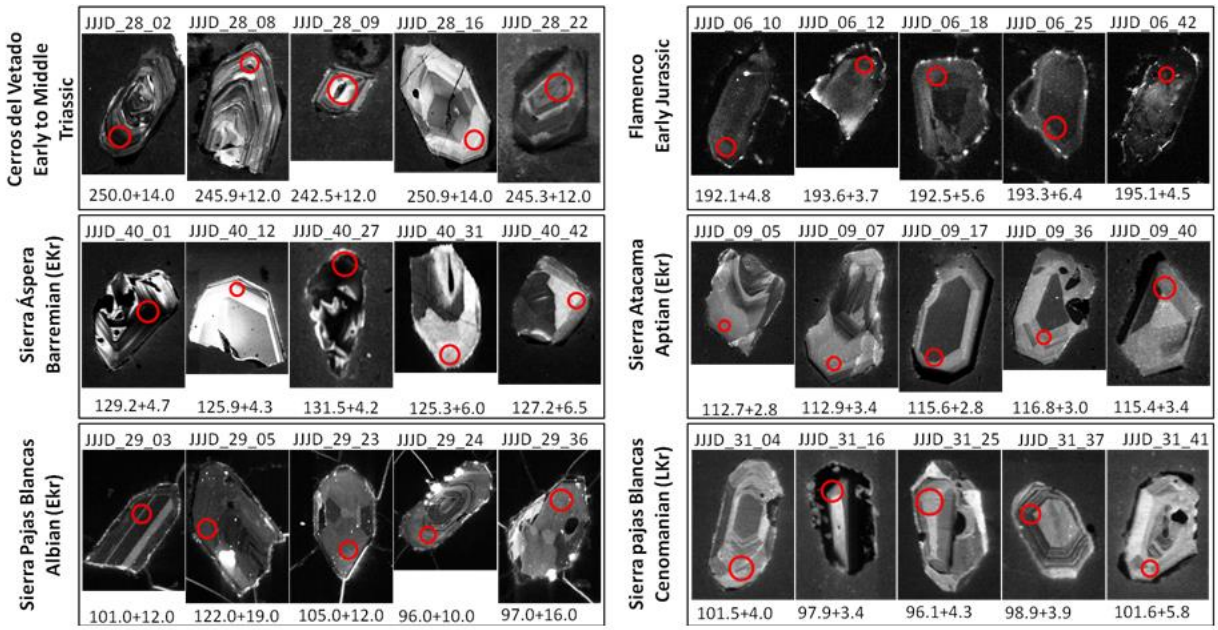

Figure 2. Representative cathodoluminescence (CL) images of analyzed zircons from plutonic complexes in the Coastal Cordillera of northern Chile. Location of laser ablation spots for simultaneous U-Pb and trace element analyses are shown with $^{206}Pb/^{238}U$ age data (in Ma). Laser ablation spot size = 50 µm.

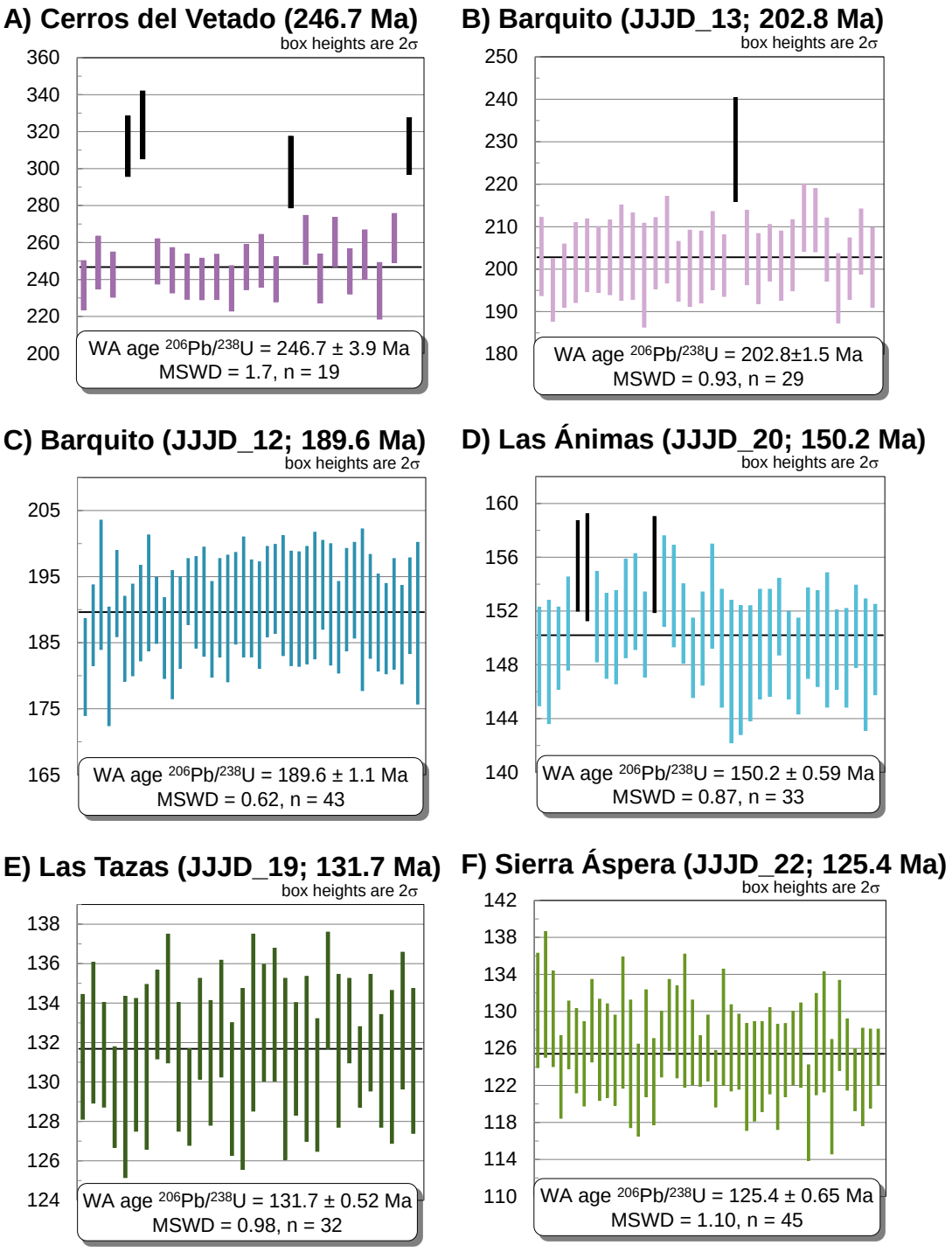

Figure 2.3. U-Pb weighted mean age plots for zircons of selected samples from the Chañaral transect. MSWD – mean square of weighted deviates. Analyses represented by black bars in weighted mean plots were excluded from age calculations.

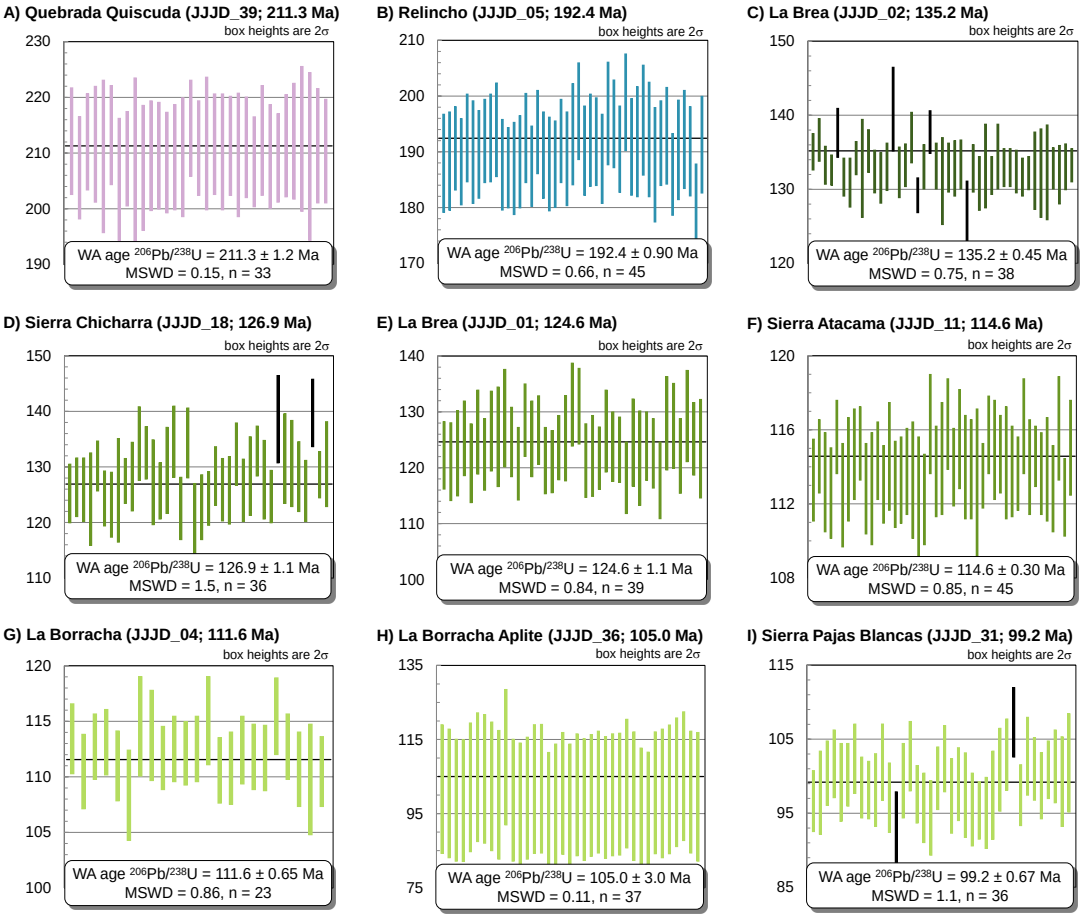

Figure 4. U-Pb weighted mean age plots for zircons from selected intrusive rocks south and north from the Chañaral transect. MSWD – mean square of weighted deviates. Analyses represented by black bars in weighted mean plots were excluded from age calculations.

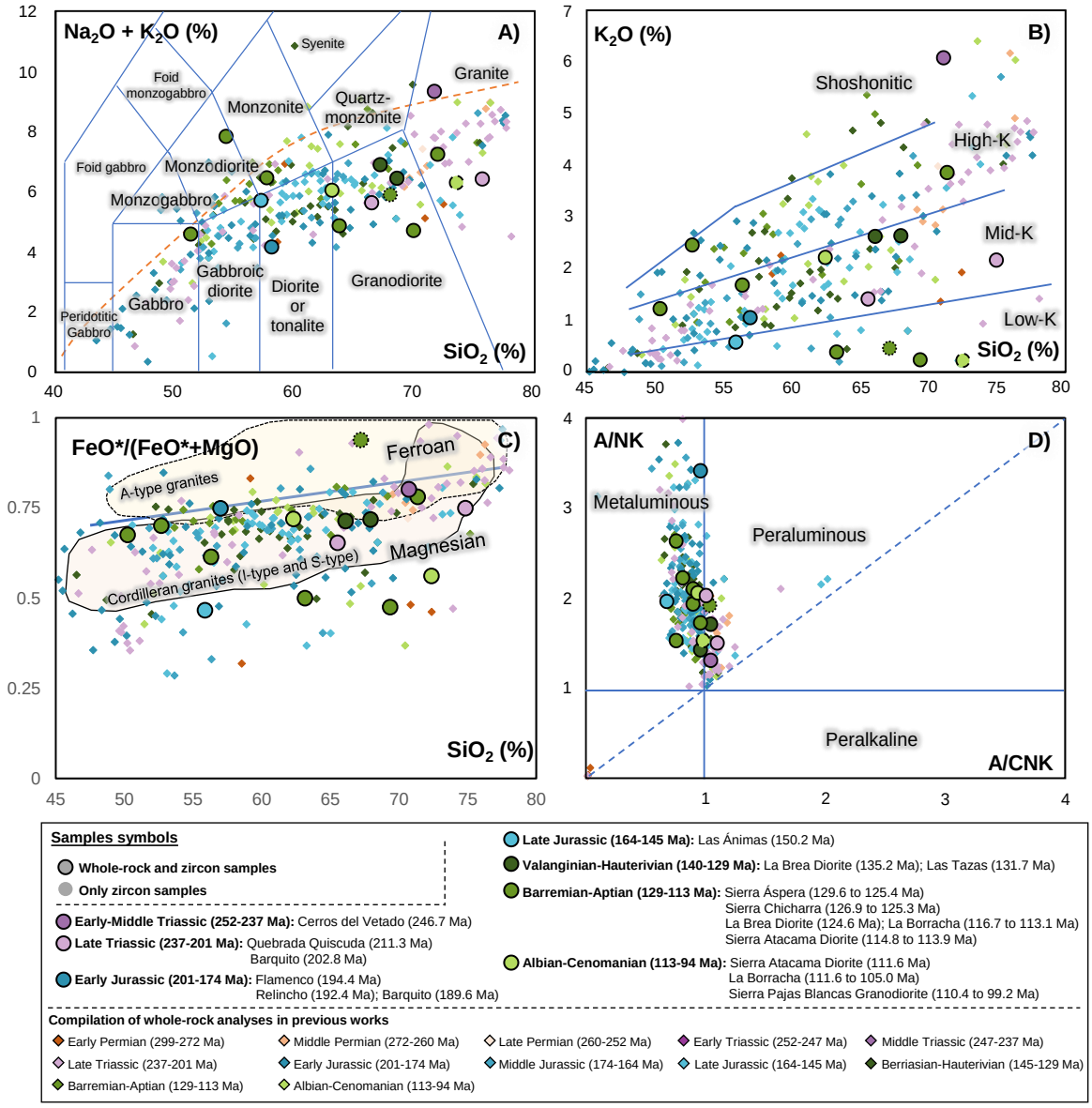

Figure 5. Plutonic rocks classification diagrams. A) Total alkali versus silica classification plot (Middlemost, 1994). The line between alkaline and sub-alkaline series is from Irvine and Baragar (1971). B) SiO_2 vs K_2O diagram of Peccerillo and Taylor (1976) showing shoshonitic and high-, mid- and low-K fields. C) SiO_2 vs FeO*/(FeO*+MgO) plot of Frost et al. (2001) showing that all but the altered sample have a magnesian affinity. D) Molar A/CNK versus molar A/NK plot showing the metaluminous to slightly peraluminous nature of the studied intrusive bodies. Symbol colors refer to the age of the plutonic complexes. Dashed circle line is of the aplitic dike from La Borracha pluton. Dotted circle outline represents the altered sample from the Sierra Áspera complex. Compiled whole-rock data in Table SM4.

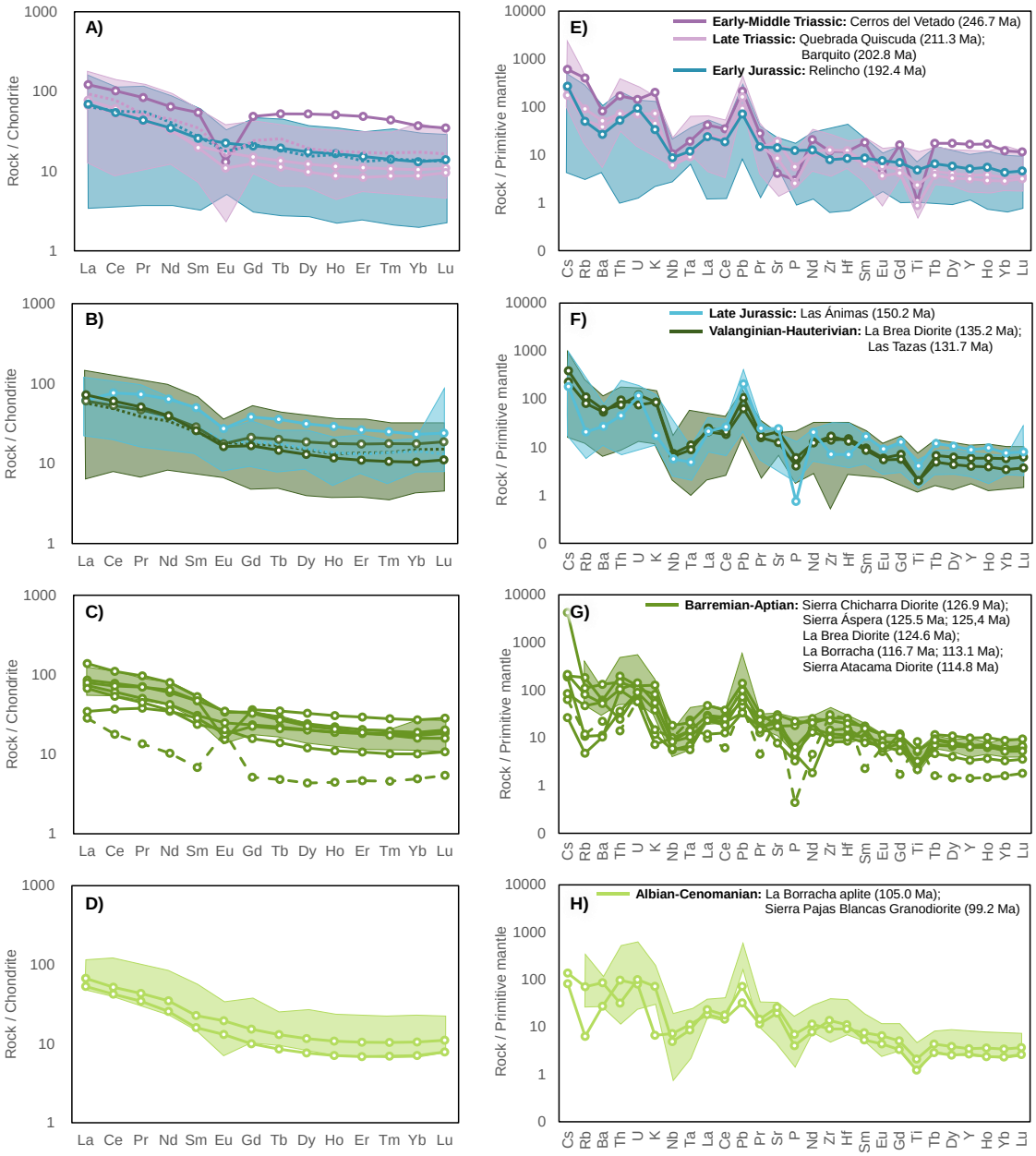

Figure 6. Chondrite-normalized rare earth elements plots (A-D) and primitive mantle-normalized minor/trace elements (E-H) diagrams for the studied intrusive complexes. Samples are grouped in Triassic and Early Jurassic samples (A and E); Late Jurassic and Valanginian to Hauterivian samples (~140-130 Ma; B and F); Barremian to Aptian (~130-113 Ma; C and G); and Albian to Cenomanian (~113-94 Ma; D and H). Dashed line in C and G represents the Sierra Áspera altered sample. Shaded areas represent 5 to 95 percentile range for each group of compiled whole-rock analyses (Table SM4); dashed lines in A and B refer to the median value for each group. Normalizing values are from Sun and McDonough (1989).

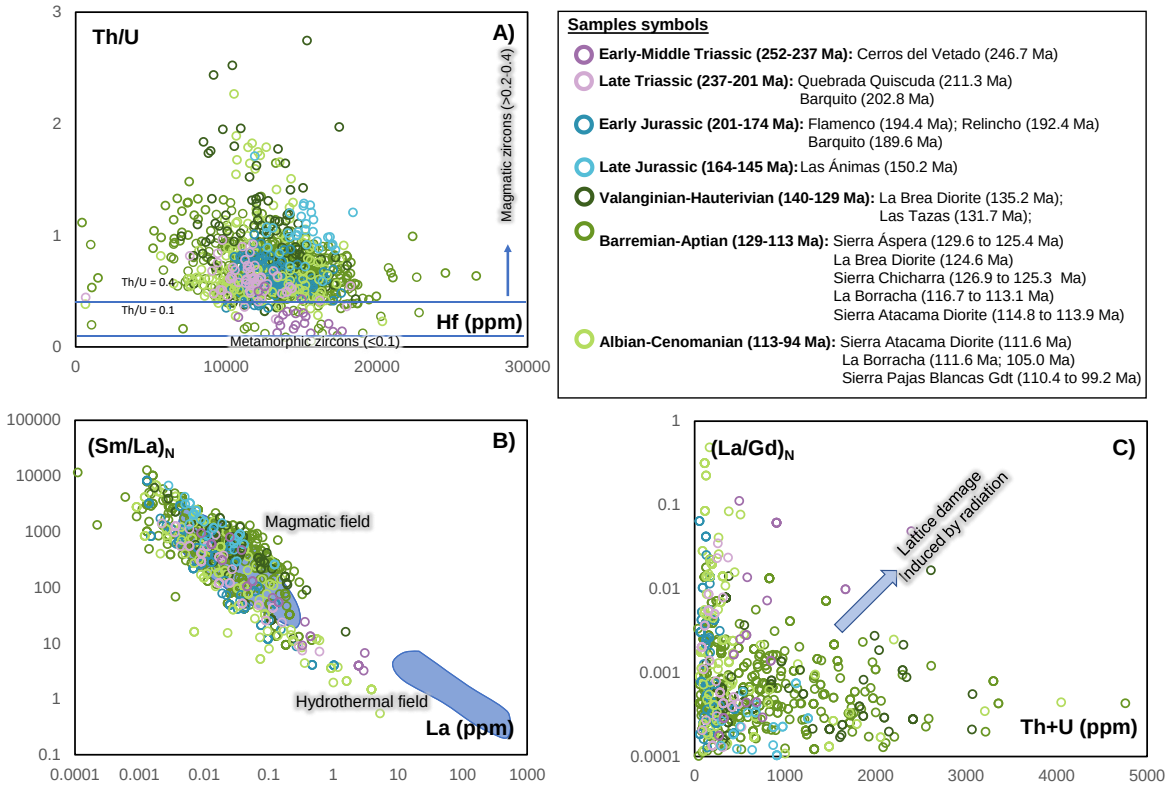

Figure 7. A) Magmatic vs metamorphic zircon discrimination diagram. The Hf vs Th/U plot suggests that most studied zircon grains have a magmatic origin. The Early to Middle Triassic grains are characterized by relatively low Th/U values (0.1-0.4) compared to those from the other samples (>0.4). The range for Th/U of magmatic (>0.2-0.4) and metamorphic (<0.1) zircon grains is from Rubatto and Gebauer (2000) and Williams and Claesson (1987). B) Magmatic vs hydrothermal zircon discrimination diagram (La vs SmN/LaN plot), suggesting that all analyzed grians are magmatic and have not been affected by post-crystallization hydrothermal alteration. Magmatic and hydrothermal fields are from Hoskin (2005). C) The Th+U vs LaN/GdN plot suggests that no metamict zircon grains are present in the studied rocks. Actinide concentration is a proxy for lattice damage induced by radiation (Whitehouse and Kamber, 2002).

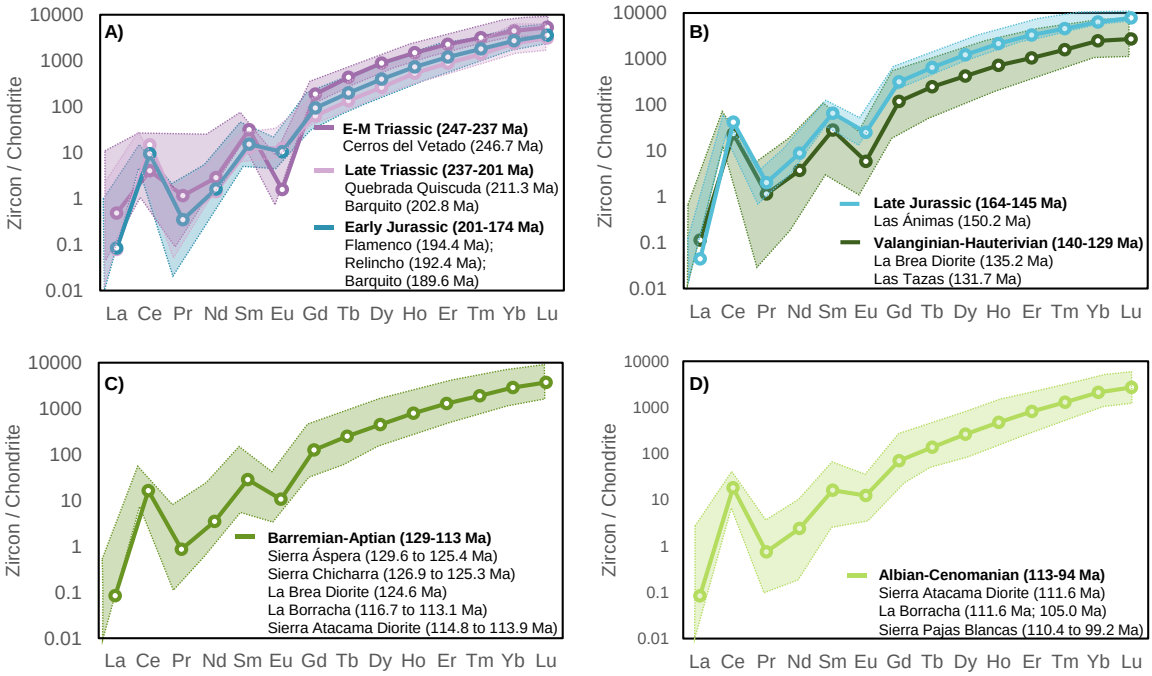

Figure 8. Zircon chondrite-normalized REE diagrams for the studied intrusive complexes. Samples are grouped by age span as in Figure 6. Normalizing values are from Sun and McDonough (1989). Shaded areas represent 5 to 95 percentile range for each sample group. Line colors refer to the median value for each group.

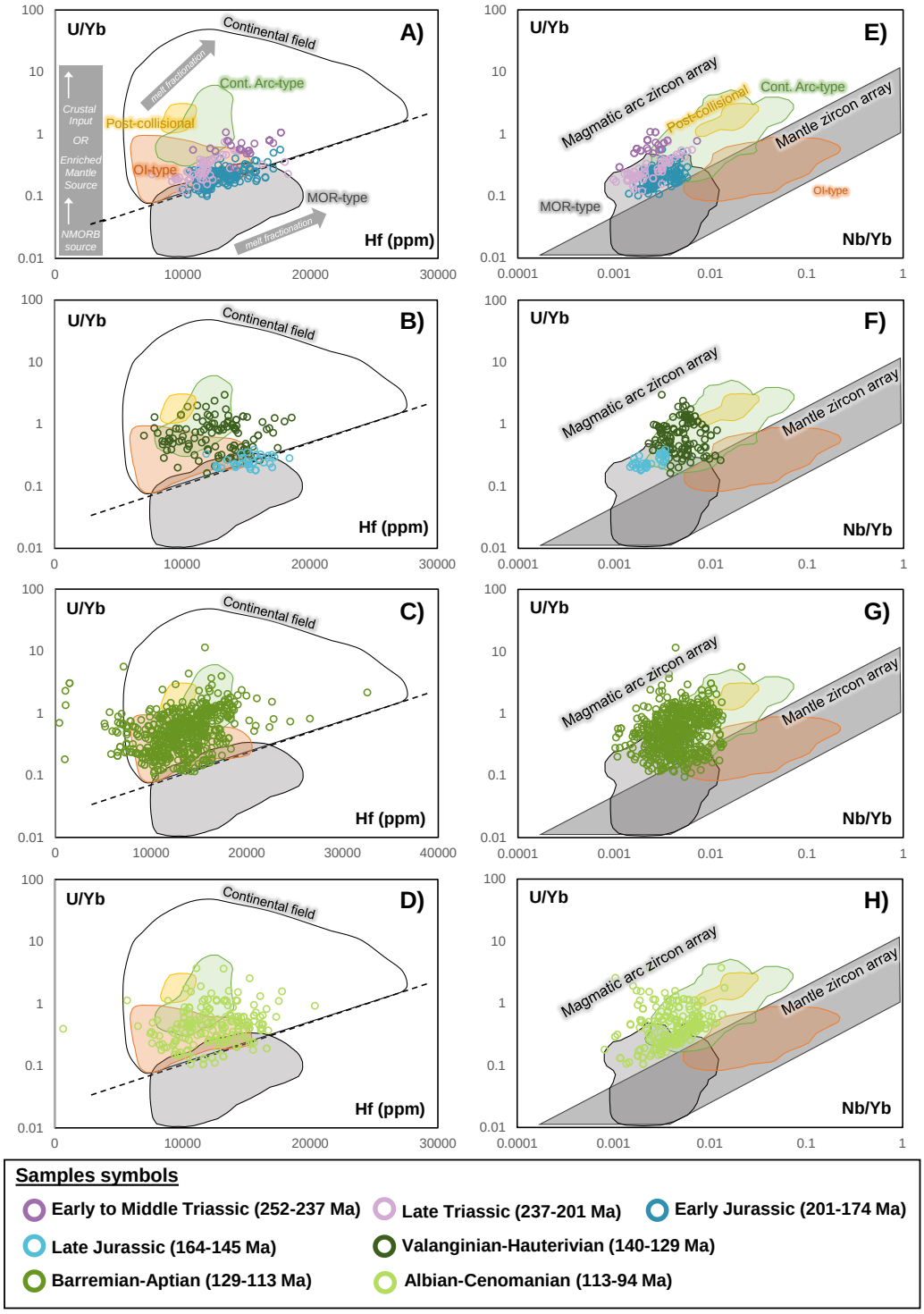

Figure 9. Zircon Hf vs U/Yb (A-D) and Nb/Yb vs U/Yb (E-H) tectonic discrimination diagrams for the studied intrusive complexes. Mid-ocean ridge (MOR-type), ocean island (OI-type), continental arc (Cont. Arc-type) and post-collisional (Post-collisional) fields are from Grimes et al. (2015), and identified by gray-, orange-, green- and yellow-shaded fields, respectively. Symbols are as in Figure 7.

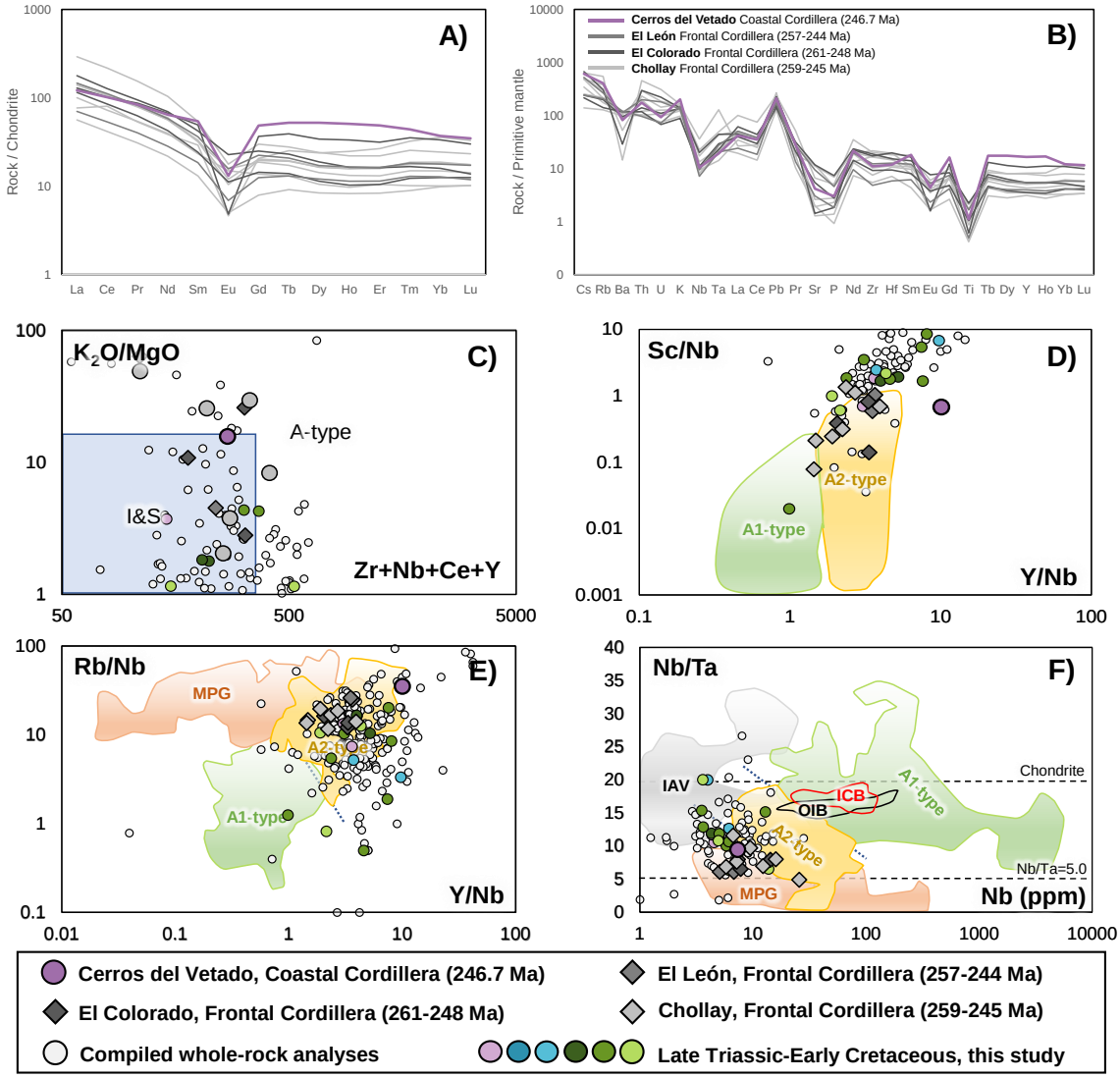

Figure 10. Whole-rock classification diagrams for Permian and Early Triassic plutonic complexes in the Frontal Andes and Coastal Cordillera. A) and B) chondrite-normalized rare earth elements and primitive mantle-normalized minor/trace elements diagrams, respectively. Normalizing values are from Sun and McDonough (1989). C) 10000*Ga/Al vs K2O plot with A-, I- and S-type granite fields (Whalen et al., 1987). D) Y/Nb vs Sc/Nb diagram for A1- and A2-type granitoids (Eby, 1992). E) Y/Nb vs Rb/Nb plot of Eby (1992), with A1-, A2- and muscovite peraluminous granites (MPG) fields from Ballouard et al. (2020). F) Nb vs Nb/Ta diagram showing the composition for MPG and A-type granitoids (Ballouard et al., 2020). Data source for El León, El Colorado and Chollay from Coloma et al. (2017) and Del Rey et al. (2019) and compiled in Table SM5. Data source for compiled whole-rock analyses from intrusive rocks of the Coastal Cordillera in Table SM4.

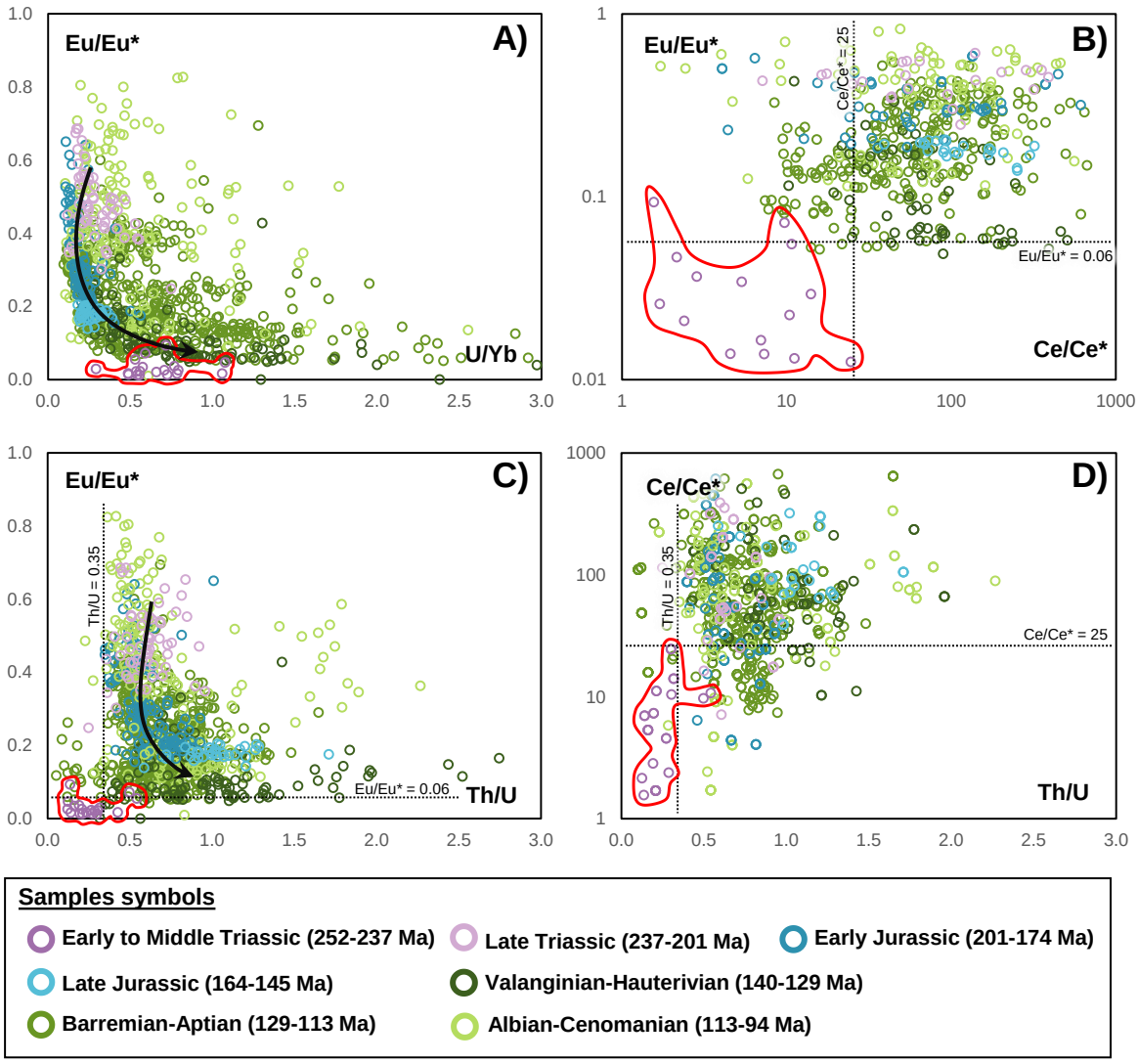

Figure 11. Zircon bivariate diagrams for the studied intrusive complexes. A) U/Yb vs Eu/Eu* and C) Th/U vs Eu/Eu*, diagrams indicating a constant decrease in the Eu anomaly from Late Triassic to lower Early Cretaceous with rather stable or slightly increasing U/Yb and Th/U ratios; B) Ce/Ce* vs Eu/Eu* and D) Th/U vs Ce/Ce*, diagrams indicating that Early to Middle Triassic zircon grains present a different composition respect to other samples in this study with strong negative Eu and weak positive Ce anomalies, possible related to variable degrees of plagioclase fractionation and redox conditions. The red outlined area represents Early to Middle Triassic zircon grains. Symbols are as in Figure 7.

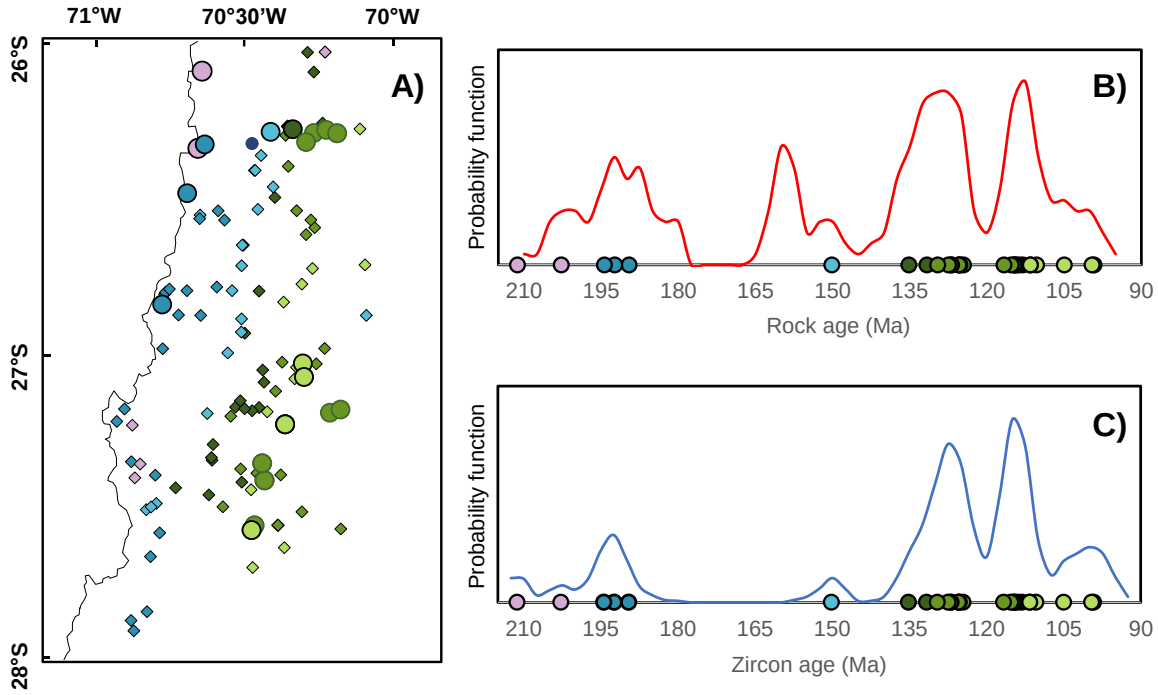

Figure 12. A) Latitude and longitude position of radiometric ages for igneous units in the area and compiled for this study. The plot shows the general temporal eastern migration of the magmatic arc. B) and C) Probability distribution functions of compiled rock ages (red line) and zircon ages obtained in this study (blue line). Probability distribution functions were calculated by kernel density estimates with a bandwidth of 2.5 Ma and a bin width of 5 Ma. Data includes amphibole, biotite and whole-rock K-Ar (n=83), $^{40}Ar/^{39}Ar$ (n=26) ages and zircon U-Pb weighted mean ages obtained in this study (n=29). Source data for the compiled radiometric ages are provided in the supplementary material (Table SM6). C) includes U-Pb ages obtained for each individual zircon (n=1163). The $^{206}Pb/^{238}U$ weighted mean age for sample groups are shown at the bottom of each plot. Symbols are as in Figure 5.

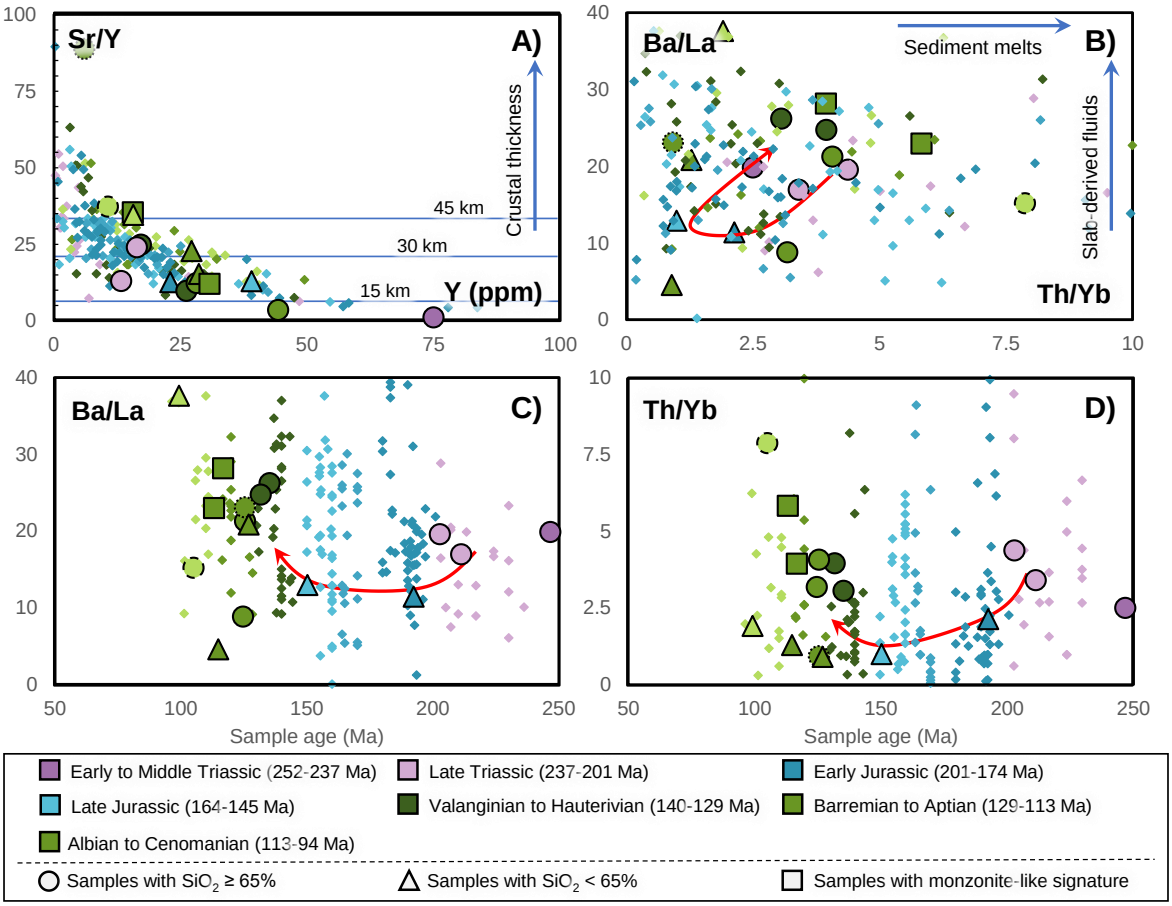

Figure 13. Whole-rock bivariate diagrams. A) Y vs Sr/Y plot showing estimated crustal thickness calculated based on Profeta et al. (2015). B) Th/Yb vs Ba/La diagram illustrating slab-derived fluids and sediment-melts contributions to the magmatic source. C) and D) Sample age vs the Ba/La and Th/Yb ratio, respectively. The compiled whole-rock analyses dataset is included. Samples from this study are identified according to their composition: circles: $SiO_2 \geq 65\%$; triangles: $SiO_2 < 65\%$; squares: monzonites.

2.11. RESEARCH HIGHLIGHTS

- First zircon U-Pb/trace element dataset from the Chilean Coastal Cordillera
- Oldest rock (ca. 247 Ma) is a transitional granitoid of the pre-Andean stage
- Onset of the Andean orogeny occurred at least 10 Ma before previous estimates (ca. 210 Ma)
- Early Andean plutonic rocks formed from a depleted source in a subduction setting
- Magmatic source enrichment occurred after tectonic change around ~150-130 Ma

2.12. ACKNOWLEDGEMENTS

Funding for this study was provided by FONDECYT grant #1190105 to F.B and M.R. Additional support was provided by the Millennium Nucleus for Metal Tracing along Subduction and FONDAP project #15090013 “Centro de Excelencia en Geotermia de Los Andes, CEGA”. José Joaquín Jara thanks ANID for providing support through a Ph.D. scholarship. The analytical work was supported by FONDEQUIP instrumentation grant EQM120098.

2.13. AUTHOR CONTRIBUTIONS

J.Joaquín Jara: Conceptualization, Methodology, Formal analysis, Investigation, Resources, Writing – Original draft, Writing – Review and editing, Visualization Fernando Barra: Conceptualization, Methodology, Validation, Investigation, Resources, Writing – Review and editing, Supervision, Project Administration Funding acquisition Martin Reich: Conceptualization, Validation, Investigation, Resources, Writing – Review and editing, Supervision, Funding acquisition Diego Morata: Methodology, Validation, Writing – Review and editing, Supervision, Funding acquisition Mathieu Leisen: Software, Validation, Formal analysis, Investigation, Resources, Writing – Review and editing Rurik Romero: Software, Validation, Formal analysis, Investigation, Resources, Writing – Review and editing.

CHAPTER 3. TRACING THE EARLY EVOLUTION OF THE ANDEAN CORILLERA BY USING ZIRCON PETROCHRONOLOGY

José Joaquín Jara[1,2,3,*], Fernando Barra[1,3], Martin Reich[1,3], Diego Morata[1,3], Mathieu Leisen[1,3], Rurik Romero[1,3]

[1]*Departamento de Geología y Centro de Excelencia en Geotermia de los Andes (CEGA), FCFM, Universidad de Chile, Plaza Ercilla 803, Santiago, Chile.*
[2]*Departamento de Ingeniería de Minería, Pontificia Universidad Católica de Chile, Av. Vicuña Mackenna 4860, Santiago, Chile.*
[3]*Millennium Nucleus for Metal Tracing Along Subduction, FCFM, Universidad de Chile, Plaza Ercilla 803, Santiago, Chile*

(*) Corresponding author: jjjara@uc.cl
Keywords: continental arc; zircon trace elements; episodic magmatism; tectonic setting; external forcing model.

3.1. ABSTRACT

Cordilleran arcs are formed by the subduction of oceanic lithosphere beneath a continental plate. This key tectonic process is responsible for the continental crust growth, recycling of materials and the formation of diverse types of magmatic-hydrothermal deposits. Here we use a multi-geochemical approach, based on zircon petrochronology and whole-rock analyses, to assess the early evolution of the Andean Cordillera. Our results show that magmatism of the early Andean Cordillera occurred over a period of ca. 120 million years (Myr) with six distinct plutonic episodes between 215 and 94 Ma. Each episode is the result of a complex interplay between mantle-crustal-slab-sediment contributions that can be traced using zircon chemistry. Overall, the magmatic composition varies as a response to changing tectonic conditions from transtensional to extensional conditions (215-145 Ma) to a transtensional regime (138-94 Ma). We conclude that an external (tectonic) forcing model with mantle-derived inputs is responsible for the episodic plutonism in this extensional continental arc.

3.2. INTRODUCTION

Orogenic systems are essential to comprehend the geological history of the Earth[1,2]. Cordilleran orogenic systems occur where oceanic lithosphere subducts under continental crust producing voluminous, episodic magmatism of mostly intermediate composition[2,3]. Traditionally, the geochemical and isotopic composition of igneous rocks coupled with field observations, have been used to determine the tectonic and compositional changes that have affected these continental magmatic arcs[4-6]. However, in some cases superimposed metamorphic and metasomatic events[7-11] obscure the primary chemical composition of plutonic and volcanic units, precluding the sole use of whole-rock geochemistry to determine their origin and evolution.

Zircon is an accessory mineral usually found in igneous, sedimentary and metamorphic rocks that is resistant to weathering and hydrothermal alteration[12]. It can be precisely dated and is able to incorporate a number of minor and trace elements; a characteristic that has been increasingly used in petrogenetic studies[13,14]. Zircon petrochronology has been applied to comprehend specific magmatic events (e.g. refs 15-17) and more extensively to study the formation and as an exploration tool for the search of magmatic-hydrothermal ore deposits (refs 18-20), i.e. "ore fertility studies", but its potential to assess the evolution of continental arcs at a regional scale has not been fully evaluated.

The early Andean Cordillera of northern Chile, also known as the Coastal Cordillera, represents the early product of the southern Andes[21], one of the most remarkable modern continental arcs of the world[2,5] (Fig. 3.1). The southern Andes comprises an orogenic belt that extends parallel to the Peru-Chile trench for more than 1,500 km and was shaped by subduction during multistage, episodic magmatism over more than 200 My. This domain has been well described in terms of its structural and geodynamic setting during the Mesozoic (e.g. refs 22-25), being key to understand the evolution of the southwestern margin of Gondwana[21-26]. Nevertheless, the chemical characteristics and petrogenesis of the Coastal Cordillera plutonic complexes have been rather understudied[27], and the complex relationship between its multiple magmatic episodes, geotectonic changes and the magma sources are poorly constrained. Here we report new U-Pb ages and trace element data from zircon grains from several plutonic complexes along the Coastal Cordillera between 26°-30°S (Fig. 3.1b) (Supplementary Data 1), covering a timespan of more than 120 Myr of geological history of the Andean orogeny. Through a multicomponent geochemical approach, based on zircon petrochronology and whole-rock analyses, the aim of our study is to determine the variable contributions of mantle-crust-slab-sediments to the magma source during the early evolution of the Andean continental arc.

3.3. THE EARLY ANDEAN CORDILLERA OF NORTHERN CHILE

The early Andean Cordillera is a non-collisional orogen built along an active margin since the Late Triassic[27]. The magmatic arc progressively migrated eastward and was intrinsically associated with back/intra-arc basins[21-26] in a multistage, extensional to transtensional setting[23,24]. This continental arc developed over a Paleozoic to early Mesozoic basement and was epitomized by thick basaltic to andesitic Middle Jurassic volcanic units with minor sedimentary sequences, and by north-south oriented, elongated plutonic complexes[28]. The volcanic rocks have tholeiitic affinity at the bottom and calc-alkaline at the top, and are characterized by primitive Sr, Nd and Pb isotopic compositions[28-31]. However, they are enriched in LILE, probably because of variable sediment contributions[30,32]. These sequences were intruded by calc-alkaline plutonic complexes distributed in belts parallel to the trench with eastward-younging ages[27,33,34] (Fig. 3.1b). Back/intra-arc basaltic to andesitic lavas interbedded with marine units of Late Jurassic to Early Cretaceous ages overlaid the Middle Jurassic volcanic rocks at its eastern edge[21,28]. On top and to the east, carbonate sedimentary sequences were deposited[21]. During the upper Early Cretaceous an extensional event led to subsidence and the development of aborted marginal basins[35]. Volcanic and sedimentary rocks unconformably overlying back-arc/intra-arc units are representative of this event[21]. At the end of the Early Cretaceous, and

concurrent with the final breakup of Gondwana and the opening of the Atlantic Ocean, this tectonic extensional setting changed to a compressional regime[26], which led to the inversion and closure of back/intra-arc basins and forced the migration of the magmatic arc to the east[26,35].

The main structural feature of the Coastal Cordillera is the Atacama Fault System (AFS), which extends from north to south for more than 1,000 km and was active intermittently at least since Middle to Late Jurassic (Fig. 3.1b) (ref. 19). It consists of vertical ductile shear zones and brittle fault arrangements in concave segments with north-northwest, north and north-northeast faults with normal and sinistral components[22-25,34].

3.4. EPISODIC, CALC-ALKALINE PLUTONISM IN THE EARLY ANDEAN CORDILLERA IN NORTHERN CHILE

In the past decades, an increasing number of studies have recognized the episodic nature of magmatic arcs[3,36]. However, few cases of this phenomenon have been reported for arcs developed in extensional to transtensional settings[36]. The available geochronological data from intrusive units in the study area (Supplementary Data 2) supports the notion that these rocks were generated by several magmatic pulses during the eastward migration of the arc (Fig. 3.2a,b) (refs 21,26). Previous studies25,27,33,34,37 identified three to five main plutonic events between 200-95 Ma, with a remarkable lull between 180 and 165 Ma and a significant flare-up from 140 to 120 Ma. These events are further recorded by zircon petrochronology (this study; ref. 27), which shows younging crystallization ages to the east (Figs. 3.1b, 3.2a) and clearly define six episodes of plutonic emplacement at ca. 215-203, 200-185, 160-145, 138-121, 120-108 and 103-94 Ma (Fig. 3.2c); the first one not reported before. The differences between outcrop and zircon ages (Fig. 3.2b,c) could be explained by: i) the higher number of igneous units and samples included in the outcrop series, which allows to better identify minor events and assess the age amplitude of major ones (sampling bias[36]); and ii) the inclusion of crystallization and cooling ages (K-Ar and $^{40}Ar/^{39}Ar$ data) in the outcrop series, making it less prompt to precisely define the starting and ending of plutonic episodes. Cooling ages apparently have a minor effect due to rapid cooling of plutonic units in the early Andean continental arc[27,34,37].

The plutonic complexes of the early Andean Cordillera are mainly composed of amphibole and biotite gabbro diorites to granodiorites[28,31] (Supplementary Data 3), with scarce granites but during the inception of the magmatic arc37 (Fig. 3.2d). They are predominantly metaluminous to slightly peraluminous with calc-alkaline affinities (Fig. 3.2e-g). All these rocks are enriched in LILE and show variable fractionation of REE. Lower Nb, Ta, P and Ti contents are also noticeable, as well as positive Pb-anomalies[27,30,31]. These results, coupled to published isotopic data[29,31,37], suggest that they were generated from a rather juvenile and depleted mantle source in a subduction setting. Nevertheless, each plutonic episode presents particular geochemical features that can be used to trace the evolution of the arc[36].

3.5. ZIRCON AND WHOLE-ROCK PETROGENETIC INDICATORS

To better constrain the episodic magmatism and trace the geological evolution of the early Andean continental arc, we selected 10 petrogenetic indicators based on whole-rock and zircon chemistry (Fig. 3.3). First order parameters were determined by: (i) whole-rock LaN/YbN (and Sr/Y; Supplementary Figure 1) ratios, used to estimate crustal thickness or depth to Moho (refs 38,39); (ii) zircon Th/U ratios, to recognize extensional and compressional periods in subduction environments (ref. 40); and (iii) Ti-in-zircon temperatures, which could be linked to magma composition, depth of emplacement and cooling rates in magma chambers[41,42]. In addition, the magma source of the rocks was determined by whole-rock La/Sm, Ba/La and Nb/Zr (ref. 4) and zircon U/Yb (ref. 13) elemental ratios. Finally, trends in magma's oxygen fugacity are: (i) recorded by zircon Eu-anomalies and Ce/Nd ratios; and (ii) calculated using rock-to-zircon elemental partitioning coefficients[43,44]. To identify trends and/or anomalous values, median and percentiles 5% and 95% were calculated using a kernel density estimation process with a bandwidth of 2.5 Ma and a bin width of 5 Ma for each series, except for calculated oxygen fugacity due to restricted number of samples with zircon and whole-rock analyses (n=30).

3.6. MULTISTAGE EVOLUTION OF THE EARLY ANDEAN CORDILLERA

The formation of the early Andean Cordillera commenced in the Late Triassic, when subduction restarted along the southwestern margin of Gondwana after an anorogenic period[21,27]. The magmatic arc was established in the current Coastal Cordillera in a rather attenuated crust (La_N/Yb_N ~6; ref. 31) within multistage, extensional to transtensional tectonic settings[23,24].

The first and second plutonic events of the early Andean continental arc took place between 215-203 and 200-185 Ma (LT and EJ; Figs. 3.2c and 3.3). These are characterized by gradual and continuous thinning of the crust from ~30 to ~22 km (La_N/Yb_N from ~4.0 to ~3.0, Fig. 3.3a; Sr/Y from ~24 to ~12, Supplementary Figure 1) and a depletion of the magmatic source. Zircon grains show low Th/U ratios of ~0.60 with minor dispersion (Fig. 3.3f), a behavior usually linked to compressional settings40. Ti-in-zircon temperatures vary within a restricted range from ~750 to near 800°C (Fig. 3.3g). Minor sediment contributions and crustal contamination are recorded by La/Sm ratio (2.6–3.8; Fig. 3.3b) and fluid-derived elements from the slab dehydration are negligible (Ba/La<20; Fig. 3.3c). This led to an increasingly depleted source with a N-MORB signature that is reflected in the Nb/Zr (0.079-0.039; Fig. 3.3d) and zircon U/Yb (0.41 to 0.24; Fig. 3.3h) ratios. The redox state of the magmas was relatively low due to the reducing effect of slab fluids. Oxygen fugacity markers decrease from intermediate initial values (ΔFMQ from −1.37 to −2.41; zircon Eu_N/Eu^*=0.36–0.26; zircon Ce/Nd=7.2–6.9; Figs. 3.3e,i,j). These geochemical signatures suggest that plutonic emplacement took place in an attenuated margin[21,26] during a transtensional regime with an increasing subduction angle and plate decoupling[23], which led to a gradual but consistent thinning of the continental crust (Fig. 3.4a). These results are consistent with structural observations in the forearc[23], and an isotopic pull-up of its igneous units[29,31] that is uncommon in continental arcs[45]. This period ended with foundering of the slab, subduction rollback and a complete decoupling between plates in an arc-normal extensional process during the extensive La Negra volcanic event (~180 to ~160 Ma) (refs. [23,26]).

The third episode (160-145 Ma; LJ; Fig. 3.2c and 3.3), is concurrent and/or subsequent La Negra volcanic event (NVE, Fig. 3.3) and prior to a plutonic hiatus in the Jurassic to Cretaceous transition. During this period, a crustal thickness of ~20 km is estimated based on whole-rock chemistry (La_N/Yb_N=2.4–6.6, Fig. 3.3a; Sr/Y=11–23, Supplementary Figure 1) and the highest zircon Th/U ratio among the studied samples (0.89; Fig. 3.3f). High crystallization temperatures are also observed (~800 to ~950°C; Fig. 3.3g). Accordingly, Late Jurassic magmatism would have been generated primarily by decompressional melting of the upper mantle[28,46] with minor contributions from the subduction process (La/Sm=3.1 and Ba/La=19 ratios; Fig. 3.3b,c). This was reflected in a highly depleted and reduced signature of the intrusive units, with whole-rock Nb/Zr values consistently below 0.039 and near the N-MORB value (Fig. 3d), a ΔFMQ of −2.05 (Fig. 3.3e), and zircon Eu_N/Eu^* and Ce/Nd ratios with median values of 0.11 and 3.8, respectively (Fig. 3.3i,j). Nevertheless, a relatively high zircon U/Yb ratio (0.60) was obtained due to the influence of two highly differentiated samples, rather uncommon in this geologic period (samples JJJD_43 and JJJD_62). Excluding these samples, a U/Yb ratio of 0.27 was obtained, similar to that of the Early Jurassic episode (Fig. 3.3h). These results are consistent with: i) a strong arc-normal extensional setting and shallow plutonic emplacement, which is based on structural analyses of the AFS and its relationship with surrounding plutonic bodies (refs 23,24,34); and ii) a negative to neutral, trench normal absolute and relative convergence rates in the kinematic plate model of South America reported by Maloney and coauthors[47]. Overall, during the long-lasting, transtensional to extensional process that occurred between the Late Triassic and Late Jurassic, the contribution of sediments and slab-derived fluids was strongly diminished, lithospheric mantle lessened, decompressional melting triggered and asthenospheric material upwelled to the base of the crust (Fig. 3.4c). This led to a progressively depleted, dehydrated and reduced magmatism[27-30,46].

The fourth and fifth plutonic events occurred between 138-121 and 120-108 Ma, respectively (V-EAp and LAp-EAlb; Figs. 3.2c and 3.3). These episodes are characterized by increasing crustal thickness (La_N/Yb_N=6.7, Fig. 3a; Sr/Y~15, Supplementary Figure 1), slightly lower crystallization temperatures (~780°C vs ~900°C; Fig. 3.3g) and higher fluid and sediment contributions to the mantle wedge compared to the previous period (La/Sm=3.7 vs 3.1 and Ba/La=24 vs 19; Fig. 3.3b,c). As a result, more enriched (zircon U/Yb = 0.79; Fig. 3.3h), hydrated and oxidized (zircon Eu_N/Eu^* = 0.19; Ce/Nd = 6.0; Fig. 3.3i,j) magmas were identified from the zircon geochemistry. These trends could be explained by: i) the transition from an arc-normal extensional to a (low-stress?) transtensional regime (Fig. 3.4d), a change that has been recorded in the kinematics of the AFS (refs 23-25,34); and ii) an increasing coupling between plates, probably due to higher convergence rates (Fig. 3.4e) (refs 23,47). As a result, subduction contributions (sediments and fluids) progressively increased and the magmas were more enriched, hydrated and oxidized than in previous episodes.

Finally, the last plutonic episode of the early Andean Cordillera occurred during the late Albian to Cenomanian (103-94 Ma; LAlb-Cnm episode, Fig. 3.3) after a magmatic lull in the middle Albian (108-103 Ma; Fig. 3.2b,c). A crustal thickness of >35 km (La_N/Yb_N=6.2, Fig. 3.3a; Sr/Y=27, Supplementary Figure 1), increasing slab-derived fluids with minor sediment contributions (La/Sm=4.5 vs 3.7; Ba/La=37 vs <25; Fig. 3.3b,c) and a

depleted mantle source (Nb/Zr=0.041; zircon U/Yb=0.31; Fig. 3.3c,g), could be better explained by an extensional to transtensional regime with high convergence rates and relative decoupling between plates (Fig. 3.4f). This setting is also supported by the relatively high oxygen fugacity markers recorded in this period (ΔFMQ= -1.54; zircon Eu_N/Eu^*=0.52 vs 0.19 and Ce/Nd=11 vs 6.0; Fig. 3.3e,i,j). These results are in agreement with the geological record in the back-arc[35], and with the changes in trench normal and parallel relative convergence rates of the kinematic plate model in Maloney and coauthors[47].

3.7. TECTONICALLY-DRIVEN EPISODIC MAGMATISM IN A CONTIENTAL ARC

The evidence presented in this study, coupled with current knowledge of the tectonic and structural evolution of Gondwana's southwestern margin, allows us to conclude that the episodic magmatism of the early Andean Cordillera resulted from a multistage, transtensional to extensional subduction setting[21,23,28]. Six plutonic episodes were identified between Late Triassic and earliest Late Cretaceous (215-94 Ma), each one related to particular substages in the evolution of the continental arc. These episodes are better identified and characterized based on zircon petrochronology coupled with whole-rock geochemical analyses (Figs. 3.2 and 3.3), and can be associated with significant tectonic changes in the continental margin (Fig. 3.4). Therefore, an "external forcing" model[36] with mantle-derived inputs[48] is argued for the episodic plutonism in this extensional continental arc. This finding contrast with evidence reported for other arcs in compressional to transpressional settings, in which "internal feedback"[36], such as foreland underthrusting[3] or arc migration[49], are the preferred explanation for cyclical magmatism.

3.8. METHODS

Descriptions of the studied plutonic complexes and analyzed samples are in presented in Supplementary Table 1 and Supplementary Table 2, respectively. Methods for whole-rock analysis and for simultaneous zircon U-Pb geochronology and trace element determinations are reported in Supplementary material. Whole-rock and zircon raw datasets of this study and those of Jara et al. (Chapter 2) are shown in Supplementary Data 1. Compiled published radiometric ages for plutonic units in the study area are in Supplementary Data 2. Compiled published whole-rock analyses for intrusive rocks in the early Andean Cordillera are in Supplementary Data 3.

3.9. ACKNOWLEDGEMENTS

Funding for this study was provided by FONDECYT grant #1190105 to F.B and M.R. Additional support was provided by ANID through Millennium Science Initiative Program (NCN13_065) and FONDAP project #15090013 "Centro de Excelencia en Geotermia de Los Andes, CEGA". JJJ thanks ANID for providing support through a Ph.D. scholarship. The analytical work was supported by FONDEQUIP instrumentation grant EQM120098. We also thank José Cembrano for his constructive comments that helped improved the clarity and quality of this contribution.

3.10. AUTHORS CONTRIBUTIONS

J.Joaquín Jara: Conceptualization, Methodology, Formal analysis, Investigation, Resources, Writing – Original draft, Writing – Review and editing, Visualization. Fernando Barra: Conceptualization, Methodology, Validation, Investigation, Resources, Writing – Review and editing, Supervision, Project Administration Funding acquisition. Martin Reich: Validation, Investigation, Resources, Writing – Review and editing, Supervision, Funding acquisition. Diego Morata: Methodology, Validation, Writing – Review and editing, Supervision, Funding acquisition. Mathieu Leisen: Software, Validation, Formal analysis, Investigation, Resources, Writing – Review and editing Rurik Romero: Software, Validation, Formal analysis, Investigation, Resources, Writing – Review and editing.

3.11. COMPETING INTERESTS

The authors declare that they have no known competing financial interests or personal relationships that could have appeared to influence the work reported in this paper.

3.12. BIBLIOGRAPHY

1. Scholl, D. W. & von Huene, R. 2007. Crustal recycling at modern subduction zones applied to the past: Issues of growth and preservation of continental basement crust, mantle geochemistry, and supercontinent reconstruction. Geological Society of America Memoirs **200**, 9-32 (2007).
2. Ducea, M.N., Saleeby, J.B. & Bergantz, G. The architecture, chemistry and evolution of continental magmatic arcs. Annual Review of Earth and Planetary Science **43**, 10.1-10.33 (2015).
3. DeCelles, P. G., Ducea, M.N., Kapp, K. & Zandt, G. Cyclicity in Cordilleran orogenic systems. Nature Geoscience **2**, 251-257 (2009).
4. Pearce, J.A. & Peate, D.W. Tectonic implications of the composition of volcanic arc magmas. Annual Review of Earth and Planetary Science **23**, 251-285 (1995).
5. Haschke, M. et al., in *The Andes: Active Subduction Orogeny* (eds Oncken, O. et al.) 337-353 (Springer, 2006).
6. Kemp, A.I.S. & Hawkesworth, C.J. in *Treatise of Geochemistry* (eds Holland, H. & Turekian, K.) 379-421 (Elsevier, 2014).
7. Barton, M.D. & Hanson, R.B. Magmatism and the development of low-pressure metamorphic belts: Implications from the western United States and thermal modeling. GSA Bulletin **101**, 1051-1065 (1989).
8. Battles, D. A. & Barton, M. D. Arc-related sodic hydrothermal alteration in the western U. S. Geology **23**, 913-916 (1995).
9. Lucassen, F. & Franz, G. Magmatic arc metamorphism: Petrology and temperature history of metabasic rocks in the Coastal Cordillera of northern Chile. Journal of Metamorphic Geology **14**, 249-265 (1996).
10. Sorensen, S.S. et al. From Jurassic shores to Cretaceous plutons: Geochemical evidence for paleoalteration environments of metavolcanic rocks, eastern California. GSA Bulletin **110**, 326-343 (1998).

11. Rossel, P., Oliveros, V., Ducea, M. & Hernandez, L. Across and along arc geochemical variations in altered volcanic rocks: Evidence from mineral chemistry of Jurassic lavas in northern Chile, and tectonic implications. Lithos **239**, 97-113 (2015).
12. Finch, R.J. & Hanchar, J.M. Structure and chemistry of zircon and zircon group minerals. Reviews in Mineralogy and Geochemistry **53**, 1-25 (2003).
13. Grimes, C.B., Wooden, J.L., Cheadle, M.J. & John, B.E. "Fingerprinting" tectono-magmatic provenance using trace elements in igneous zircon. Contributions in Mineralogy and Petrology **170**, 1-26 (2015).
14. Balica, C. et al. A zircon petrochronologic view on granitoids and continental evolution. Earth and Planetary Science Letters **531**, [116005] (2020).
15. Claiborne, L.L, Miller, C.F., Flanagan, D.M., Clynne, M.A. & Wooden, J.L. Zircon reveals protracted magma storage and recycling beneath Mount St. Helens. Geology **38**, 1011-1014 (2010).
16. Carley, T.L. et al. Iceland is not a magmatic analog for the Hadean: Evidence from the zircon record. Earth and Planetary Science Letters **405**, 85-97 (2014).
17. Xu, Z., Zheng, Y. & Zhao, Z. Zircon evidence for incorporation of terrigenous sediments into the magma source of continental basalts. Scientific Reports **8**, [178] (2018).
18. Buret, Y. et al. From a long-lived upper-crustal magma chamber to rapid porphyry copper emplacement: reading the geochemistry of zircon crystals at Bajo de la Alumbrera (NW Argentina). Earth and Planetary Science Letters **450**, 120-131 (2016).
19. Gardiner, N.J. et al. Contrasting granite metallogeny through the zircon record: A case study from Myanmar. Scientific Reports **7**, [748] (2017).
20. Pizarro, H. et al. Porphyry indicator zircons (PIZs): Application to exploration of porphyry copper deposits. Ore Geology Reviews **126**, [103771] (2020).
21. Charrier, R., Pinto, L. & Rodríguez, M.P. in *The Geology of Chile* (eds Moreno, T. & Gibbons, W.) 21-114 (The Geological Society of London, 2007).
22. Scheuber, E. & Andriessen, P.A.M. The kinematic and geodynamic significance of the Atacama fault zone, northern Chile. Journal of Structural Geology **12**, 24-257 (1990).
23. Scheuber, E. & González, G. Tectonics of the Jurassic-Early Cretaceous magmatic arc of the north Chilean Coastal Cordillera (22°-26°S): A story of crustal deformation along a convergent plate boundary. Tectonics **18**, 895-910 (1999).
24. Grocott, J. & Taylor, G.K. Magmatic arc fault systems, deformation partitioning and emplacement of granitic complexes in the Coastal Cordillera, northern Chilean Andes (25°30'S to 27°00'S). Journal of the Geological Society of London **159**, 425-442 (2002).
25. Seymour, N.M. et al. The relationship between magmatism and deformation along the intra-arc strike-slip Atacama fault system, northern Chile. Tectonics **39**, [e2019TC005702] (2020).
26. Mpodozis, C. & Ramos V.A. in *Geology of the Andes and its Relation to Hydrocarbon and Mineral Resources* (eds Ericksen, G.E., Cañas-Pinochet, M.T. & Reinemud, J.A.) 59-90 (Circumpacific Council for Energy and Mineral Resources, 1989).

27. Jara, J.J. et al. Geochronology and petrogenesis of intrusive rocks in the Coastal Cordillera of the Atacama Region, northern Chile: whole rock geochemistry and zircon U-Pb dating/trace elements analysis (Chapter 2).
28. Parada, M. A. et al. in *The Geology of Chile* (eds Moreno, T. & Gibbons, W.) 115-146 (The Geological Society of London, 2007).
29. Lucassen, F. et al. Nd, Pb and Sr isotope composition of juvenile magmatism in the Mesozoic large magmatic province of northern Chile (18°-27°S): Indications for a uniform subarc mantle. Contributions in Mineralogy and Petrology **152**, 571-589 (2006).
30. Oliveros, V., Morata, D., Aguirre, L., Féraud, G. & Fornari, M. Jurassic to Early Cretaceous subduction-related magmatism in the Coastal Cordillera of northern Chile (18°30'-24°S): Geochemistry and petrogenesis. Revista Geológica de Chile **34**, 209-232 (2007).
31. Oliveros, V. et al. Lithospheric evolution of the Pre- and Early Andean convergent margin, Chile. Gondwana Research **80**, 202-227 (2020).
32. Rossel, P. et al. The Early Andean subduction system as an analogue to island arcs: evidence from across-arc geochemical variations in northern Chile. Lithos **179**, 211-230 (2013).
33. Berg, K. & Baumann, A. Plutonic and metasedimentary rocks from the Coastal Range of northern Chile: Rb-Sr and U-Pb systematic. Earth and Planetary Science Letters **75**, 101-115 (1985).
34. Dallmeyer, R.D., Brown, M., Grocott, J., Taylor, G. & Treloar, P. Mesozoic magmatic and tectonic events within the Andean plate boundary zone, north Chile: Constraints from 40Ar/39Ar minerals ages. Journal of Geology **104**, 19-40 (1996).
35. Mpodozis, C. & Allmendinger, R. Extensional tectonics, Cretaceous Andes, northern Chile (27°S). GSA Bulletin **105**, 1462-1477 (1993).
36. Paterson, S.R. & Ducea, M.N. Arc magmatic tempos: Gathering the evidence. Elements **11**, 91-98 (2015).
37. Girardi, J.D. Comparison of Mesozoic magmatic evolution and iron oxide (-copper-gold) ('IOCG') mineralization, Central Andes and Western North America. Ph.D. Thesis (Unpublished). The University of Arizona (Tucson, 2014).
38. Profeta, L. et al. Quantifying crustal thickness over time in magmatic arcs. Scientific Reports **5**, [17786] (2015).
39. Lieu, W.K. & Stern. R.J. The robustness of Sr/Y and La/Yb as proxies for crust thickness in modern arcs. Geosphere **15**, 621-641 (2019).
40. McKay, M. P., Jackson, W.T., Jr. & Hessler, A. Tectonic stress regime recorded by zircon Th/U. Gondwana Research **57**, 1-9 (2018).
41. Ferry, J.M. & Watson, E.B. New thermodynamic models and revised calibrations for the Ti-in-zircon and Zr-in-rutile thermometers. Contributions in Mineralogy and Petrology **154**, 429-437 (2007).
42. Schiller, D. & Fritz, F. Application of Ti-in-zircon thermometry to granite studies: problems and possible solutions. Contributions in Mineralogy and Petrology **174**, [51] (2019).
43. Smythe, D.J. & Brenan, J.M. Magmatic oxygen fugacity estimated using zircon-melt partitioning of cerium. Earth and Planetary Science Letters **453**, 260-266 (2016).
44. Loucks, R.R., Fiorentini, M.L. & Henríquez, G.J. New magmatic oxybarometer using trace elements in zircon. Journal of Petrology **61**, [egaa034] (2020).

45. Chapman, J.B., Ducea, M.N., Kapp, P., Gehrels, G.E. & DeCelles, P.G. Spatial and temporal radiogenic isotopic trends of magmatism in Cordilleran orogens. Gondwana Research **48**, 189-204 (2017).
46. Pichowiak, S. in *Tectonics of the Southern Central Andes* (eds Reutter, K.J., Scheuber, E. & Wigger, P.) 203-217 (Springer, 1994).
47. Maloney, K.T., Clarke, G.L., Klepeis, K.A. & Quevedo, L. The Late Jurassic to present evolution of the Andean margin: Drivers and the geological record. Tectonics **32**, 1-17 (2013).
48. Martínez Ardila, A.M., Paterson, S.R., Memeti, V., Parada, M.A. & Molina, P.G. Mantle driven Cretaceous flare-ups in Cordilleran arcs. Lithos **326-327**, 19-27 (2019).
49. Chapman, J.B. & Ducea, M.N. The role of arc migration in Cordilleran orogenic cyclicity. Geology **47**, 627-631 (2019).

3.13. FIGURES

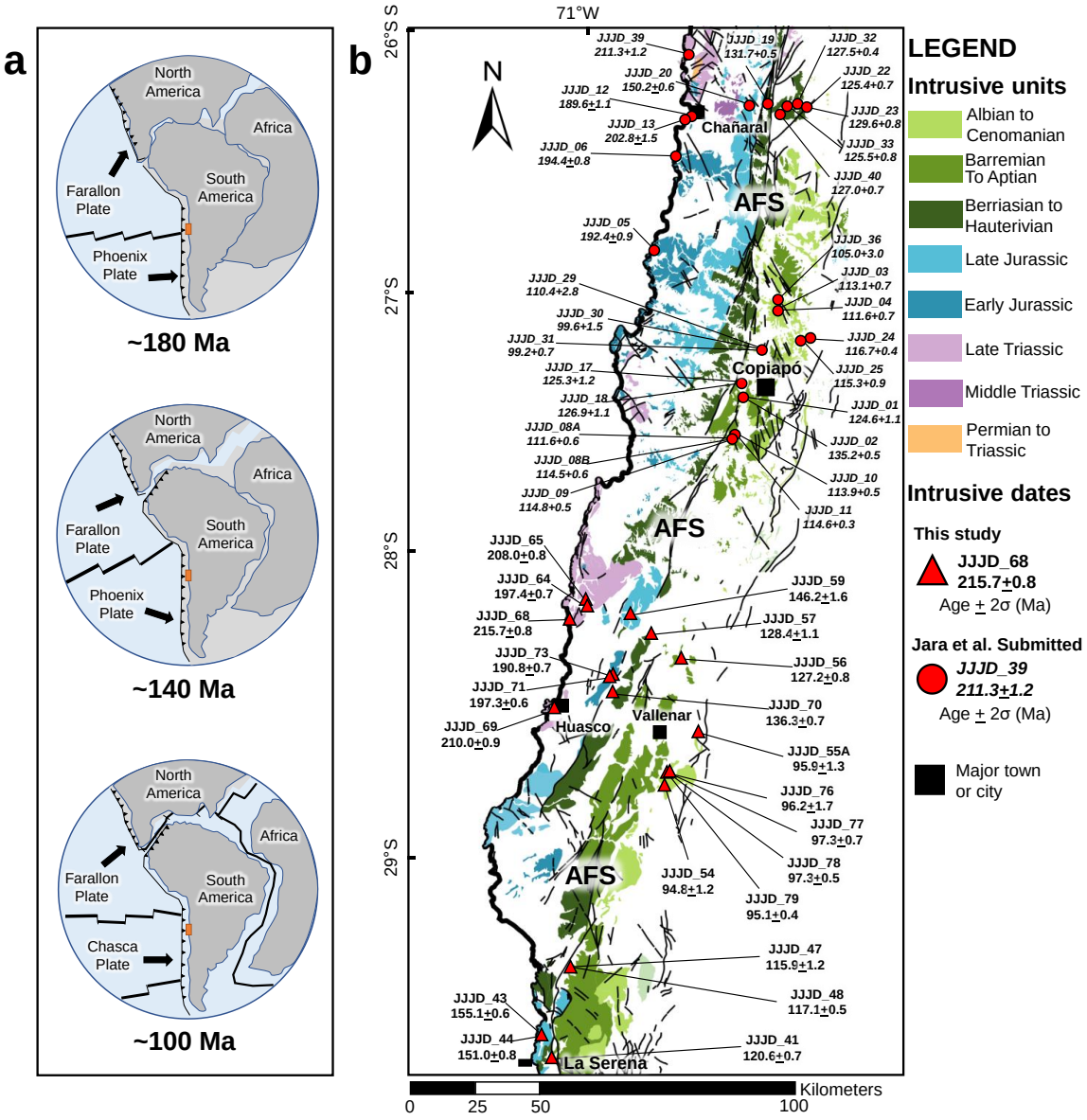

Figure 3.1. **Plutonic complexes of the early Andean Cordillera of northern Chile. a**, geotectonic setting of Gondwana's southwestern margin during the early Andean tectonic cycle (~200-100 Ma). **b**, distribution of plutonic complexes in the study area. Samples and their U-Pb zircon ages are indicated, including datasets in Supplementary Data 1. **AFS**, Atacama Fault System.

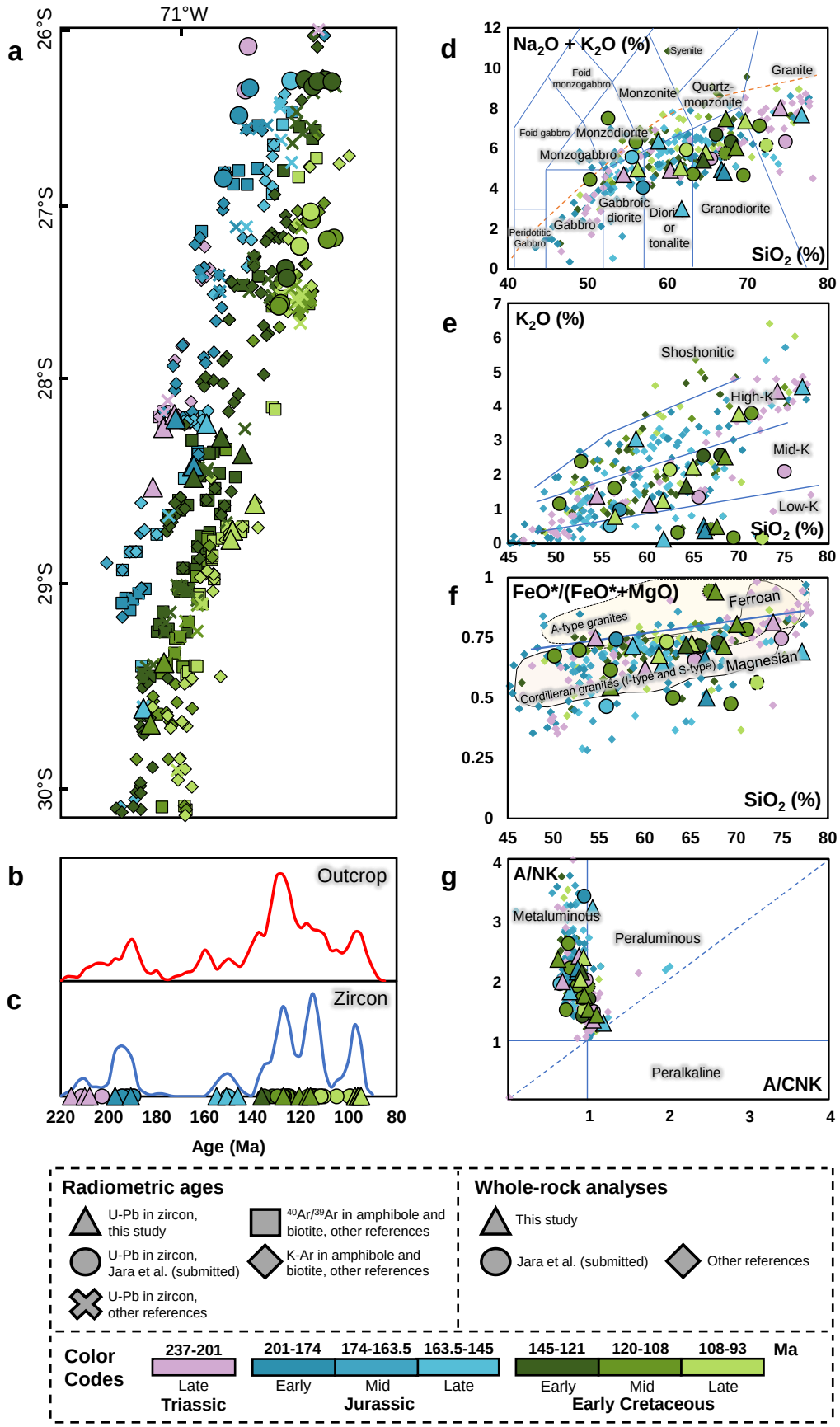
a
71°W
26°S
27°S
28°S
29°S
30°S
b
Outcrop
c
Zircon
220 200 180 160 140 120 100 80
Age (Ma)
d
Na2O + K2O (%)
Syenite
Foid monzogabbro
Granite
Monzonite
Quartz-monzonite
Foid gabbro
Monzodiorite
Monzogabbro
Gabbroic diorite
Diorite or tonalite
Granodiorite
Gabbro
Peridotitic Gabbro
SiO2 (%)
e
K2O (%)
Shoshonitic
High-K
Mid-K
Low-K
SiO2 (%)
f
FeO*/(FeO*+MgO)
Ferroan
A-type granites
Magnesian
Cordilleran granites (I-type and S-type)
SiO2 (%)
g
A/NK
Metaluminous
Peraluminous
Peralkaline
A/CNK
Radiometric ages
U-Pb in zircon, this study
U-Pb in zircon, Jara et al. (submitted)
U-Pb in zircon, other references
40Ar/39Ar in amphibole and biotite, other references
K-Ar in amphibole and biotite, other references
Whole-rock analyses
This study
Jara et al. (submitted)
Other references
Color Codes
237-201
Late
Triassic
201-174
Early
174-163.5
Mid
163.5-145
Late
Jurassic
145-121
Early
120-108
Mid
108-93
Late
Early Cretaceous
Ma

Figure 3.2. Radiometric ages and whole-rock geochemistry of plutonic complexes of the early Andean Cordillera. a, outcrop ages of plutonic complexes in the study area. b, probability distribution function of outcrop ages in the study area. **a,b** include the datasets in Supplementary Data 1 and 2. **c**, probability distribution function of zircon $^{238}U/^{206}Pb$ ages in the study area, including data from Supplementary Data 1. **b,c** were calculated using a kernel density estimation process with a bandwidth of 2.5 Ma and a bin width of 5 Ma. **d**, total alkali versus silica classification plot (Middlemost, 1994), including the alkaline and sub-alkaline limit from Irvine and Baragar (1971). **e**, SiO_2 vs K_2O diagram of Peccerillo and Taylor (1976), showing shoshonitic and high-, mid- and low-K fields. **f**, SiO_2 vs FeO*/(FeO*+MgO) plot of Frost et al. (2001), defining the ferroan and magnesian fields. **g**, molar A/CNK versus molar A/NK plot, showing the metaluminous peraluminous and peralkaline fields. **d-g** include the datasets in Supplementary Data 1 and 3. **a-g**, symbol colors refer to the age of the plutonic complexes.

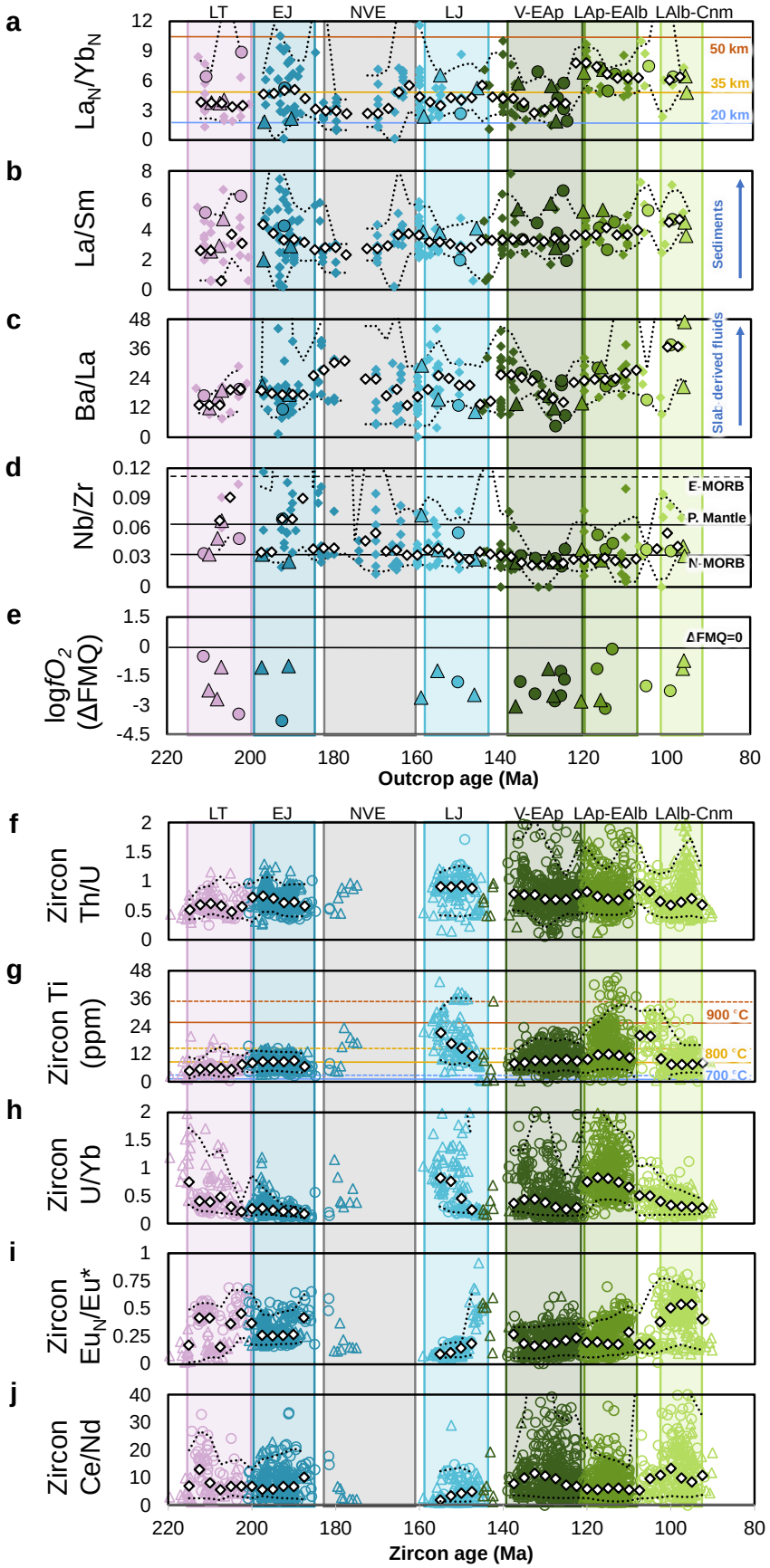
a
b
c
d
e
f
g
h
i
j
LT
EJ
NVE
LJ
V-EAp
LAp-EAlb
LAlb-Cnm
La$_N$/Yb$_N$
50 km
35 km
20 km
La/Sm
Sediments
Ba/La
Slab derived fluids
Nb/Zr
E-MORB
P. Mantle
N-MORB
logfO_2 (ΔFMQ)
ΔFMQ=0
Outcrop age (Ma)
Zircon Th/U
Zircon Ti (ppm)
900 °C
800 °C
700 °C
Zircon U/Yb
Zircon Eu$_N$/Eu*
Zircon Ce/Nd
Zircon age (Ma)

Figure 3.3. Zircon and whole-rock petrogenetic indicators to trace the evolution of the early Andean Cordillera. a, La_N/Yb_N, to estimate crustal thickness (ref. 32). **b-c**, La/Sm and Ba/La, proxies for sediments and slab-derived fluids contribution to magma genesis. **d**, Nb/Zr, tracer of enrichment in the magmatic source; N-MORB, Primitive Mantle and E-MORB values of Sun and McDonough (1989). **e**, oxygen fugacity (ΔFMQ), determined by rock to zircon partitioning coefficients (ref. 37). **a-e** vs outcrop age, including: Supplementary Data 1 and 3. Symbols as in Figure 2. **f**, zircon Th/U, recognizing extensional and compressional periods in subduction environments (ref. 34). **g**, zircon Ti (ppm), to estimate Ti-in-zircon temperatures (ref. 35). **h**, zircon U/Yb, indicator of enrichment and/or crustal contamination of the magmatic source (ref. 13). **i**, zircon Eu-anomaly, to trace oxygen fugacity changes and plagioclase fractionation prior to zircon crystallization. **j**, zircon Ce/Nd, proxy for oxygen fugacity during zircon crystallization. **f-j** vs zircon $^{238}U/^{206}Pb$ age, including: this study (triangles) and Jara et al. (Chapter 2) (circles). **a-j**, symbol colors refer to age of plutonic complexes. Rhomboidal white symbols and lower and upper dotted black lines represent median, percentile 5% and 95% of each series (kernel density estimation with 2.5 Ma bandwidth and 5 Ma bin width, except for calculated oxygen fugacity). **LT**, Late Triassic (215-203 Ma). **EJ**, Early Jurassic (200-185 Ma). **LJ**, Late Jurassic (160-145 Ma). **V-EAp**, Valanginian to early Aptian (138-121 Ma). **LAp-EAlb**, late Aptian to early Albian (120-108 Ma). **LAlb-Cnm**, late Albian to Cenomanian (103-93 Ma).

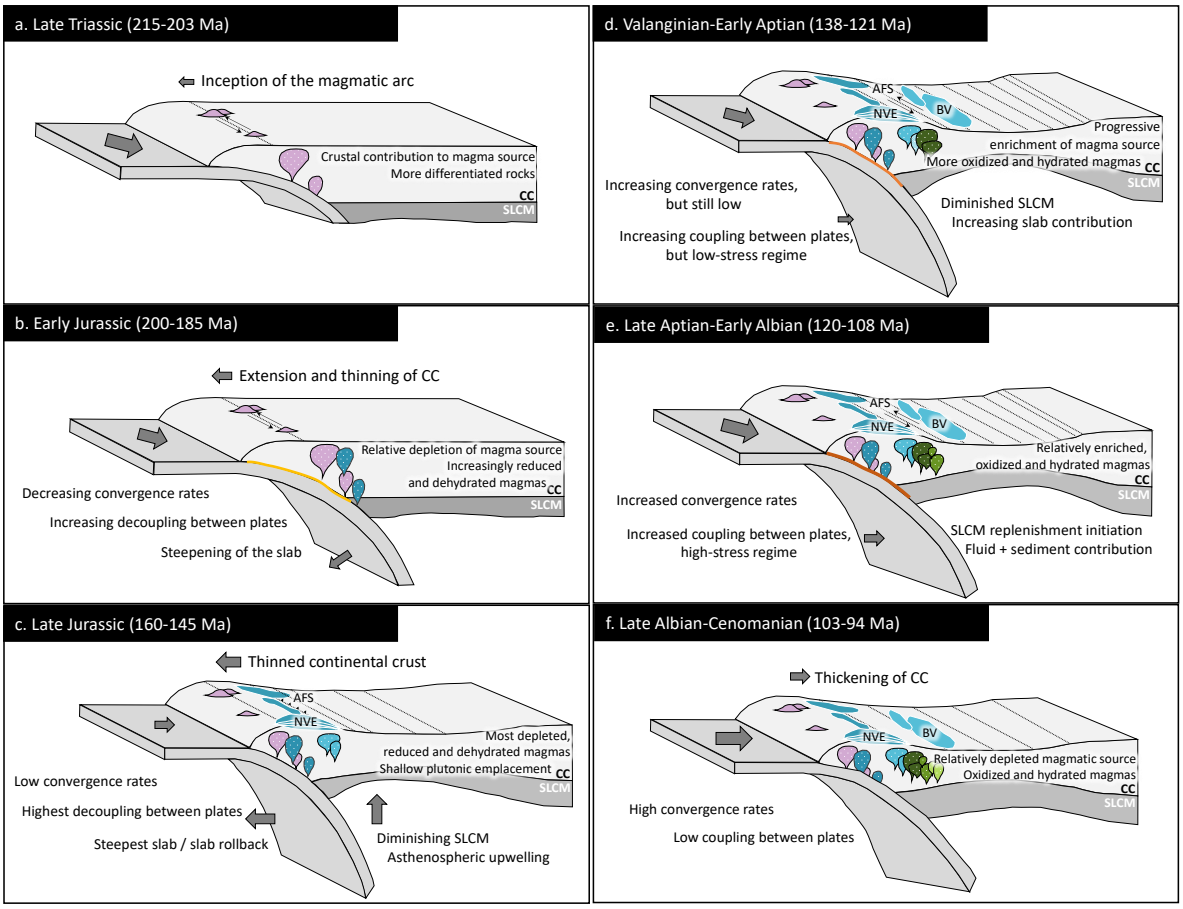

Figure 3.4. Multistage evolution of the early Andean Cordillera. a, Late Triassic plutonic episode (215-203 Ma) represents the inception of the early Andean magmatic arc in an attenuated continental arc, with crustal inputs to the magma source and the emplacement of granitic intrusions. **b-c**, Early Jurassic to Late Jurassic plutonic episodes (200-145 Ma). This transtensional to extensional period implied a reduction in sediment, slab-derived fluids and lithospheric mantle contributions to magma source, and finally triggered decompressional melting and the upwelling of asthenospheric material. This led to a progressively depleted, dehydrated and reduced magmatism during Late Jurassic. **d-e**, Valanginian to late Aptian plutonic episodes (138-108 Ma) showed the transition from an arc-normal extensional to a (low-stress?) transtensional setting with probably higher convergence rates and increasing plate coupling. As a result, subduction contributions progressively augmented, generating increasingly more enriched, hydrated and oxidized magmas. **f**, late Albian to Cenomanian plutonic episode (103-94 Ma) with supposedly high convergence rates and relative plate decoupling should have led to a relatively depleted mantle source but somewhat oxidized magmas.

CHAPTER 4. DISCUSSION AND CONCLUSIONS

Even though the early Andean Cordillera is a major morphotectonic domain that records more than a 100 million years of geologic history of the southwestern margin of Gondwana and South America (Mpodozis and Ramos, 1989; Charrier et al., 2007), it has received significantly less attention from the scientific community than its late Mesozoic to Cenozoic counterparts. This is probably due to two main reasons: i) the Principal Andean range host nearly 50% of global copper resources (Sillitoe and Perelló, 2005; Sillitoe, 2010) and it is also a relevant source for precious and base metals, and for other mineral products such as lithium, nitrates and borates (Sillitoe and Perelló, 2005); and ii) it is one of the most remarkable active continental arcs of the world, giving an incomparable opportunity to study orogenic and volcanic processes occurring in recent times (e.g., DeCelles et al., 2015; Wörner et al., 2018).

Nevertheless, the early Andean Cordillera presents some interesting features that makes it an excellent field to contribute to the knowledge of Cordilleran arc systems. It is a continental margin that was formed during a long-lasting, multistage extensional to transtensional subduction setting developed in an attenuated crust (Charrier et al., 2007; Seymour et al., 2020), a situation scarcely studied in terms of cyclical or episodic magmatism in magmatic arcs (Paterson and Ducea, 2015). Its vast plutonic units arranged in belts parallel to the trench are well-exposed along and across the domain, which also host significant arc and back-arc volcanic sequences that were preserved despite subsequent uplift and erosion (Parada et al., 2007; Oliveros et al., 2020). Moreover, tectonic and structural processes of this continental margin have been analyzed in detail through the study of its main structures, particularly the Atacama Fault System (e.g., Scheuber and Andriessen, 1990; Scheuber and González, 1999; Grocott and Taylor, 2002; Seymour et al., 2020). Finally, the early Andean Cordillera of southern Peru and northern Chile host a number of porphyry copper deposits and some of the most important Phanerozoic iron-oxide related mineralization systems of the world (Sillitoe, 2003; Barra et al., 2017; Simon et al., 2018; Creixell et al., 2020). Therefore, it is a fertile area to study the relationship between tectonic changes and magmatism, the evolution of an extensional continental arc, and the metallogenesis of magmatic-hydrothermal deposits.

Nevertheless, some volcanic and plutonic units belonging to this domain have been partially altered by subsequent metasomatic and/or metamorphic processes (Hervé et al., 2007; Rossel et al., 2015), leading to a restricted interpretation of the tectonic and magmatic events that occurred during its evolution by the sole use of whole-rock petrogenetic tools. This thesis confronted this challenge by focusing on the study of less altered plutonic units of the early Andean Cordillera of northern Chile, and the application of recently developed petrochronologic tools based on the chemistry of magmatic zircons, a mineral phase that is highly resilient to metamorphic and hydrothermal processes.

4.1. PRE-ANDEAN MAGMATISM, ONSET OF THE ANDEAN OROGENY AND EVOLUTION OF THE EARLY ANDEAN CONTINENTAL ARC

In **Chapter 2**, the first zircon U-Pb/trace element dataset of plutonic complexes from the Coastal Cordillera of northern Chile is presented, providing new constraints on the early evolution of the Andean orogeny. The oldest event in the study area (Cerros del Vetado pluton, ~247 Ma; Fig. 3A in **Chapter 2**) is interpreted as a transitional magmatism belonging to the pre-Andean tectonic cycle; a controversial result regarding recently published articles that contend for an extensional subduction setting as the origin of the pre-Andean magmatism (Del Rey et al., 2016; 2019; Coloma et al, 2017; Oliveros et al., 2020). This interpretation is based on several aspects of the sample obtained during this study, and its comparison with other intrusive units emplaced concurrently but in other morphotectonic domain or in the same morphotectonic domain but in the Late Triassic to Early Cretaceous. First, this sample shows a shoshonitic signature and a higher enrichment in LILE and HFSE than the samples obtained from other plutonic units of the early Andean Cordillera (Figs. 5 and 6 in **Chapter 2**). Second, its whole-rock geochemistry is similar to those of the El Colorado, Chollay and El León plutonic units, which were emplaced during Permian to Triassic times in the Frontal Andes and have been classified as transitional granitoids in previous studies (Fig. 10 in **Chapter 2**) (Mpodozis and Kay, 1992; Coloma et al., 2017; Del Rey et al., 2019). It also presents a completely different zircon chemistry compared to the other units sampled in the study, showing significantly lower Th/U ratios and higher Eu anomalies (Figs. 7A and 11C in **Chapter 2**). Moreover, the trace element contents of its zircon do not follow the general trend that could be trace from the latest Triassic to Early Cretaceous plutonic complexes of the Coastal Cordillera, suggesting that it was not related to the same subduction regime (Fig. 11 in C **Chapter 2**). Nevertheless, this interpretation should be taken carefully because it is based on only one sample. To reach a more definitive conclusion about the tectonic regime and the type of magmatism during the pre-Andean cycle, additional structural and petrologic studies are needed. The hypothesis advocating for a continuous subduction process with steepening and foundering of the slab, which possibly explains the retreat of the magmatic arc from the Frontal Andes to the Coastal Cordillera during this period, should be further tested considering some aspects arising from this study, such as: How could magmatism have been concurrently active in the frontal and coastal ranges (i.e., across the margin or perpendicular to the main axis of the magmatic arc) during Early to Middle Triassic in their proposed extensional subduction setting? How a transitional granitoid formed to the west of the proposed magmatic arc, in the foreland where subduction related magmatism is expected? Why there are no other Early to Middle Triassic intrusive units north and south of the Cerros del Vetado complex, forming an Early to Middle Triassic plutonic belt such as of those of the latest Triassic to Early Cretaceous ages? On the other hand, the anorogenic origin hypothesis for the Early to Middle Triassic magmatism in northern Chile should address the processes that led to extensive I-type granitoids in the Frontal Andes concurrent or after the emplacement of transitional units supposedly generated during the anorogenic pre-Andean tectonic cycle.

In contrast to the Early to Middle Triassic sample, the second oldest pluton sampled during this study (Quebrada Quiscuda stock, ~211 Ma; Fig. 4A in **Chapter 2**) presents typical characteristics of I-type, subduction related granitoids (Figs. 5 and 6 in **Chapter 2**) and similar zircon geochemical signatures with Jurassic to Early Cretaceous plutonic bodies in the early Andean Cordillera (Figs. 8, 9 and 11 in **Chapter 2**). Thus, based on our results the Quebrada Quiscuda is representative of the Andean tectonic cycle, and consequently we

propose that the Andean orogeny (in the study area) started at least 10 Ma before previous estimates, at around 210 Ma during the Norian stage.

Additionally, the geochronology results obtained in this novel study also indicate that plutons of the first stage of the Andean orogeny (latest Triassic-Early Cretaceous) were arranged in belts parallel to the trench with eastward decreasing ages in five plutonic pulses (Figs. 1 and 12 in **Chapter 2**), as suggested by previous studies (Berg and Baumann, 1985; Dallmeyer et al., 1996; Seymour et al., 2020). It also shows that the early Andean magmatism was generated from a rather depleted mantle source, corroborating the conclusions of previous petrologic studies in volcanic and plutonic units of the Coastal Cordillera (Pichowiak, 1994; Kramer et al., 2005; Lucassen et al., 2006; Oliveros et al., 2007; Oliveros et al., 2020). Moreover, this research was able to identify a relevant change in the characteristics of this magmatism that was not reported before, associated with a variation in the tectonic regime from ~150 to 130 Ma (Fig. 11 in **Chapter 2**). Less evolved signatures are found before the transition from extensional to transtensional settings, a transition that has been reported in a number of tectonic and structural studies (e.g., Dallmeyer et al., 1996; Scheuber and González, 1999; Grocott and Taylor, 2002; Seymour et al., 2020). After this change, magmas became enriched and more oxidized, possibly related to major slab contributions due to an increasing coupling between plates.

Chapter 3 deepens or understanding of the tectonic and magmatic evolution of the early Andean continental arc of southwestern Gondwanaland during latest Triassic to earliest Late Cretaceous (ca. 215 to 95 Ma). Expanding the study area and the findings of the previous chapter, the chemistry and ages of the zircon from the plutonic complexes of the Coastal Cordillera allowed us to: i) reject a stable tectonic framework for this period; ii) correlate the changes in the whole-rock and zircon chemistry of the samples with determined tectonic regimes over time; and iii) characterize the magmatic conditions of each substage in the tectonic cycle (Figs. 3 and 4 in **Chapter 3**). As a result, six plutonic episodes characterized by their zircon chemistry and previously described tectonic settings where identified (Figs. 2 and 3 in **Chapter 3**). The first one, occurred during the Late Triassic (215-203 Ma), and probably records the inception of the magmatic arc that presents higher crustal inputs and the most differentiated rocks of the whole study (Fig. 4a in **Chapter 3**), including significant granite units that are scarce for the other events of this arc (Fig. 2d in **Chapter 3**). The second and third events of Early (200-185 Ma) and Late (160-145 Ma) Jurassic ages evidence the extensional nature of the arc (Fig. 4b,c in **Chapter 3**) (Scheuber and González, 1999; Seymour et al., 2020). This could be observed in the thinning of the crust (Fig. 3a in Chapter 3), the depletion of the magmatic source (Figs. 3d,h in **Chapter 3**) and the reducing contribution of sediments and fluids from the slab (Fig. 4b,c in **Chapter 3**) (Pichowiak, 1994; Kramer et al., 2005; Lucassen et al., 2006; Oliveros et al., 2007). As a result, Late Jurassic plutons show the less evolved signatures, resembling a rather reduced and dehydrated, N-MORB like magmatism (Fig. 3d,i,j in **Chapter 3**).

The latter was followed by a major change in the tectonic regime from an arc-normal extensional to an oblique transtensional settings at ~150-130 Ma (Dallmeyer et al., 1996; Scheuber and González, 1999; Grocott and Taylor, 2002; Seymour et al., 2020). The fourth and fifth plutonic episodes record a significant flare-up in this extensional

continental margin during Valanginian to early Aptian (138-121 Ma) and late Aptian to early Albian (120-108 Ma) (Fig. 4d,e in **Chapter 3**). These two events are featured by a sustaining increase in the sediment and fluid contributions from the slab to the mantle wedge (Fig. 3b,c in **Chapter 3**), which probably resulted in the generation of more oxidized and hydrated magmas (Fig. 3i,j in **Chapter 3**). This process is better observed when both episodes are taken into account, since the progression in the geochemical signals is slow and smooth during the 30 My period. Therefore, some could argue that there is only one plutonic episode covering almost the entire Early Cretaceous magmatism in the Coastal Cordillera. However, the tectonic changes and the magmatic lull that occurred between both periods have been previously recognized in structural studies (Scheuber and González, 1999; Grocott and Taylor, 2002; Seymour et al., 2020), and could be traced in the zircon geochronological and geochemical records, most notoriously in the zircon U/Yb ratio (Fig. 3h in **Chapter 3**). Finally, the sixth and probably last plutonic episode of the early Andean continental arc developed between 103 and 94 Ma in the late Albian and Cenomanian (Fig. 4f in **Chapter 3**), postdating a short extensional process recorded by the generation of marginal basins in the back-arc and the deposition of sedimentary and volcanic units of continental origin (Mpodozis and Allmendinger, 1993). This event shows mixing geochemical signals with crustal thickness, slab-derived fluid contribution and magma oxygen fugacity proxies rising (Fig. 3a,c,i,j in **Chapter 3**) without a relevant increase in the enrichment of the magmatic source (Fig. 3d,h in **Chapter 3**). One possible explanation of this scenario is that the convergence rate between the oceanic and continental plates augmented but their coupling decreased due to a higher subduction angle (Fig. 4f in **Chapter 3**). An alternative is that these plutons are the very early products of the compressional subduction setting that marks the initiation of second stage of the Andean orogeny. In this case, the rather depleted magmatic source of the arc resulted from the exhaustion of the subcontinental lithospheric mantle during the long-lasting extensional to transtensional regime of the Late Triassic to the Early Cretaceous. Nevertheless, to decipher this conundrum additional structural, geochronological and petrological studies related to this plutonic episode are needed.

4.2. PRELIMINARY DISCUSSION ABOUT THE IMPLICATIONS FOR THE METALLOGENESIS OF THE EARLY ANDEAN CORDILLERA

The study area of this thesis is commonly known as the Chilean Iron Belt by the economic geology community, because it hosts some of the most significant Mesozoic iron oxide, copper and gold (IOCG) deposits of the world (Fig. 1). It includes relevant copper-poor endmembers of this '*clan of deposits*' such as Los Colorados and El Romeral (iron oxide-apatite deposits, IOA), and copper-rich examples as Candelaria and Mantoverde (IOCG '*sensu stricto*' deposits; IOCG deposits onwards). Additionally, relevant porphyry copper operations, like Andacollo and Dos Amigos-Tricolor are located within its geographical and temporal limits.

The '*clan of IOCG deposits*' has been controversial since its inception (Porter, 2000; Barton, 2014), probably due to the broad definition made by its creators based on some common characteristics shared by the studied deposits (Hitzman et al., 1992) and not in the processes involved in their formation. Some of the distinctive features that were

initially proposed has undergone relevant variations over time, for example including the IOA or Kiruna-type deposits, the Phanerozoic IOCG deposits of the Central Andes and those of the Carajás province in Brazil belonging to the Archean (Pollar, 2000; Porter, 2000). Additionally, other authors include in this group of deposits the high-grade Cu-Au systems with low Fe contents such as Mt. Isa, Starra, Peko and Tick Hill in Australia (Haynes, 2000; Groves et al., 2010) and others with a mineralogy quite different from the initial criteria (Barton, 2014). Therefore, currently the '*clan of IOCG deposits*' is broadly defined as a family of geologically diverse mineral deposits that: (1) have low-Ti iron oxides in concentrations greater than 10%; (2) they present geochemically high contents of Cu, Au, REE, P, U, Ag and Co; (3) they are usually structurally or stratigraphically controlled; and (4) are spatially and temporally associated with high volume, intensive Na-Ca-K metasomatic events. However, as a group they lack a unique tectonic setting and an unequivocal relationship with magmatic processes, key variables to characterize and understand the genesis of other types of magmatic-hydrothermal deposits such as porphyry systems (Barton, 2014). This broad definition is useful to differentiate them from other types of deposits that share some features with IOCG systems, such as banded iron formations (BIF), magmatic iron-titanium systems associated with anorthosite intrusions, and other hydrothermal iron deposits such as porphyries with high magnetite content or iron skarns with high copper and gold contents (Barton, 2014). However, this broad definition does not provide unequivocal information about the genesis of these deposits.

Although there is extensive literature and multiple hypotheses on the origin of the IOCG systems, these can be summarized in four main genetic models: (1) a magmatic model, primarily associated with IOA deposits, where the essential mineralizing fluid is an immiscible melt that is rich in iron and volatiles; (2) a magmatic-hydrothermal model, where the main fluid is aqueous but from a magmatic origin; (3) a basin model, in which the essential fluids are surface brines or non-magmatic basinal fluids that circulate thanks to the heat delivered by igneous processes or geothermal gradients; and (4) a metamorphic model, where the fluids come from the devolatilization of minerals and the exsolution of fluids in metamorphic processes and the fluid-rock interaction at depth (Barton and Johnson, 2004; Williams et al., 2005; Barton, 2014). In addition, there are other possible explanations for the formation of these deposits, for example, the superimposition of copper-gold mineralizing events in older rocks rich in iron oxides (Skirrow and Walshe, 2002; Mark et al., 2006) or the gradation from the magmatic model to the magmatic-hydrothermal model based in the flotation of magmatic magnetite suspensions (Knipping et al., 2015; Reich et al., 2016). Moreover, there have been other proposals that integrate more than one of the previously described genetic models. For example, Vila et al. (1996) recognize the similarities between the Mantoverde IOCG system and surrounding IOA deposits, proposing a magmatic-hydrothermal continuum between the IOA and the IOCG mineralized systems. Analogously, Sillitoe (2003) proposes a relationship between IOA and IOCG deposits in which the former are the deep expression of a magmatic-hydrothermal system and the latter represent their middle to upper part. Marschik and Fontboté (1996) make a similar comparison but placing IOCG deposits in a transition between the IOA and porphyry copper deposits. Finally, in his postgraduate thesis on the Santo Domingo Sur deposit, Daroch (2011) relates the IOCG system with the stratabound Cu (-Ag) deposits of northern Chile. In his proposal, the latter would be a low-temperature, distal expression of the former.

All these genetic models incorporate a close spatial and temporal relationship between the mineralization and magmatism. However, only a few examples of a direct connection of these geological processes are available (Rojas et al., 2018). Therefore, it is not possible to unequivocally relate the genesis of the '*clan of IOCG deposits*' to particular intrusive units or to specific tectono-magmatic conditions (Williams et al., 2005; Barton, 2014). The igneous units spatially and temporally related to IOCG deposits cover the entire compositional spectrum: from mafic to felsic rocks, usually sub-alkaline to rarely alkaline, and generally oxidized (Barton, 2014). Additionally, trace element analysis indicates that both arc and intraplate magmatism may be involved (Hitzman, 2000; Pollard, 2000; Haynes, 2000; Pollard, 2006; Barton, 2014). In the case of the Chilean Iron Belt, the associated intrusive complexes are metaluminous, calc-alkaline, subduction related intrusions of mainly diorites with minor tonalites and granodiorites; and all of them are relatively oxidized, thus belonging to the magnetite series (Sillitoe, 2003). However, these characteristics only represent the generality of the intrusive complexes in the different IOCG districts associated with convergent margins worldwide, and in most continental arcs developed in rather thinned crusts. Therefore, does not allow to correlate the genesis and the origin of the metal endowment of these mineralized systems with the magmatic conditions in the arc. Nevertheless, the results presented in **Chapter 2** and **Chapter 3** give some insights of the role that tectono-magmatic changes and magmatic conditions could have played in the formation of the Andean IOA and IOCG systems, and in the genesis of Cretaceous porphyry Cu-Au deposits.

Figure 2 summarizes some of the relevant petrologic indicators analyzed in **Chapter 3** but including the ages of formation for major IOA, IOCG and porphyry copper deposits of the Chilean Iron Belt. As it can be seen from the figure, most IOA deposits were formed during the fourth plutonic episode of the early Andean Cordillera, between 132 and 128 Ma and probably concurrent or after the transition from the extensional to transtensional tectonic setting (Fig. 2g). This result suggest that magmatism not only contributed to the formation of IOA and IOCG deposits as a heat source for basinal fluids to scavenge elements from country rocks, as proposed by Barton and collaborators (e.g., Barton and Johnson, 1996; 2000; Barton et al., 2005), but probably as the main source of the mineralizing fluids and the metals deposited in these systems. Back-arc volcano-sedimentary units of latest Jurassic to earliest Cretaceous age (~150-135 Ma) are the main country rocks hosting IOA and IOCG deposits (Sillitoe, 2003). These units were intruded and chemically modified by the shallow emplacement of some intrusions of the third and by the complexes of the fourth, fifth and sixth plutonic episodes. Thus, all the elements needed to generate the IOA and IOCG systems in the basin model (Barton and Johnson, 1996) were in place before the tectonic change occurred at ca. 130 Ma in the study area (Dallmeyer et al., 1996; Grocott and Taylor, 2002; Seymour et al., 2020). However, no significant deposits were formed during that time span (Fig. 2g). Prior to the change in the tectonic setting the magmatism in the continental arc was driven mainly by asthenospheric upwelling and decompressional melting (Fig. 4c in **Chapter 3**), generating relatively depleted, reduced and dehydrated magmas (Fig. 2d-f) due to the scarce contribution of sediments and fluids to the mantle wedge (Fig. 2b,c). This type of magmatism does not have the proper conditions to mobilize from the magma source the siderophile and chalcophile elements that are characteristic of IOA and IOCG deposits. This situation

explains why these systems were not formed earlier in the evolution of the continental arc if a magmatic-hydrothermal model is argued for their origin.

In contrast, the shift to a transtensional tectonic setting brought slight but growing sediment and fluid additions to the magmatic factory (Fig. 2b,c), generating comparatively more enriched, hydrated and oxidized magmas during the fourth plutonic event (Fig. 4d in **Chapter 3**). Though, the enrichment of the source and the oxygen fugacity of the magmas during this episode (Fig. 2d-f) would have not been sufficient to scavenge the key elements from the mantle that are necessary to form the IOCG deposits but enough to trigger the genesis of IOA systems. Consequently, only a few IOCG deposits were generated between 138 and 120 Ma, being the most relevant ones formed in the fifth plutonic episode after 120 Ma (i.e., Candelaria, Mantoverde and Punta del Cobre) (Fig. 2g). The crustal thickening occurred during the fifth episode, together with the continuous addition of sediments and slab-derived fluids to the magma source during more than 15 My (Fig. 2a-c) produced more enriched, hydrated and oxidized magmas compared to their predecessor plutonic episode (Fig. 2d-f). As a result, these magmas could have been able to incorporate siderophile and chalcophile elements from the mantle since volatile ligands, such as sulfur and chlorine, were increasingly available (Richards et al., 2017). This process may have help to enhance the formation of the most relevant IOCG deposits in the early Andean Cordillera between 120 and 110 Ma. These results support a magmatic-hydrothermal origin for the mineralized fluids of IOA and IOCG deposits. Finally, the porphyry Cu-Au deposits within this geologic domain are prompt to be found at the end of the fifth and during the sixth plutonic event (Figs. 4e,f in **Chapter 3**), possibly concurrent or shortly after the initiation of the compressional subduction setting that is characteristic of modern Andes (Mpodozis and Allmendinger, 1993).

4.3. CONCLUSIONS

This research provides new constraints on the tectono-magmatic evolution of the southwestern border of Gondwana during the first stage of the Andean orogeny. In this study, the first regional dataset of U-Pb geochronology and geochemistry of zircon from plutonic complexes in the early Andean Cordillera of northern Chile was published. The new evidence presented here, coupled with current knowledge of the tectonic and structural evolution of this continental margin, allow to conclude:

- A restricted (?) transitional magmatism is responsible for the generation of the pre-Andean plutonic complexes of the early Andean Cordillera. In particular, for the Early to Middle Triassic Cerros del Vetado pluton (~247 Ma).
- The Andean orogeny would have started ca. 215 Ma during the Norian stage, at least 10 to 15 million years before previous estimates.
- The early Andean continental arc produced episodic magmatism that was mainly driven by multiple tectonic stages in a subduction setting. As a result, six plutonic events organized in belts parallel to the trench with eastward decreasing ages were identified between 215 and 94 Ma.
- The plutonic episodes were recognized and described by using whole-rock and zircon petrochronologic indicators and can be related to specific tectonic changes occurred in the continental margin.

- Consequently, the plutonic complexes of the early Andean Cordillera have typical calc-alkaline, metaluminous to slightly peraluminous affinities of I-type granitoids. However, due to the long-lasting extensional to transtensional tectonic regime governing the evolution of the arc, this magmatism had a rather depleted mantle source.
- As the arc evolved and migrated to the east, variable slab-derived fluids and sediment contributions to the mantle wedge were recorded. Increasingly depleted, reduced and dehydrated magmas are associated with the latest Triassic to latest Jurassic period, until the transition from an arc normal extensional to an oblique transtensional tectonic setting occurred in the earliest Cretaceous. After this tectonic change, the geochemical signature of the magmas indicates growing contributions of fluids and sediments from the slab. Therefore, Early Cretaceous plutonic units were produced from magmas increasingly more enriched, oxidized and hydrated over time.
- This succession of tectono-magmatic events give some insights on the spatial and temporal distribution of iron oxide (IOA and IOCG) and porphyry Cu-Au mineralized systems in the early Andean Cordillera, and contributes to the growing evidence supporting a magmatic-hydrothermal origin for the former group of deposits.

Finally, these results are relevant to understand tectonic cycles, subduction and magmatism in continental arcs not as long-lasting processes or particular occurrences that are independent from former or later events, but as complex systems that are interconnected and evolve through time.

4.4. BIBLIOGRAPHY

Barra, F., Reich, M., Selby, D., Rojas, P., Simon, A., Salazar, E., Palma, G., 2017. Unraveling the origin of the Andean IOCG clan: A Re-Os isotope approach. Ore Geology Review 81, 62-78.

Barton, M.D., 2014. Iron oxide(-Cu-Au-REE-P-Ag-U-Co) systems. Treatise on Geochemistry, 2nd edition, Volume 11, Chapter 23, 515-541. Elsevier.

Barton, M.D., Johnson, D.A., 1996. Evaporitic source model for igneous-related Fe oxide-(REE-Cu-Au-U) mineralization. Geology, 24, 259-262.

Barton, M.D., Johnson D.A., 2000. Alternative brine sources for Fe-oxide (Cu-Au) systems: Implications for hydrothermal alteration and metals. En Porter T.M. (ed.) Hydrothermal Iron Oxide Copper–Gold and Related Deposits: A Global Perspective, 43-60. Glenside, SA., Australian Mineral Foundation.

Barton M.D. y Johnson D.A. (2004). Footprints of Fe-oxide (-Cu-Au) Systems, SEG 2004 Predictive Mineral Discovery Under Cover. Centre for Global Metallogeny, University of Western Australia, Special Publication 33, 112-116.

Barton, M.D.; Jensen, E.P.; Ducea, M. 2005. Fluid sources for IOCG and porphyry Cu-style mineralization, Copiapo batholith, Chile: Geologic and Sr isotopic constraints. Geological Society of America Abstracts with Programs 37, 316.

Berg, K., Baumann, A., 1985. Plutonic and metasedimentary rocks from the Coastal Range of northern Chile: Rb-Sr and U-Pb systematic. Earth and Planetary Science Letters 75, 101-115.

Charrier, R., Pinto, L., Rodríguez, M. P., 2007. Tectonostratigraphic evolution of the Andean Orogen in Chile. In Moreno, T., and Gibbons, W., eds., The geology of Chile: London, The Geological Society, p. 21-114.

Coloma, F., Valin, X., Oliveros, V., Vásquez, P., Creixell, C., Salazar, E., Ducea, M.N., 2017. Geochemistry of permian to triassic igneous rocks from northern Chile (28°-30°15‘S): Implications on the dynamics of the proto-Andeanmargin. Andean Geology 44, 147–148.

Creixell, C., Fuentes, J., Bierma, H., Salazar, E., 2020. Tectonic setting of Cretaceous porphyry copper deposits of northern Chile (28°-30° S) and its relations with magmatic evolution and metallogeny. Andean Geology 47, 469-507.

Dallmeyer, R.D., Brown, M., Grocott, J., Taylor, G., Treloar, P., 1996. Mesozoic magmatic and tectonic events within the Andean plate boundary zone, north Chile: constraints from 40Ar/39Ar minerals ages. Journal of Geology 104, 19-40.

Daroch, G. (2011). Hydrothermal alteration and mineralization of the iron oxide-(Cu-Au) Santo Domingo Sur deposit, Atacama region, northern Chile. Memoria de Magíster en geología, Departamento de Geociencias, Universidad de Arizona: 1-90.

DeCelles, P. G., Zandt, G., Beck, S. L., Currie, C. A., Ducea, M. N., Kapp, P., Gehrels, G. E., Carrapa, B., Quade, J., Schoenbohm, L. M., 2015. Cyclical orogenic processes in the Cenozoic central Andes. In M. N. Ducea, M. N. Ducea, P. G. DeCelles, P. A. Kapp, & B. Carrapa (Eds.), Geodynamics of a Cordilleran Orogenic System: The Central Andes of Argentina and Northern Chile (pp. 459-490). (Memoir of the Geological Society of America; Vol. 212). Geological Society of America.

Del Rey, A., Arriagada, C., Dekart, K., Martínez, F., 2016. Resolving the paradigm of the late Paleozoic-Triassic Chilean magmatism: Isotopic approach. Gondwana Research 37, 172-181.

Del Rey, Dekart, K., Planavsky, N., A., Arriagada, C., Martínez, F., 2019. Tectonic evolution of the southwestern margin of Pangea and its global implications: Evidence from the mid Permian–Triassic magmatism along the Chilean-Argentine border. Gondwana Research 76, 303-321.

Goldfarb, R.J., and Richards, J.P., eds., One Hundredth Anniversary Volume. Society Of Economic Geologists: Denver.

Grocott, J., Taylor, G.K., 2002. Magmatic arc fault systems, deformation partitioning and emplacement of granitic complexes in the Coastal Cordillera, northern Chilean Andes (25°30’S to 27°00’S). Journal of the Geological Society of London 159, 425-442.

Groves D.I.P., Bierlein F.P., Meinert L.D., y Hitzman M.W. (2010). Iron oxide copper-gold (IOCG) deposits through Earth history, implications for origin, lithospheric setting, and distinction from other epigenetic iron oxide deposits. Economic Geology, 105, 641-654.

Haynes D. (2000). Iron oxide copper(–gold) deposits: Their position in the ore deposit spectrum and modes of origin. En Porter TM (ed.) Hydrothermal Iron Oxide Copper–Gold and Related Deposits: A Global Perspective, vol. 1, pp. 71–90. Adelaide: PGC Publishing.

Hervé, F., Faúndez, V., Calderón, M., Massone, H., Willner, A., 2007. Metamorphic and plutonic basement complexes. In The Geology of Chile (Gibbons, W., Moreno, T., editors). The Geological Society, Special Publication, 5-19. London.

Hitzman M.W. (2000). Iron oxide-Cu-Au deposits: What, where, when, and why? En Porter TM (ed.) Hydrothermal Iron Oxide Copper-Gold and Related Deposits: A Global Perspective, vol. 1, pp. 9–25. Adelaide: PGC Publishing.

Hitzman, M.W., Oreskes, N. y Einaudi, M.T. (1992). Geological characteristics and tectonic setting of Proterozoic iron oxide (Cu-U-Au-REE) deposits. Precambrian Research, 58, 241-287.

Knipping, J.L.; Bilenker, L.D.; Simon, A.C.; Reich, M.; Barra, F.; Deditius, A.P.; Lundstrom, C.; Bindeman, I.; Munizaga, R. 2015. Giant Kiruna-type deposits form by efficient flotation of magmatic magnetite suspensions. Geology 43, 591-594.

Kramer, W., Siebel, W., Romer, R. L., Haase, G., Zimmer, M., Ehrlichmann, R., 2005. Geochemical and isotopic characteristics and evolution of the Jurassic volcanic arc between Arica (18°30'S) and Tocopilla (22°S), North Chilean Coastal Cordillera. Chemie der Erde - Geochemistry, 65 (1), 47-78.

Lucassen, F., Kramer, W., Bartsch, V., Wilke, H.G., Franz, G., Romer, R.L., Dulski, P., 2006. Nd, Pb and Sr isotope composition of juvenile magmatism in the Mesozoic large magmatic province of northern Chile (18°-27°S): indications for a uniform subarc mantle. Contributions to Mineralogy and Petrology 152: 571-589.

Mark, G., Oliver, N.H.S. y Williams, P.J. (2006). Mineralogical and chemical evolution of the Ernest Henry Fe oxide-Cu-Au ore system, Cloncurry district, Northwest Queensland, Australia. Mineralium Deposita, 40, 769-801.

Marschik, R. y Fontboté, L. (1996). Copper(-Iron) Mineralization and Superposition of Alteration Events in the Punta Del Cobre Belt, Northern Chile. En Andean copper deposits: New discoveries, mineralization, styles and metallogeny. Society of Economic Geologists Special Publication, 5, Camus, F., Sillitoe, R., and Petersen, R. eds., 171-190.

Mpodozis, C., Allmendinger, R.W., 1993. Extensional tectonics, Cretaceous Andes, northern Chile (27°S). Geological Society of America Bulletin 105, 1462-1477.

Mpodozis, C., Kay, S.M., 1992. Late Paleozoic to Triassic evolution of the Gondwana margin, evidence from Chilean Frontal Cordillera batholiths (28°S to 31°S). The Geological Society of America, Bulletin 104 (8), 999-1014.

Mpodozis, C., Ramos, V.A., 1989. The Andes of Chile and Argentina. In Geology of the Andes and its Relation to Hydrocarbon and Mineral Resources, Ericksen, G.E., Cañas-Pinochet, M.T., Reinemud, J.A. (eds). Circumpacific Council for Energy and Mineral Resources. Earth Sciences Series 11, 59–90. Houston, Texas.

Oliveros, V., Morata, D., Aguirre, L., Féraud, G., Fornari, M. 2007. Jurassic to Early Cretaceous subduction-related magmatism in the Coastal Cordillera of northern Chile (18°30’-24°S): geochemistry and petrogenesis. Revista Geológica de Chile 34, 209-232.

Oliveros, V., Vásquez, P., Creixell, C., Lucassen, F., Ducea, M.N., Ciocca, I., González, J., Espinoza, M., Salazar, E., Coloma, F., Kasemann, S.A., 2020. Lithospheric evolution of the Pre- and Early Andean convergent margin, Chile. Gondwana Research 80, 202-227.

Parada, M. A., López-Escobar, L., Oliveros, V., Fuentes, F., Morata, D., Calderon, M., Aguirre, L., Féraud, G., Espinoza, F., Moreno, H., Figueroa, O., Muñoz-Bravo, J.,

Troncosco-Vásquez, R., and Stern, C. R., 2007. Andean magmatism. In Moreno, T., and Gibbons, W., eds., The geology of Chile: London, The Geological Society, p. 115-146.

Paterson, S.R., Ducea, M.N., 2015. Arc magmatic tempos: Gathering the evidence. Elements 11, 91-98.

Pichowiak, S. 1994. Early Jurassic to Early Cretaceous magmatism in the Coastal Cordillera and the Central Depression of North Chile. In Reutter, K.J., Scheuber, E., Wigger, P., editors, Tectonics of the Southern Central Andes: Heidelberg, Springer, p. 203-217.

Pollard, P.J. (2000). Evidence of a magmatic fluid and metal source for Fe-oxide Cu-Au mineralisation. En Porter TM (ed.) Hydrothermal Iron Oxide Copper-Gold and Related Deposits: A Global Perspective, vol. 1, pp. 27–46. Adelaide: Australian Mineral Foundation.

Pollard, P.J. (2006). An intrusion-related origin for Cu-Au mineralization in iron oxide-copper-gold (IOCG) provinces. Mineralium Deposita, 41, 179-187.

Porter, T.M. (ed.) (2000) En Hydrothermal Iron Oxide Copper–Gold and Related Deposits: A Global Perspective, vol. 1, pp. 349. Adelaide: PGC Publishing.

Reich, M.; Simon, A.; Deditius, A.; Barra, F.; Chryssoulis, S.; Lagas, G.; Tardani, D.; Knipping, J.; Bilenker, L.; Sánchez-Alfaro, P.; Roberts, M.; Munizaga, R. 2016. Trace element signature of pyrite from the Los Colorados Iron Oxide-Apatite (IOA) deposit, Chile: A missing link between Andean IOA and Iron Oxide Copper Gold systems? Economic Geology 111 (3): 743-761.

Richards, J., López, G.P., Zhu, J., Creaser, R.A., Locock, A., & Mumin, A. (2017). Contrasting Tectonic Settings and Sulfur Contents of Magmas Associated with Cretaceous Porphyry Cu ± Mo ± Au and Intrusion-Related Iron Oxide Cu-Au Deposits in Northern Chile. Economic Geology, 112, 295-318.

Rojas, P., Barra, F., Reich, M., Deditius, A.P., Simon, A., Uribe, F., Romero, R., & Rojo, M. (2018). A genetic link between magnetite mineralization and diorite intrusion at the El Romeral iron oxide-apatite deposit, northern Chile. Mineralium Deposita, 53, 947-966.

Rossel, P., Oliveros, V., Ducea, M., Hernandez, L., 2015. Across and along arc geochemical variations in altered volcanic rocks: Evidence from mineral chemistry of Jurassic lavas in northern Chile, and tectonic implications. Lithos 239, 97-113.

Scheuber, E., Andriessen, P.A.M., 1990. The kinematic and geodynamic significance of the Atacama fault zone, northern Chile. Journal of Structural Geology 12, 24-257.

Scheuber, E., González, G., 1999. Tectonics of the Jurassic-Early Cretaceous magmatic arc of the north Chilean Coastal Cordillera (22°-26°S): A story of crustal deformation along a convergent plate boundary. Tectonics 18 (5), 895-910.

Seymour, N. M., Singleton, J. S., Mavor, S. P., Gomila, R., Stockli, D. F., Heuser, G., Arancibia, G., 2020. The relationship between magmatism and deformation along the intra-arc strike-slip Atacama fault system, northern Chile. Tectonics 39, e2019TC005702.

Sillitoe, R.H. (2003). Iron oxide-copper-gold deposits: An Andean view. Mineralium Deposita, 38, 787-812.

Sillitoe, R.H., 2010. Porphyry Copper Systems. Economic Geology 105, 3-41.

Sillitoe, R.H., Perelló, J., 2005. Andean copper province: tectonomagmatic settings, deposit types, metallogeny, exploration, and discovery. In Hedenquist, J.W., Thompson, J.F.H.,

Simon, A., Knipping, J., Reich, M., Barra, F., Deditius, A., Bilenker, L., Childress, T., 2018. A holistic model that combines igneous and magmatic-hydrothermal processes to explain Kiruna-type iron oxide-apatite deposits and iron oxide-copper-gold deposits as products of a single evolving ore system. Society of Economic Geologists, Special Publication 21, 89-114.

Skirrow, R.G. y Walshe, J.L. (2002). Reduced and oxidized Au-Cu-Bi iron oxide deposits of the Tennant Creek inlier, Australia: An integrated geologic and chemical model. Economic Geology, 97, 1167-1202.

Vila, T., Lindsay, L. y Zamora, R. (1996). Geology of the Manto Verde copper deposit, northern Chile: A specularite-rich, hydrothermal-tectonic breccia related to the Atacama Fault Zone. En Andean copper deposits: new discoveries, mineralization, styles and metallogeny. Society of Economic Geologists, Special Publication, 5, 157-170.

Williams, P.J., Barton, M.D., Johnson, D.A., Fontbote, L., De Haller, A., Mark, G., Oliver, N.H.S. y Marschik, R. (2005). Iron oxide copper-gold deposits: geology, space-time distribution, and possible modes of origin. Economic Geology 100th Anniversary Volume, 100, 371-406.

Wörner, G., Mamani, M., Blum-Oeste, M., 2018. Magmatism in the Central Andes. Elements 14, 237-244.

4.5. FIGURES

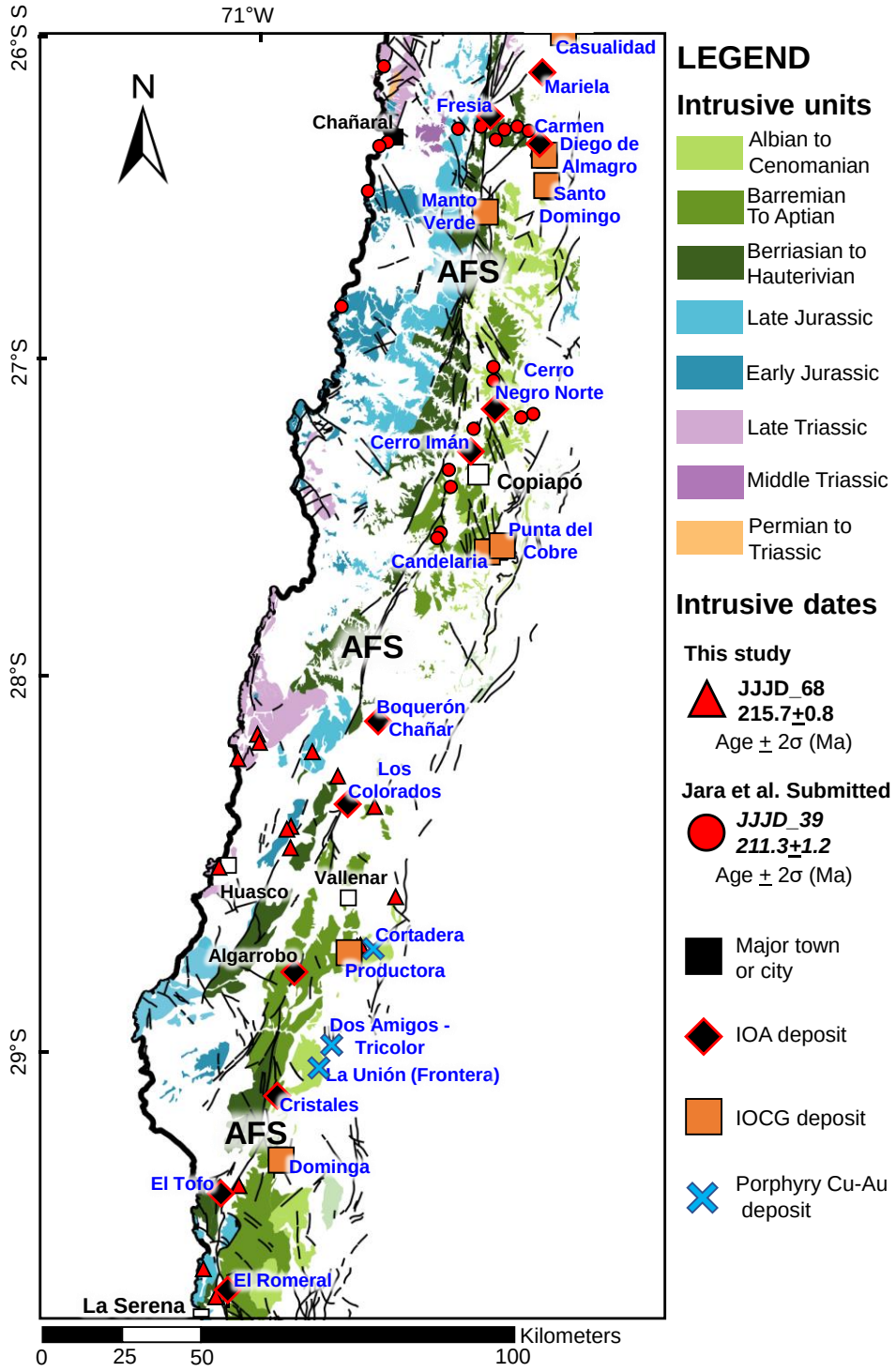

Figure 1. **Main mineral deposits and plutonic complexes of the early Andean Cordillera of northern Chile.** Distribution of relevant mineral deposits (IOA, IOCG and Cretaceous porphyry Cu-Au) and plutonic belts in the study area. **AFS**, Atacama Fault System.

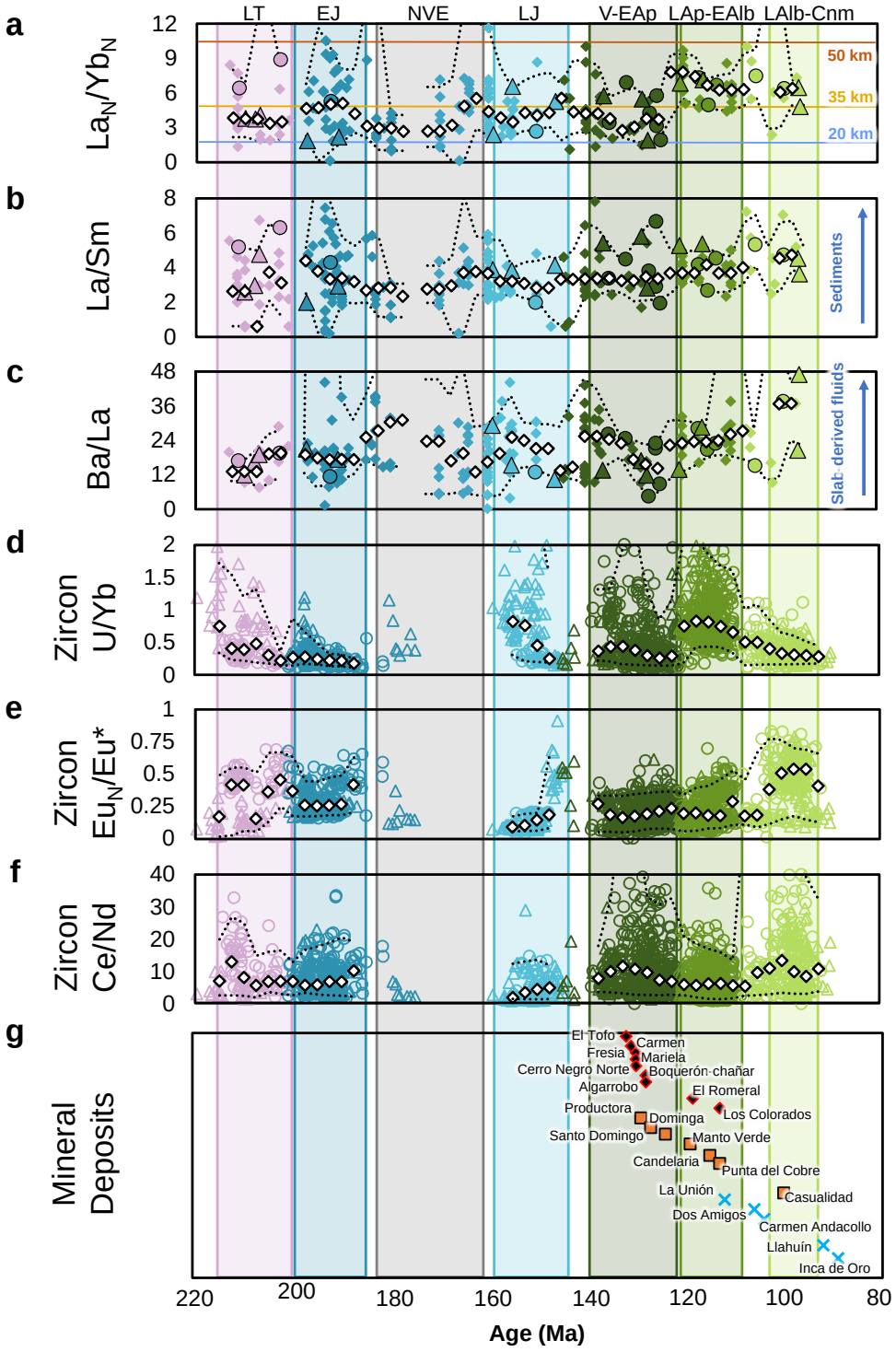

Figure 3. Zircon and whole-rock petrogenetic indicators of the evolution of the early Andean Cordillera and age of most relevant mineral deposits of this domain. a, La_N/Yb_N, to estimate crustal thickness (Profeta et al., 2015). **b-c**, La/Sm and Ba/La, proxies for sediments and slab-derived fluids contribution to magma genesis. **a-c** vs outcrop age, including: Supplementary Data 1 and 3 from **Chapter 3**. Symbols as in Figure 2 of **Chapter 3**. **d**, zircon U/Yb, indicator of enrichment and/or crustal contamination of the

magmatic source (Grimes et al., 2015). **e**, zircon Eu-anomaly, to trace oxygen fugacity changes and plagioclase fractionation prior to zircon crystallization. **f**, zircon Ce/Nd, proxy for oxygen fugacity during zircon crystallization. **d-f** vs zircon $^{238}U/^{206}Pb$ age, including: data from **Chapter 2** (circles) and **Chapter 3** (triangles). **a-f**, symbol colors refer to age of plutonic complexes. Rhomboidal white symbols and lower and upper dotted black lines represent median, percentile 5% and 95% of each series (kernel density estimation with 2.5 Ma bandwidth and 5 Ma bin width, except for calculated oxygen fugacity). **g**, age of most relevant IOA (Barra et al., 2017; Gelcich et al., 2005; Montecinos, 1985; Morales, 2017; Palma, 2020; Rojas et al., 2015; Salazar et al., 2019; Zentilli, 1974), IOCG (Arévalo et al., 2006; Barra et al., 2017; Daroch et al., 2015; Kovacic, 2014; Marquardt et al., 2015; Marschik and Fontboté, 2001; Rieger et al., 2010; Veloso et al., 2017) and porphyry Cu-Au (Maksaev et al., 2010; Creixell et al., 2015; Richards et al., 2017) deposits of the Chilean Iron Belt. **LT**, Late Triassic (215-203 Ma). **EJ**, Early Jurassic (200-185 Ma). **LJ**, Late Jurassic (160-145 Ma). **V-EAp**, Valanginian to early Aptian (138-121 Ma). **LAp-EAlb**, late Aptian to early Albian (120-108 Ma). **LAlb-Cnm**, late Albian to Cenomanian (103-93 Ma).

APPENDICES

A.1. SUPPLEMENTARY MATERIAL FOR CHAPTER 2

SM1. Analytical methods

Analytical methods – Obtained from GeoAnalytical Lab, Washington State University.

https://environment.wsu.edu/facilities/geoanalytical-lab/technical-notes/ (accessed October, 2020)

XRF analysis of rocks and minerals for major and trace elements

Johnson, D.M., Hooper P.R., and Conrey, R.M. (1999). XRF Analysis of Rocks and Minerals for Major and Trace Elements on a Single Low Dilution Li-tetraborate Fused Bead. GeoAnalytical Lab, Washington State University. Advances in X-ray Analysis 41, 843-867.

Abstract

The precision and accuracy of a low (2:1) Li-tetraborate fused bead technique by X-ray fluorescence analysis for 27 major and trace elements is demonstrated by comparison to accepted values of standard samples and to values acquired by other techni ques in other laboratories. The increased efficiency of using a single bead for major and trace elements is achieved without loss of precision or accuracy and the beads may be stored for tens of years without degradation.

Introduction

Of the many advantages in applying X-ray fluorescence (XRF) to the analysis of rocks and minerals, one of the most obvious is the versatility of the instrumentation. Methods can be developed to satisfy a wide variety of needs. In the GeoAnalytical Laboratory of Washington State University, the method developed over a period of more than 30 years (e. g. Hooper, 1964) was originally designed to distinguish the subtle chemical differences between flows of the Columbia River Basalt Group. To trace these flows over the Columbia Plateau required larger than normal numbers of analyses for the maximum number of elements and the highest possible analytical precision, while retaining the best available absolute accuracy. The approach finally adopted includes three separate components which differ from the more commonly employed methods based primarily on the work of Norrish and Hutton (1969). First, a single low dilution (2:1 diLi-tetraborate: sample) fusion is used for both major and trace elements, providing maximum efficiency without loss of accuracy. Second, a constant voltage on a Rh target is used for all elements to achieve maximum long-term stability and precision, despite this causing less than perfect conditions for a few trace elements. Third, the oxidation state of iron and the volatile content of the rock are ignored. The original major element concentrations are then normalized to 100%, volatile-free, with all the iron expressed as FeO.

Single bead low-dilution fusion technique

Sample Preparation

Fresh chips of the sample are handpicked and a standard volume of chips (approximately 28 g) is ground in a swing mill with tungsten carbide surfaces for 2 minutes. Three and a half grams (3.5 g) of the sample powder is weighed into a plastic mixing jar with 7.0 g of spec pure dilithium tetraborate (Li2B4O7) and, assisted by an enclosed plastic ball, mixed for ten minutes. The mixed powders are emptied into graphite crucibles with internal measurements of 34.9 mm diameter by 31.8 mm deep. Twenty-four (24) filled crucibles are placed on a silica tray and loaded into a muffle furnace only large enough to contain the tray. Fusion takes 5 minutes from the time the preheated furnace returns to its normal 1000ºC after loading. The silica plate and graphite crucibles are then

removed from the oven and allowed to cool. Each bead is reground in the swing mill for 35 seconds, the glass powder then replaced in the graphite crucibles and refused for 5 minutes.

Following the second fusion, the cooled beads are labelled with an engraver, their lower flat surface is ground on 600 silicon carbide grit, finished briefly on a glass plate (600 grit with alcohol) to remove any metal from the grinding wheel, washed in an ultrasonic cleaner, rinsed in alcohol and wiped dry. The glass beads are then ready to be loaded into the XRF spectrometer. Preparation of a single bead takes, on average, 45 minutes.

A number of practical points in this process need emphasis. Hand picking of fresh chips after the use of steel hammers, hydraulic press, and steel jaw crusher should prevent significant iron, chromium or nickel contamination, which resides mainly i n the finer dust. It has long been recognized that tungsten carbide mills cause contamination with tungsten and cobalt and these elements are not analyzed. Niobium contamination has also been reported from tungsten carbide mills (Joron et al., 1980; Hicks on and Juras, 1986) and tests using pure vein quartz suggest that different mills cause variable degrees of Nb contamination, which is typically of the same order of magnitude (2%) as the precision of the method (one standard deviation 1.0 ppm). Tantalum contamination is apparent. Alumina ceramic mills can be substituted for tungsten carbide but are brittle and therefore costly and only achieve the fine and even-grained powder required over a much longer period. fine and even grinding is surprisingly important. coarse powders result in separation of mineral phases during fusion (even double fusion) and can be a cause of high totals.

Analytical Procedure

The concentrations of 27 elements in the unknown samples are measured by comparing the X-ray intensity for each element with the intensity for two beads each of nine USGS standard samples (PCC-1, BCR-1, BIR-1, DNC-1, W-2, AGV-1, GSP-1, G-2, and STM -1, using the values recommended by Govindaraju, 1994) and two beads of pure vein quartz used as blanks for all elements except Si. The 20 standard beads are run and used for recalibration approximately once every three weeks or after the analysis of about 300 unknowns. The intensities for all elements are corrected automatically for line interference and absorption effects due to all the other elements using the fundamental parameter method.

Precision

Two standard beads (BCR-P and GSP-1) are used as internal standards. Kept in the same position in the automatic loader, they are run between every 28 unknown samples and so provide a continuing check on instrumental performance. They also provide a measure of instrumental precision within a single run and between runs over much longer periods.

The other critical aspect of analytical precision is the ability to reproduce the same concentration values in many separate beads prepared from the same rock or mineral sample. The important factors here are the homogeneity of the original sample and the ability to make a homogeneous bead. Clearly, coarse grained rock samples need to be homogenized adequately before mixing with the tetraborate flux. Assuming that the sample powder is perfectly homogenous, then the analysis of multiple beads prepared from that powder should provide a realistic measure of the overall precision of the technique. A quick visual illustration of the variation in elemental concentrations between two beads made from the same powder is provided in the vertical discrepancies between each of the two beads made from the ten standard samples used to create the calibration curves.

In a laboratory dedicated to the analyses of up to one hundred samples a week, every week of the year, one of the most acute concerns is the possibility of mixing samples. This can occur at any stage, but in the preparation procedure used here the most obvious step in which samples may get mixed is the placing of the 20 samples in unmarkable carbon crucibles in the furnace for fusion. As a precaution against mixing at this stage the plate on which the samples are loaded is notched and

sample numbers recorded on a paper template. In addition, a second bead is made from one, randomly chosen, sample from each tray and reported as a "repeat" analysis. Such repeat beads also provide the user with an immediate measure of the precision of the analyses and whether small variations in the composition of two samples are analytically significant or not.

Accuracy

Unlike precision, a definitive measure of the accuracy of geologic samples is not possible. We can best estimate accuracy by comparing our results to the "given" values of standard (reference) samples, compiled from numerous analyses by different workers in different laboratories using a variety of techniques. Reliance on oxide totals approximating to 100% as a measure of accuracy is of limited value. While the use of totals as a test of accuracy was the only such check available to the classical wet chemical analyst, it should only be used in instrumental analysis as a rough guide to locate gross errors, as in the weighing of sample and flux. This is particularly true if, as in the methods outlined here, the volatile content and oxidation state of iron are ignored. The modern instrumental analyst has better methods of estimating accuracy. In the WSU GeoAnalytical Laboratory we estimate the accuracy of our analyses in two ways: First, by the scatter of the standard samples around the calibration curve for each element; and second, by comparing our values to those of the same samples analyzed by other workers in different laboratories and using different techniques.

(1) Accuracy estimated by use of standard samples:

By treating the ten calibration standards as unknowns and comparing the values so obtained to the "given" values (that is, other peoples' best estimates) we gain an immediate visual impression of accuracy. In essence this is the amount of scatter of any one sample from the calculated calibration curve drawn through all 20 analyzed standard beads. These results are quantified, where the observed WSU XRF values are compared to the best or "given" values compiled by Govindaraju (1994), normalized to 100% on a volatile-free basis.

For most major elements the variation between the two standard sample beads is of the same order as their variation from the given value, with the inference that imprecision resulting from the preparation of the beads (as recorded in the overall precision) is equal to or greater than inaccuracies caused by inadequate matrix and interference corrections. With the exception of Na, the total discrepancies from the "given" values are less than might reasonably be expected between two random samples collected in the field from the same rock unit - lava flow, igneous intrusion, etc. Hence, this degree of inaccuracy may be regarded as insignificant for most purposes of geologic correlations or petrogenetic modelling

Among the trace elements the precision, and therefore the accuracy, of Ni, Cr, SC, V, and Ba is significantly less than for Rb, Sr, Zr, Nb, Y, Ga, Cu, and Zn. This correlates in part with the lower count rates (cts/sec/ppm) for SC, V, and Ba using a Rh target. Ni, Cr, SC, V, and Ba are regarded as only semiquantitative below the 30 ppm level. Rb, Sr, Zr, Nb, Y, Pb, and Th have satisfactory precision and accuracy down to 1 to 3 ppm. La and Ce concentrations are qualitative only.

Precision and accuracy of SC, V, Ba, and Nb in particular, could be improved by changing the X-ray tube target and operating conditions, but only at a loss of some long term reproducibility for all elements. The WSU GeoAnalytical Laboratory has an ICP/MS facility which measures SC, Ba, Pb, Nb and La and Ce with the other rare earth elements much more accurately than XRF, so attempts to perfect the XRF system for these elements have not been pursued.

(2) Accuracy estimated from inter-laboratory comparisons:

Major and Minor Elements. For each element a comparison of analyses of the same powders by another laboratory has been attempted using, where possible, the most appropriate technique.

For major and minor elements other XRF laboratories have been used. Comparisons are available from Los Alamos, the USGS (Denver), Rhodes University (South Africa), and from XRAL (Canada). In addition, comparisons of Fe and Na data by INAA are available from Washington State University, Oregon State University, and the University of Oregon. Na data have also been compared to ICP data from London.

Of these various comparative data sets, that of 158 samples from the Cascade Range supplied by Dr. Dave Sherrod, USGS, (Sherrod, 1986) and run in Los Alamos have the widest concentration range. In general, the correlations are tight and within the limits set by the precision measurements. Slight biases between the WSU values and other XRF laboratories have been noted previously (Hooper et al., 1993) and are not yet fully understood. The WSU data sets appear to have consistently lower Fe (0.3% FeO) and higher Si (0.45% Si02) than other XRF laboratories. We suspect this reflects differences in the Fe measurements which are then reflected in Si02 by the normalization procedure used. However, no such bias is apparent between the WSU XRF data and WSU INAA data for Fe from WSU (185 Cascade Range samples (Conrey, 1991)), nor between WSU XRF and INAA data from Oregon State University (Hill, 1992). In all cases the biases are well within the natural variation between two samples from the most homogeneous flow from the Columbia Plateau and are therefore unlikely to prove significant in petrologic studies. The Na data, while less precise than that for other major elements, nevertheless compares well with the Los Alamos XRF data and with INAA (WSU) and ICP (London) data.

Trace Elements. Ni has been compared to XRF data from Rhodes University, South Africa (J. S. Marsh, 1993, unpublished data), XRAL, and six samples from the USGS-Menlo Park (Gardner, 1994). There is a fair scatter and the WSU data is consistently 10 to 15 ppm lower than the Rhodes values but similar or slightly higher than the USGS and XRAL values. The Rhodes data may not have been corrected for enhancement by Fe.

Cr XRF values from WSU have been compared to XRF values from the USGS, XRAL, and Rhodes University, and to INAA data from WSU and from Oregon State University (OSU). The correlation is fairly tight, but the WSU values appear lower, the discrepancy increasing at higher concentrations (>100 ppm).

Sc values have been compared to INAA values (WSU and OSU), ICP (London), and ICP/MS (WSU). INAA should provide excellent Sc. ICP and ICP/MS comparisons are less tight, indicating these techniques are somewhat less suitable for Sc analysis. The main problem with the WSU XRF data for Sc is the poor precision, a result of the low count rate caused by the combination of the Rh target and 50 kV/50 mA settings used.

Duplicate analyses for V are available by XRF from Rhodes University, by ICP (London, Texas Tech. U.). Precision is again relatively poor because of the set operating conditions, but no obvious bias is apparent.

Ba values are compared with ICP/MS (WSU) and ICP (King's College and Texas Tech. U.) values. There is no discernible bias over a large range in concentration, but again with a fair scatter due to relatively poor precision.

Rb and Sr values indicate both high precision and accuracy for these two elements. This is well illustrated by a large data set for samples from Greenland for which Dr. John Duke (University of Alberta, Edmonton) obtained duplicate analyses by isotope dilution (Duke, 1993). Correlation with ICP/MS values is almost as tight. The exceptionally close correlations demonstrated in these plots is particularly significant because it implies that the reproducibility of the sample preparation technique must be at least that good. And this, of course, is applicable to all other elements, so long as the original powder was homogeneous.

Duplicate Zr values are available by XRF (Rhodes University and U. S. G. S., Menlo Park) and by ICP (London). No bias is apparent but while very adequate, the scatter on these plots is slightly greater than expected, given a precision which is theoretically as high as that for Rb and Sr. The answer may lie in the dispersed nature of the principal Zr bearing phase, zircon; the powders may not be entirely homogeneous with respect to this phase and element.

Duplicate analyses for Y are available by XRF (USGS, Menlo Park, Rhodes University, and XRAL), by ICP (London) and by ICP/MS (WSU). The ICP/MS data correlates well with the WSU XRF data although the two separate runs differ in that in one case the XRF is slightly higher and in the other the XRF data is slightly lower than the ICP/MS data. It is virtually impossible for this type of variation to be due to the XRF in which the conditions are rigidly constant, so these differences are believed to reflect small differences between the two ICP/MS runs.

Nb values have been compared with XRF data (USGS, Menlo Park, XRAL, Rhodes University), ICP data (London), and ICP/MS data (WSU). The results are scattered, suggesting many laboratories have problems in obtaining good Nb values. The tightest correlations of the XRF data are with the ICP/MS values, but there is a slight bias which increases with concentration suggesting the XRF values are high. As for Y, this bias differs significantly between the two runs suggesting that at least a part of this problem lies with the ICP/MS values.

No comparative data is available for Ga and duplicate Cu analyses are only available from one XRF run (Rhodes University) which demonstrates adequate correlation. Duplicate values on Zn by XRF (USGS, Menlo Park and Rhodes University) and by ICP (London) are again somewhat scattered but the relatively good correlation with the ICP data, while implying a small bias between the two data sets, suggests the WSU XRF data are adequate. Clearly, more duplicate analyses are required for Ga, Cu, and Zn to provide a better estimate of the accuracy of the WSU XRF values.

XRF values for La and Ce are only quoted by the WSU GeoAnalytical Laboratory because of special requests. They demonstrate poor precision and are regarded as qualitative only.

Recent XRF runs have been expanded to include Pb and Th. Adequate comparisons are only available from the ICP/MS (WSU). The Pb and Th values show adequate correlation and suggest the limiting factor in the accuracy of the values for both elements is the precision of the XRF data.

Summarizing, it is apparent that for the 17 trace elements analyzed on the WSU XRF system, the accuracy imposed is that of the precision, the limits of which are noted earlier. Small biases may be present in some cases (e. g. Cr, N b) but few are significant, and none appear critical. The precision limits are, however, important. These comparative plots serve to remind us of the high reproducibility of XRF analyses in general but also that the XRF technique loses precision at low concentrations (below 10 ppm and, for some elements, below 30 ppm). At these lower concentrations other techniques, isotope dilution and ICP/MS in particular, are preferable.

Stable Operating Conditions

The GeoAnalytical Laboratory uses only a Rhodium target which is run at 50 kV and 50 mA with full vacuum and a 25 mm mask for all elements and all samples. The advantages for retaining the same conditions for all elements, in addition to efficiency, is the greater stability and consequent ability to reproduce the same intensities for the same sample over long periods of time. This can be demonstrated for this laboratory over a 10-year period. In addition, the 2:1 tetraborate beads can be stored for a demonstrable 30 years without significant deterioration and can be re-run if and when the basic equipment, standards, or running conditions are modified. This level of precision has been critical to the tracing of the subtle differences between the many flows sampled from the Columbia Plateau over that period.

The disadvantages of using such constant operating conditions are loss of precision and accuracy for some elements, notably Sc, V, Nb and Ba, for which these conditions are not ideal.

Oxidation State and Volatile Content – LOI

The WSU GeoAnalytical Laboratory normally ignores the oxidation state of iron in whole rock samples, quoting all the iron as FeO and normalizing to 100% without measuring the volatile content. LOI and oxidation state are measured only for particular purposes or on special request.

In general, we regard the volatile content and oxidation state of igneous rocks as a distraction for most petrogenetic work. Both are products of post eruptive processes (alteration) in large part and serve to distort the composition immediately prior to eruption which is our principal concern. When data on the volatile content and oxidation state are lacking, it follows that original totals can be used only as a rough check for major errors in weighing, smaller variations in the totals will reflect variable oxidation states and volatile contents. The use of normalized values has caused some concern amongst our colleagues, especially those introduced to geochemistry through wet chemical analysis in which the total, including volatile content, was the obvious check on the accuracy of the analysis. As discussed above, there are now much better ways of measuring precision and estimating accuracy. Incorporation of oxidation states and volatile content so distort analyses of Columbia River basalt, to us e but one example, that their use on the Columbia Plateau significantly reduces our ability to correlate flows. Had this approach been adopted our present knowledge of Columbia River basalt flow stratigraphy would be much less precise.

Two other factors are involved. The analysis of volatiles and the oxidation state of iron tends to be labor-intensive, creating an unjustified cost except in particular circumstances. Both, of course, are independent of the X-ray analysis and can be added or discarded any time, so long as the totals are not relied upon as a measure of accuracy for the whole analysis. Finally, this laboratory would argue that in analytical comparisons inclusion of the oxidation state of iron and the volatile content distorts the results and makes the comparisons of little value (Govindaraju, 1994). To determine genuine bias and analytical differences between laboratories it is essential to calculate the iron in a single oxidation state, eliminate the volatile (LOI) content, and normalize to 100. This is because the methods of measuring the LOI are so variable that differences in these values between laboratories distort the abundances of all other elements (again, see Govindaraju, 1994).

Conclusions

We argue that the single low-dilution fusion technique is superior to the more traditional high dilution fusion and pressed powder technique in its much greater efficiency which is achieved without measurable loss of either precision or accuracy.

There are advantages and disadvantages in using stable operating conditions, in which neither the target nor the voltage are changed between elements. The adoption of such a procedure is likely to depend on the specific aims of any one research program. Finally, the measurement of the oxidation state of iron and the volatile content should not be used to distort otherwise excellent XRF analyses.

Bibliography

References

Conrey, R. M., 1991, Ph. D. dissertation, Washington State University, Pullman.

Duke, M. J. M., 1993, Ph. D. dissertation, University of Alberta, Edmonton.

Gardner, C. A., 1994, U. S. Geological Survey Open-file Report 94-261, 100 p.

Govindaraju, K., 1994, Geostandards Newsletter, vol. 18, Special Issue, p. 1-158.

Hickson, C. J. and Juras, S. J., 1986, Canadian Mineralogist, vol. 24, p. 585-589.

Hill, B. E., 1992, Ph. D. dissertation, Oregon State University, Corvallis.

Hooper, P. R., 1964, Analytical Chemistry, vol. 36, p 127.

Hooper, P. R., Johnson, D. M. and Conrey, R. M., 1993, Washington State University, Department of Geology, open-file report.

Joron, J. L., Briqueu, L., Bougalt, H., and Treuil, M., 1980, Initial Reports of the Deep Sea Drilling Project, vol. LIV, U. S. Gov't., Washington, D. C., p. 725-727.

Madin, I., 1994, State of Oregon Dept. of Geology and Mineral Industries Geological Map Series GMS-60 with accompanying text and table of chemical data.

Norrish, K. and Hutton, J. T., 1969: Geochim Cosmochim Acta 33, 431.

Sherrod, D. R., 1986, Ph. D. dissertation, Santa Barbara, 320 pp.

Trace Element Analyses of Rocks and Minerals by ICP-MS

Introduction

Inductively coupled plasma-mass spectrometry (ICP-MS) is well established as a rapid and precise method for the determination of the rare earth elements (REEs) and trace elements in geologic samples – Lichte et al., (1987), Jarvis (1988), Longerich et al., (1990). However, complete sample digestion is required for accurate results. Mixed acid open-vial digestions on a hotplate work well for basaltic and most ultramafic samples, but may fail to completely decompose many trace mineral phases found in more silicic samples. These resistant phases, such as zircon, garnet, and tourmaline, may contain a significant percentage of the total trace elements in a given sample. High-pressure bombs are effective at achieving complete digestion, but are cumbersome, slow, and labor intensive. Fusion with a flux may require large dilutions to avoid unacceptably high levels of total dissolved solids. We have developed a combination fusion-dissolution method that effectively decomposes refractory mineral phases and removes the bulk of unwanted matrix elements. The procedure consists of a low-dilution fusion with di-Lithium tetraborate followed by an open-vial mixed acid digestion. This method allows us to analyze 14 REEs and 13 additional trace elements in a wide range of geologic samples without having to make assumptions as to the presence or absence of resistant mineral phases. The dissolution with HF after the Lithium-tetraborate fusion quantitatively removes silica and more than 90% of the flux as gaseous fluorides, leaving clear, stable solutions for analysis on the ICP-MS.

Experimental

The Flux used for the fusion is di-Lithium-tetraborate (Spectromelt® A-10, EM Science, Gibbstown, NJ). Reagents are HNO3 69-70% (Fisher ACS plus grade), HF 48-52% (Baker ACS reagent grade), HClO4 67-71% (Fisher Trace Metal Grade), and H2O2 (Baker ACS Reagent). The HF is further purified before use by sub-boiling distillation in a teflon still. All water used is >18 M deionized water from a Nanopure analytical grade water system (Barnstead/Thermolyne).

Powdered samples are mixed with an equal amount of lithium tetraborate flux (typically 2g), placed in a carbon crucible and fused at 1000° C in a muffle furnace for 30 minutes. After cooling, the resultant fusion bead is briefly ground in a carbon-steel ring mill and a 250 mg portion is weighed into a 30 ml, screw-top Teflon PFA vial for dissolution. The acid dissolution consists of a first evaporation with HNO3 (2ml), HF (6 ml), and HClO4 (2 ml) at 110° C. After evaporating to dryness, the sample is wetted and the sides of the vial are rinsed with a small amount of water before a second evaporation with HClO4 (2 ml) at 160° C. After the second evaporation, samples are brought into solution by adding approximately 10 ml of water, 3 ml HNO3, 5 drops H2O2, 2 drops of HF and warmed on a hot plate until a clear solution is obtained. The sample is then transferred to a clean 60 ml HDPE bottle diluted up to a final weight of 60g with de-ionized water.

Solutions are analyzed on an Agilent model 4500 ICP-MS and are diluted an additional 10X at the time of analysis using Agilent's Integrated Sample Introduction System (ISIS). This yields a final dilution factor of 1:4800 relative to the amount of sample fused. Instrumental drift is corrected using Ru, In, and Re as internal standards. Internal standardization for the REEs uses a linear interpolation between In and Re after Doherty (1989) to compensate for mass-dependant differences in the rate and degree of instrumental drift. Isobaric interference of light rare earth oxides on the mid- heavy REEs can be a significant source of error in ICP-MS analysis, so tuning is optimized to keep the CeO/Ce ratio below 0.5%. Correction factors used to compensate for the remaining oxide interferences are estimated using two mixed-element solutions. The first contains Ba, Pr, and Nd, and the second Tb, Sm, Eu, and Gd. Standardization is accomplished by processing duplicates of

three in-house rock standards interspersed within each batch of 18 unknowns. Concentrations, oxide- and drift corrections are then calculated offline using a spreadsheet.

Results

Long term precision for the method is typically better than 5% (RSD) for the REEs and 10% for the remaining trace elements. Analyses of USGS and international rock standards show good agreement with consensus values.

Bibliography

Doherty W. (1989), An internal standardization procedure for the determination of yttrium and the rare earth elements in geological materials by inductively coupled plasma-mass spectrometry. Spectrochimica Acta, 44B, 263-280.

Jarvis, K.E. (1988), Inductively coupled plasma mass spectrometry; a new technique for the rapid or ultra-trace level determination of the rare-earth elements in geological materials. Chemical Geology, 68, 31-39.

Jenner G.A., Longerich H.P., Jackson S.E., and Fryer B.J. (1990), ICP-MS – A powerful tool for high-precision trace-element analysis in Earth sciences: Evidence from analysis of selectd U.S.G.S. reference samples. Chemical Geology, 83, 133-148.

Lichte, F.E., Meier, A.L., and Crock, J.G. (1987), Determination of the rare-earth elements in geological materials by inductively coupled plasma mass spectrometry. Analytical Chemistry, 59, 1150-1157.

Longerich H. P., Jenner G.A., Fryer B.J., and Jackson S.E. (1990), Inductively coupled plasma-mass spectrometric analysis of geological samples: A critical evaluation based on case studies. Chemical Geology, 83, 105-118.

SM2. Zircon U-Pb geochronology and trace element data

This supplementary material is in a spreadsheet.

SM3. Supplementary figures

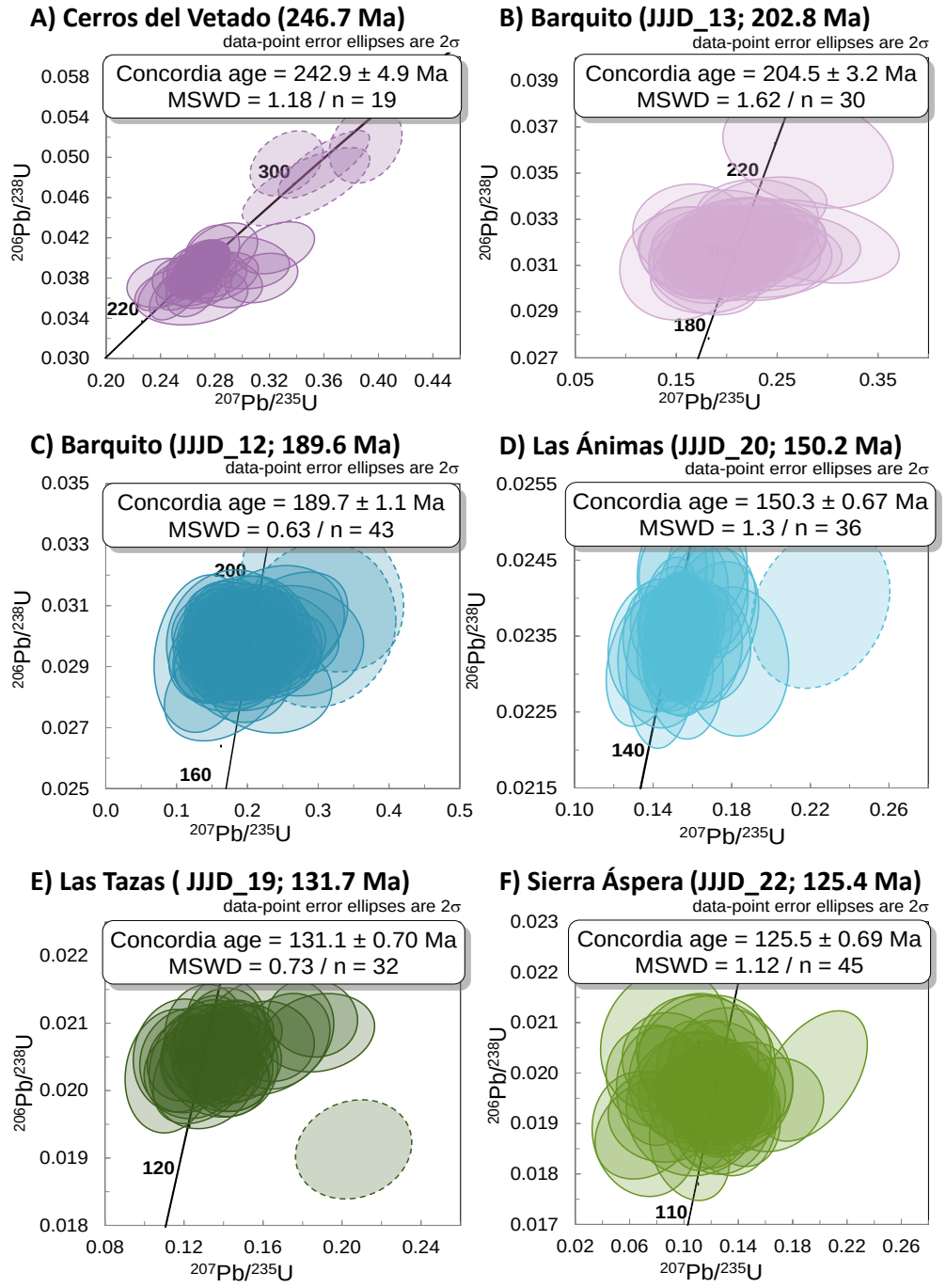

Figure SM3.1. U-Pb concordia age plots for selected intrusive samples from the Chañaral transect.

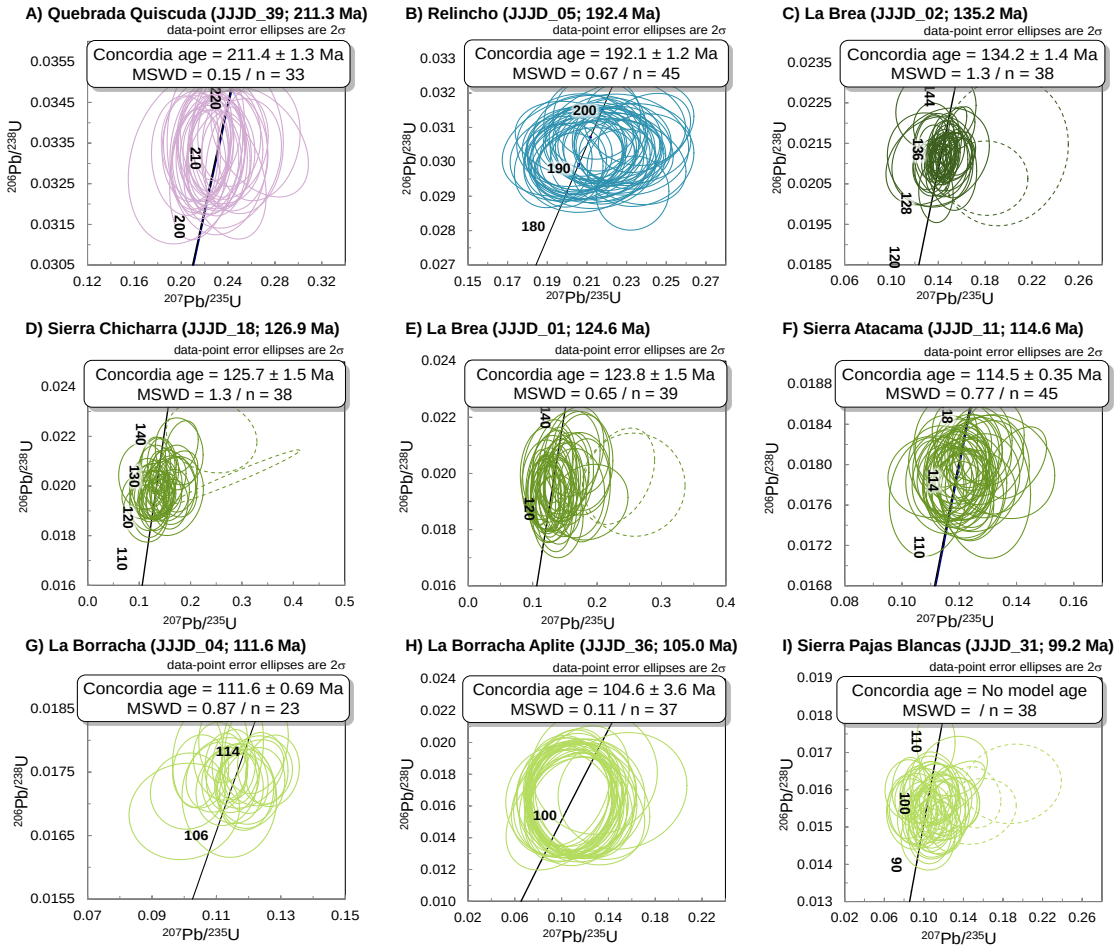

Figure SM3.2. U-Pb concordia age plots for selected intrusive samples from the study area.

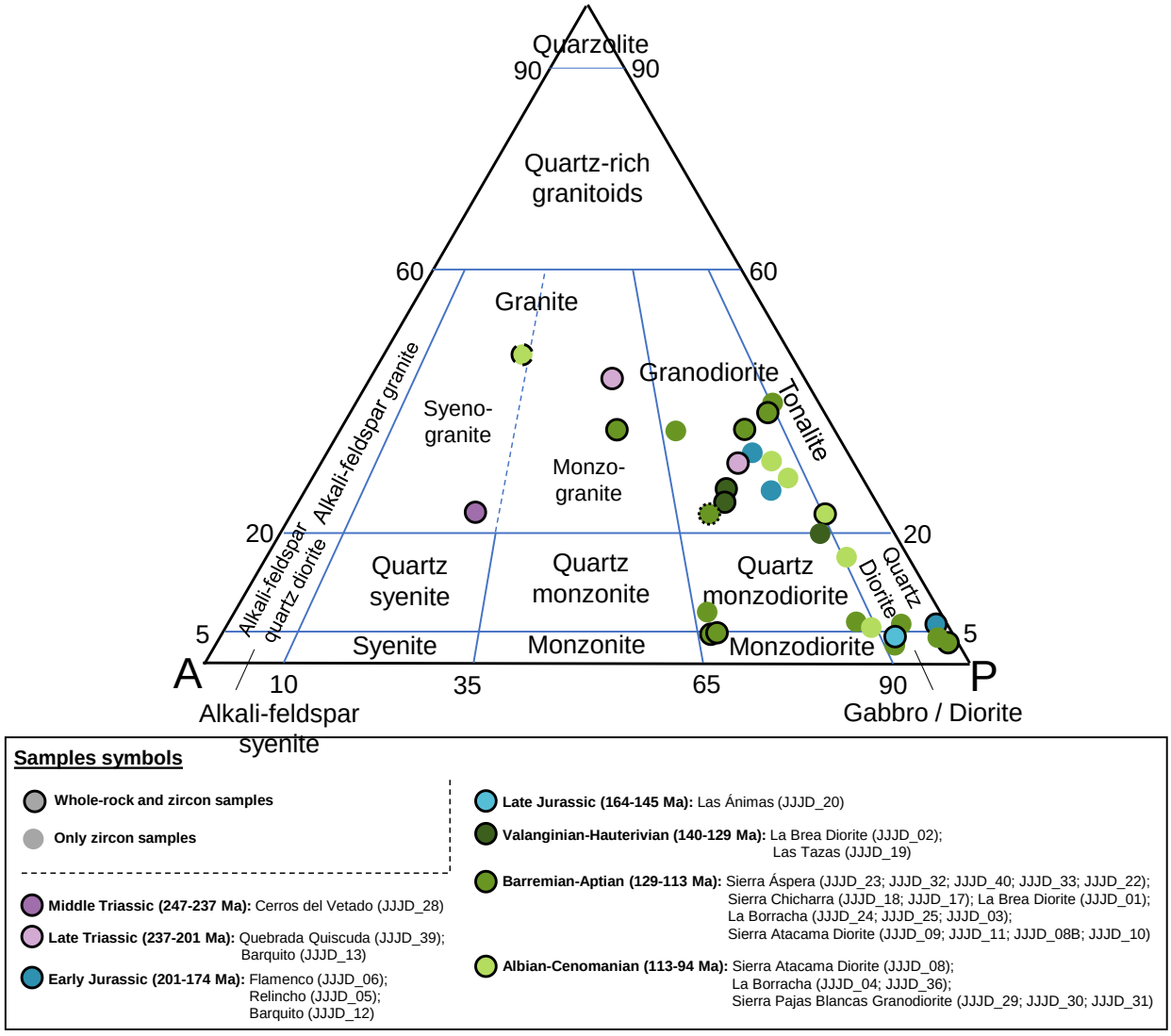

Figure SM3.3. QAP classification diagram of Streckeisen (1974).

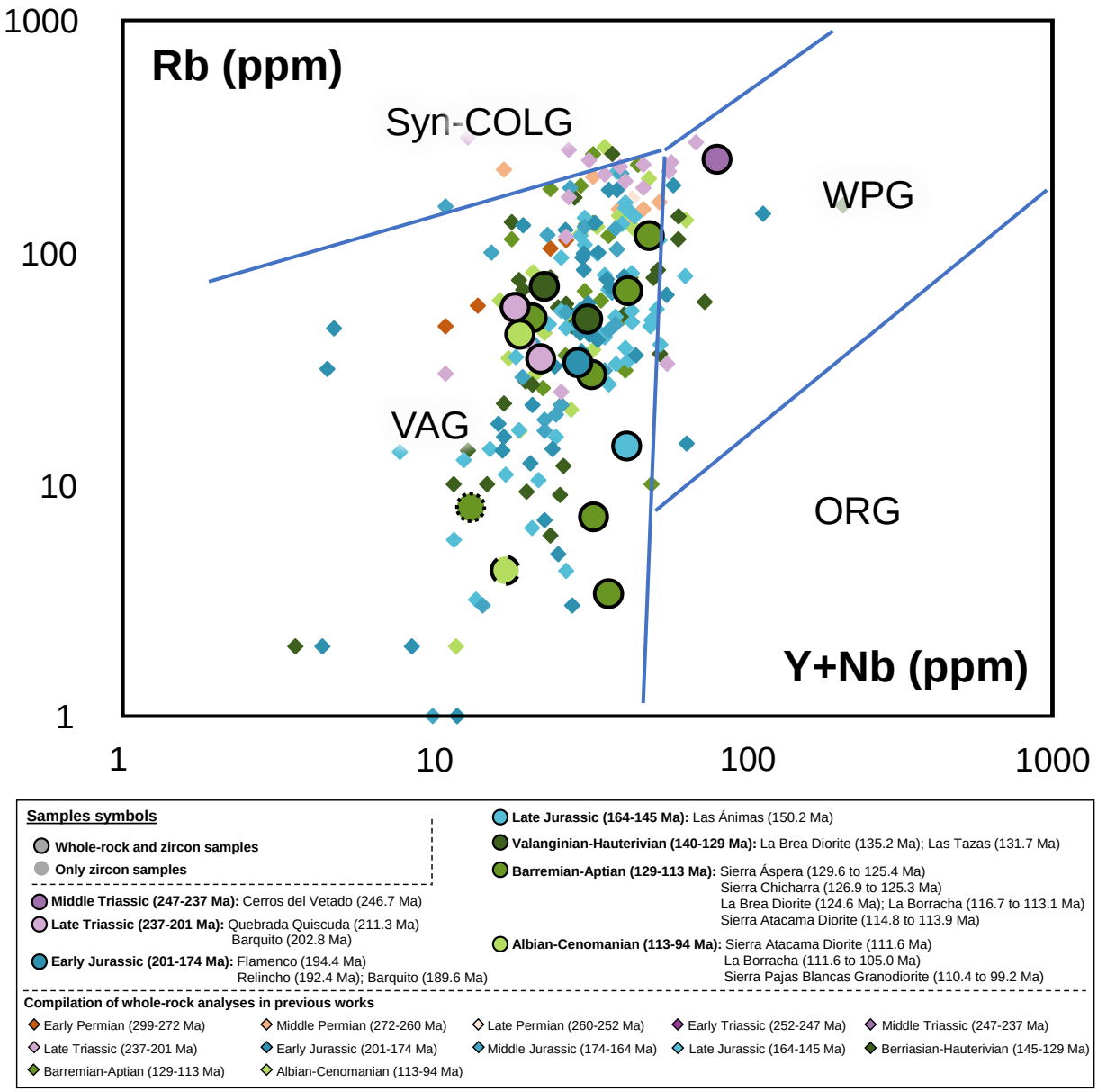

Figure SM3.4. Y+Nb vs Rb tectonic discrimination diagram of Pearce et al. (1984).

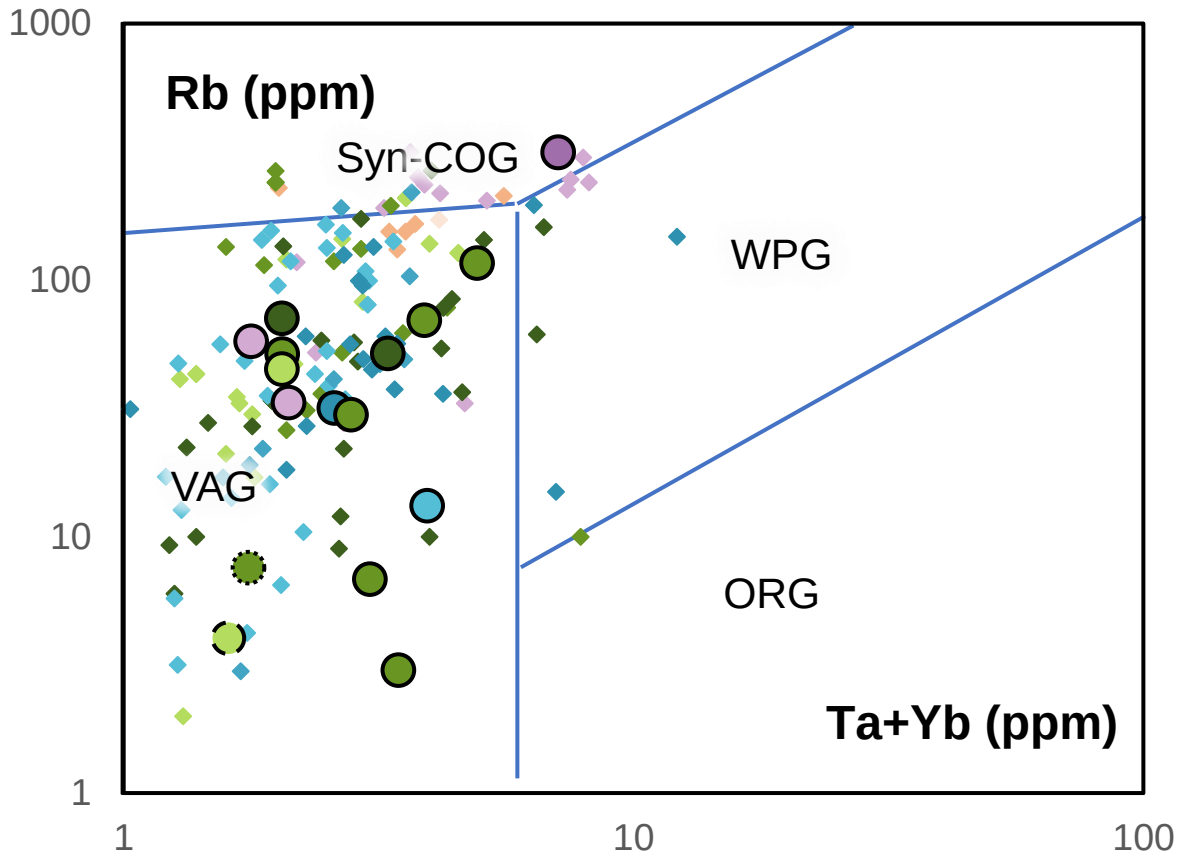

Figure SM3.5. Ta+Yb vs Rb tectonic discrimination diagram of Pearce et al. (1984). Symbols are as in Figure SM3.4.

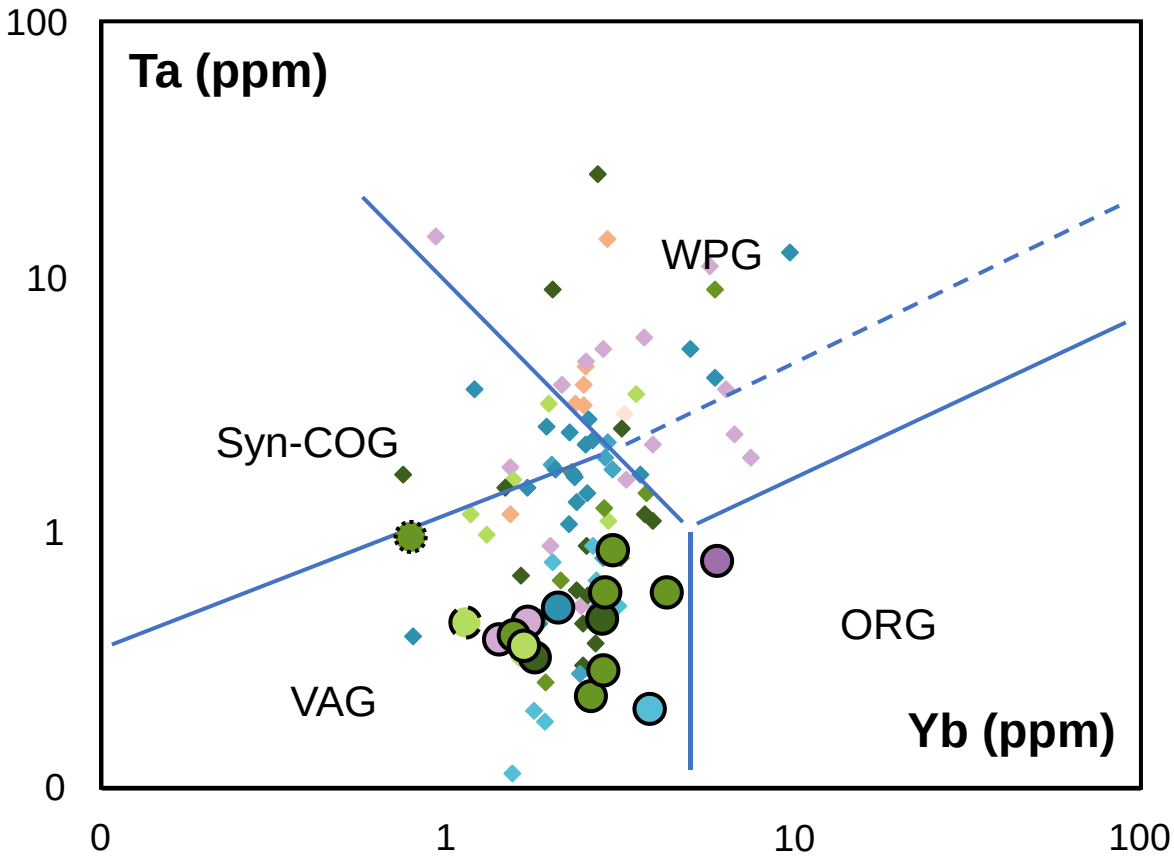

Figure SM3.6. Yb vs Ta tectonic discrimination diagram of Pearce et al. (1984). Symbols are as in Figure SM3.4.

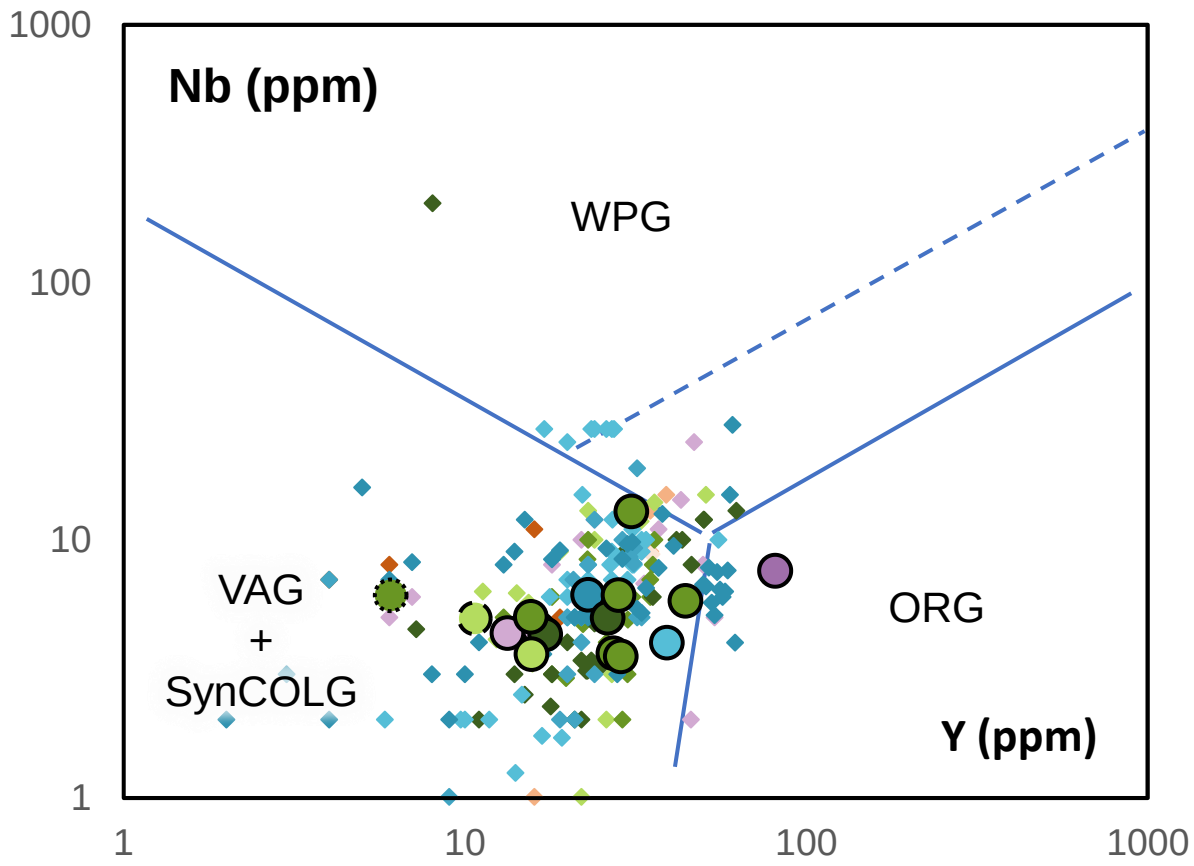

Figure SM3.7. Y vs Nb tectonic discrimination diagram of Pearce et al. (1984). Symbols are as in Figure SM3.4.

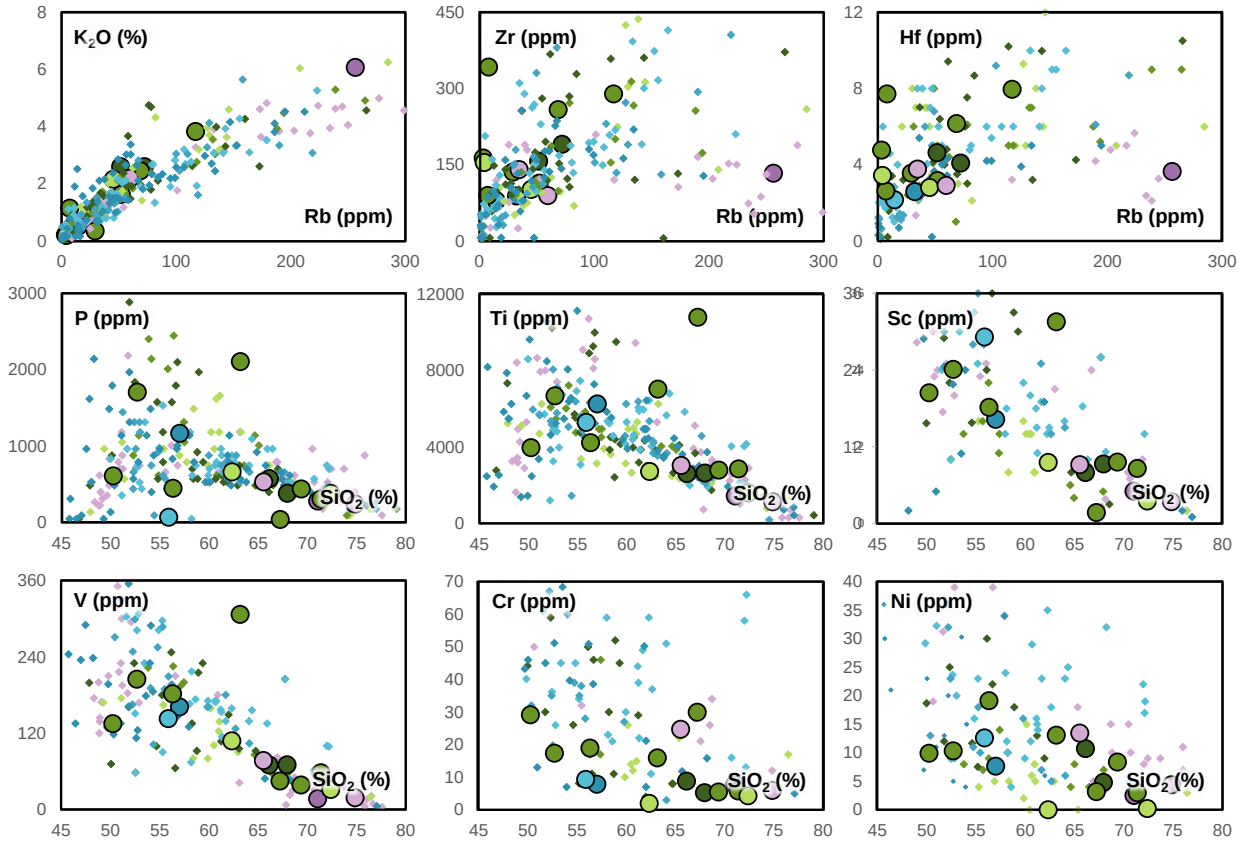

Figure SM3.8. Bivariate plots for studied plutonic complexes. Symbols are as in Figure SM3.4.

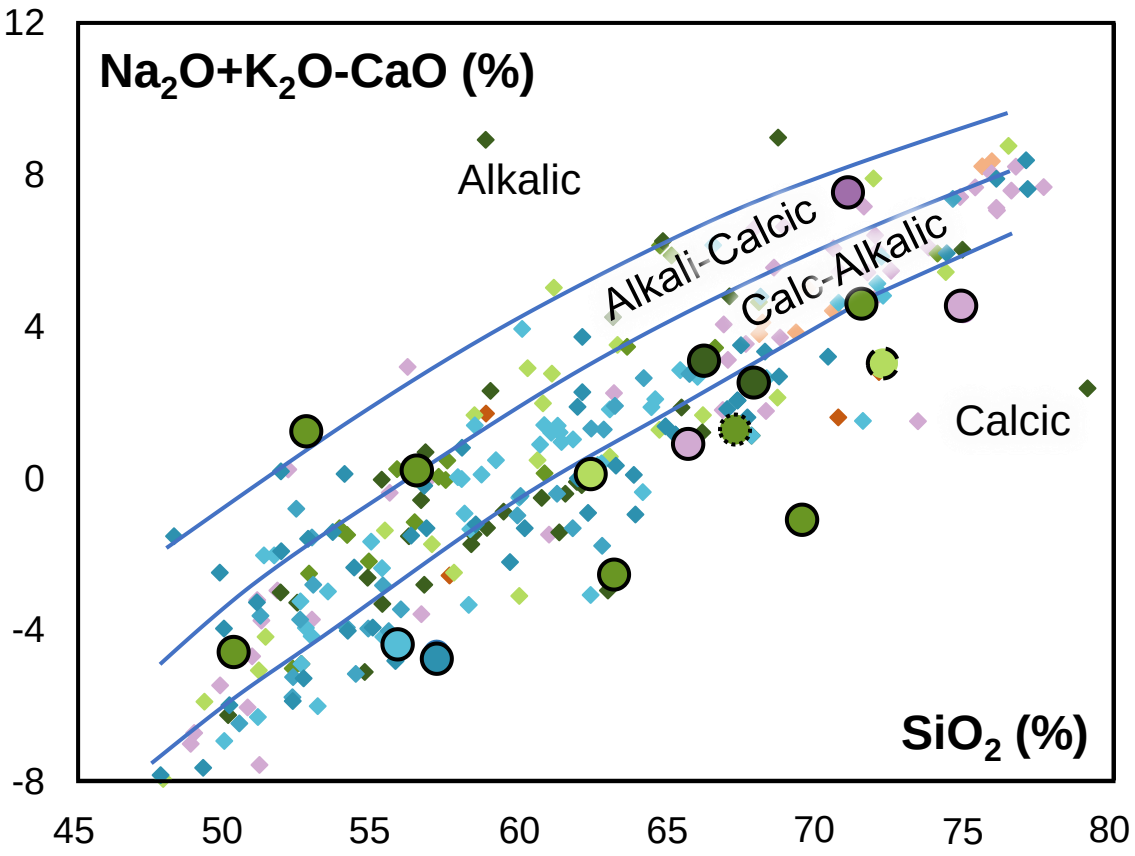

Figure SM3.9. Modified alkali-lime index (MALI) diagram used to distinguish between calc-alkalic/calcic and more alkalic complexes (after Frost et al., 2001). Symbols are as in Figure SM3.4.

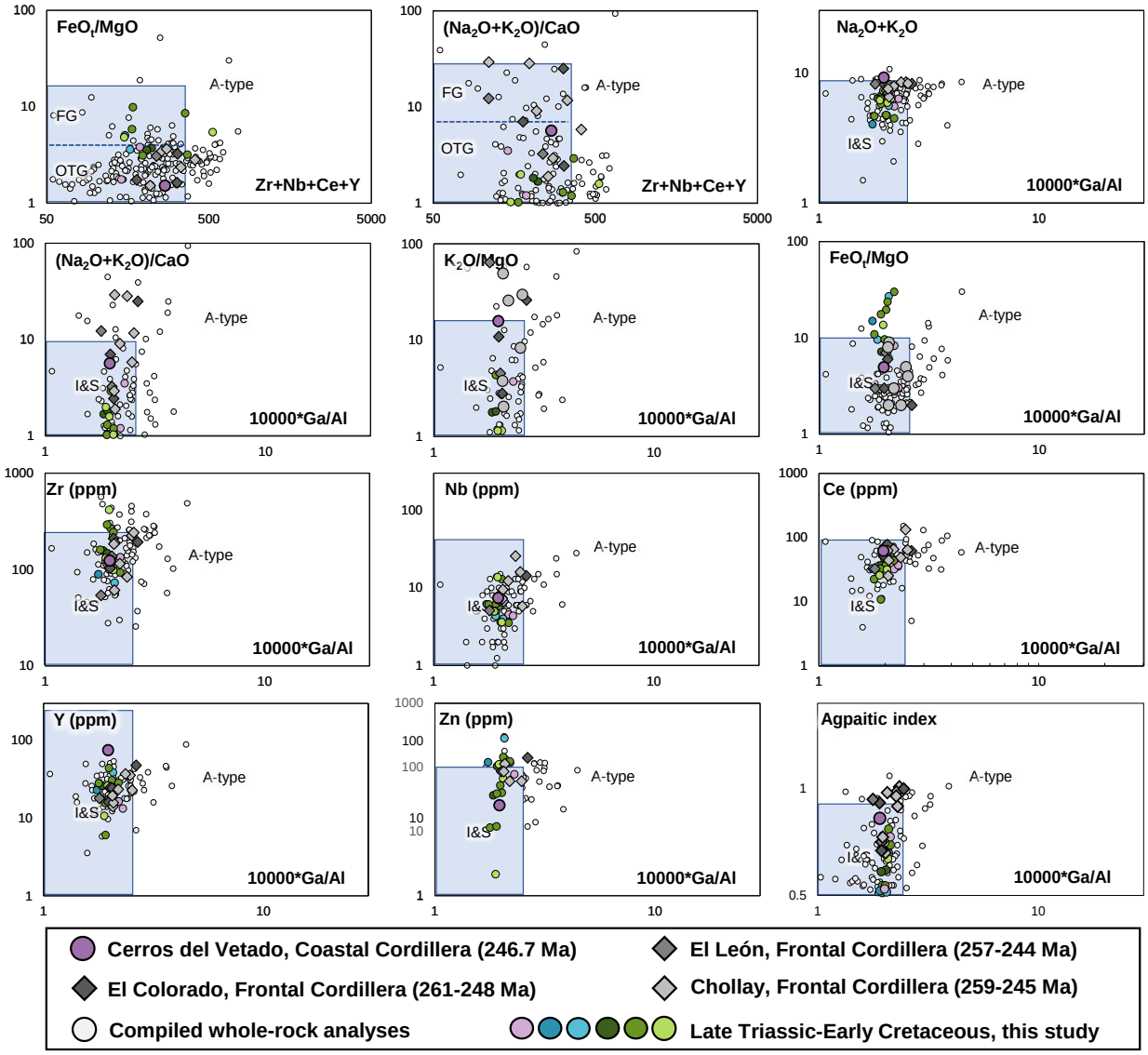

Figure SM3.10. I&S and A-type granitoids classification diagram (after Whalen et al., 1987). Symbols are as in Figure 10 of the main text.

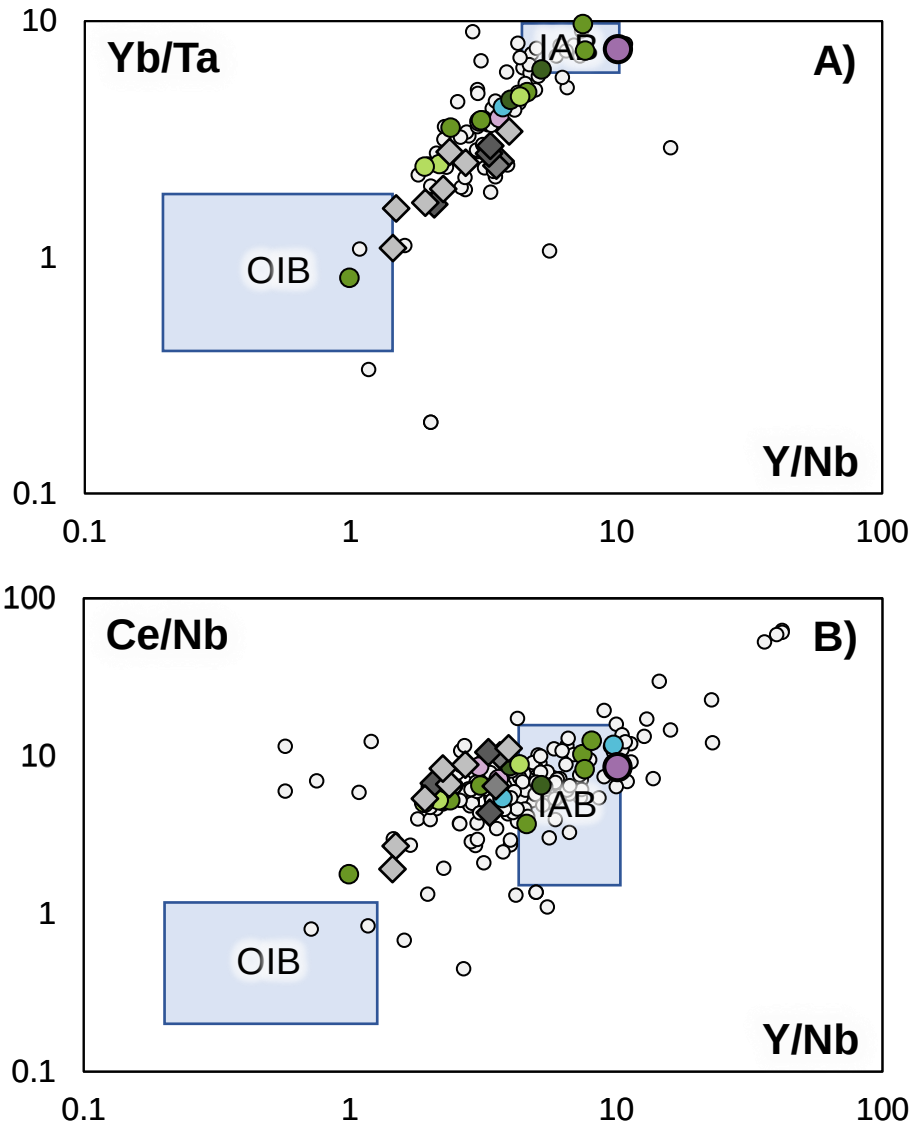

Figure SM3.11. Y/Nb vs Yb/Ta (A) and Ce/Nb (B) plots to discriminate A1- and A2-type granitoids (after Eby, 1992). Symbols are as in Figure SM3.10.

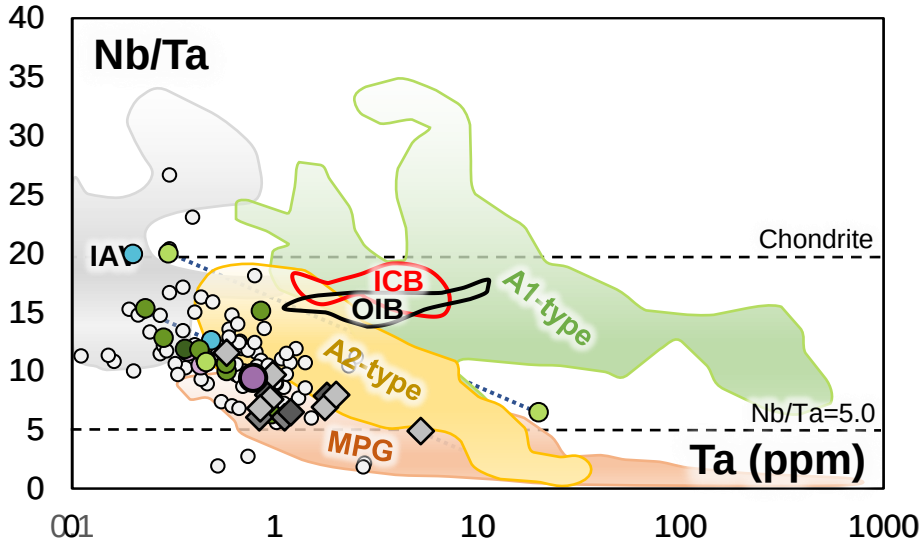

Figure SM3.12. Ta vs Nb/Ta diagram showing the composition for muscovite peraluminous (MPG) and A-type granitoids (Ballouard et al., 2020). Symbols are as in Figure SM3.10.

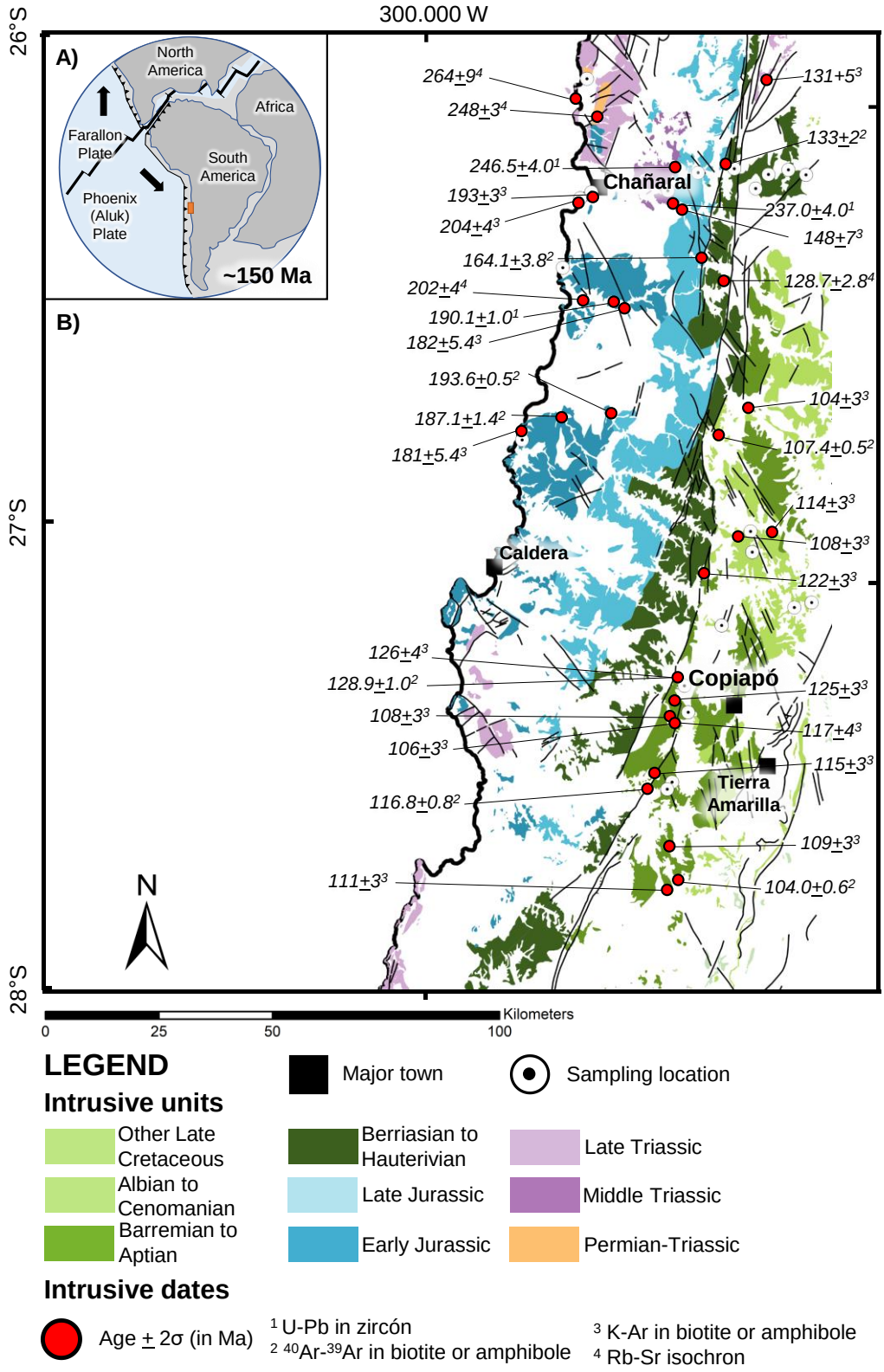

Figure SM3.13. Distribution of plutonic complexes in the study area (Modified after Vivallo et al., 2008 and Sernageomin, 2002). Previously published radiometric ages are

indicated. Data source: Vivallo et al. (2008), Arévalo (2005a,b), Blanco et al. (2003), Godoy and Lara (1999; 1998) and Sernageomin (2002).

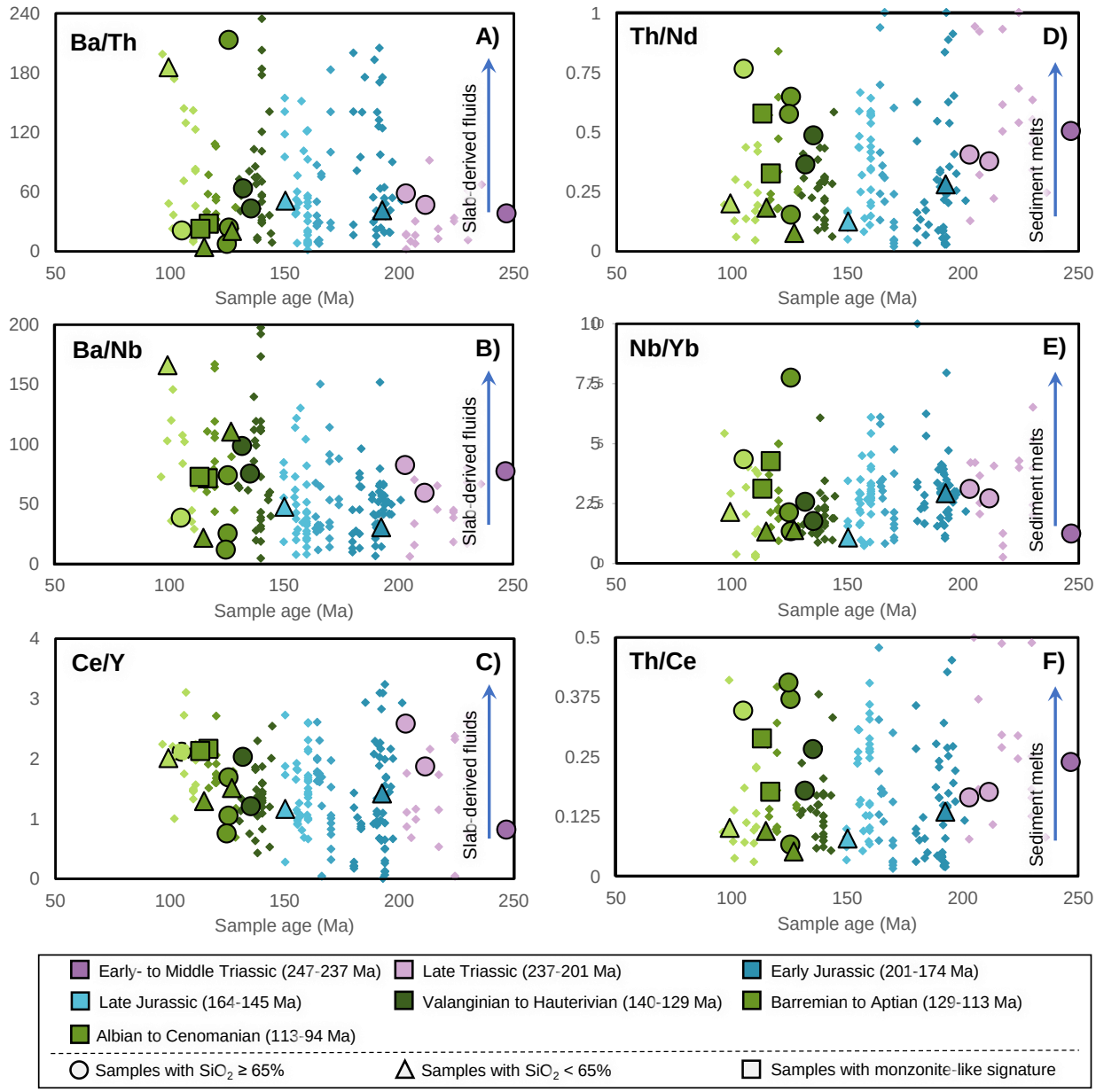

Figure SM3.14. Rock ages vs elemental ratios showing slab-derived fluids (A-C) and sediment melts contributions (D-F) to the magmatic source of the studied plutonic complexes. Symbols are as in Figure 13 of the main text.

SM4. Compiled dataset of whole-rock analyses for intrusive rocks from the Coastal Cordillera of Chile

This supplementary material is in a spreadsheet.

SM5. Compiled whole-rock analyses for El León, El Colorado and Chollay plutonic units

This supplementary material is in a spreadsheet.

SM6. Compiled dataset of radiometric ages for intrusive rocks from the study area

This supplementary material is in a spreadsheet.

A.2. SUPPLEMENTARY MATERIAL FOR CHAPTER 3

SM1. Samples and studied plutonic complexes

Sampling was carried out in a transect north of the Huasco valley (~28°15'S) and along the range between 28°30'and 30°S. Fifteen whole-rock and 21 zircon geochronology and trace element determinations were performed in samples obtained from 10 different plutonic complexes. Petrologic descriptions of the studied plutonic complexes and analyzed samples are in tables 1 and 2.

Main mineralogical components of the samples are plagioclase, hornblende and quartz (Table 2). Biotite could be present as a minor phase and pyroxene is usually replaced by hornblende. Magnetite and titanite are common accessory minerals. No evidence of deformation is observed. Alteration is minor and only represented by selective replacement of mafic minerals by chlorite, actinolite and/or epidote; and scarce albitization or sericitization of plagioclase could be also observed in some samples.

In terms of the zircon crystals obtained from the mineral separation procedure, most of them are inclusion-free, transparent and prismatic, with sizes ranging from 50 to 500 μm and a length to width ratio between 1.0 and 5.0. Cathodoluminescence (CL) images commonly reveal oscillatory zoning across the rims with homogeneous cores.

Analytical procedures

Whole-rock analysis. Determination of whole-rock major, minor and trace element concentrations were performed at the GeoAnalytical Laboratory, Washington State University, USA. Clean, unaltered rock chips (100 to 300 g) were ground in an agate mill. Concentrations of major and minor elements were determined by X-ray fluorescence with a single low dilution in a lithium tetraborate fused bead (Johnson et al., 1999). Trace

elements were determined using ICP-MS with a di-lithium tetraborate low-dilution fusion followed by an open-vial mixed acid digestion (Yu et al., 2009).

Simultaneous zircon U-Pb geochronology and trace element analysis. Five to 10 kg of sample were processed for zircon mineral separation by conventional comminution, magnetic and gravity procedures at the Department of Geology, University of Chile. Approximately 100 zircon grains per sample were handpicked and mounted in epoxy resin. Plešovice (Sláma et al., 2008) or SL2 (Gehrels et al., 2008) reference materials were used as a primary standard and SL2 or 91500 (Wiedenbeck et al., 1995) as a secondary standard for geochronology purposes; USGS NIST 610 was used as a primary standard for trace element measurements. Polished mounts were analysis at the CEGA Mass Spectrometry Laboratory, University of Chile. Zircon crystal images (CL) were obtained by using a FEI Quanta 250 scanning electron microscope (SEM) coupled with a Centaurus sensor. Images were used to assess their internal structure. Simultaneous U-Pb geochronology and trace element concentrations were determined by laser ablation, inductively coupled plasma mass spectrometry (LA-ICP-MS). Analyses were carried using an Analyte G2 193 nm ArF excimer laser ablation system coupled to an iCAP-Q ICP-MS. Detailed analytical procedures and data reduction are described in Liu et al. (2010) and are briefly summarized here. Spot analyses (50 μm) were performed on the rims of the zircon grains to run coupled U-Pb dating and trace element analyses. Each analysis considered 20 s followed by 50 s of data acquisition. The time-dependent drifts of U-Pb isotopic ratios and trace elements concentrations were corrected using a linear or exponential interpolation for every 5 and every 15 analyses, respectively. The reproducibility of the U-Pb geochronology was evaluated by comparison with the secondary reference material (Wiedenbeck et al., 1995). Off-line selection and integration of signals, time-drift corrections and quantitative

calibrations were performed using Iolite (Paton et al., 2011). Concordia diagrams and weighted mean calculations were constructed using Isoplot 4.0 (Ludwig, 2010). Uncertainties of individual analyses are quoted at the 2σ confidence level and include measured and propagated errors.

Bibliography (supplementary material)

Arévalo, C., Creixell, C., 2009. Geología del cuadrángulo Tres Cruces, Región de Coquimbo. Servicio Nacional de Geología y Minería: Santiago.

Arévalo, C., Mourgues, F.A., Chávez, R., 2009. Geología del área Vallenar-Domeyko, Región de Atacama. Servicio Nacional de Geología y Minería: Santiago.

Arévalo, C., Welkner, D., 2008. Geología del área Carrizal Bajo-Chacritas, Región de Atacama. Servicio Nacional de Geología y Minería: Santiago.

Arredondo, C., Moscoso, R., Prieto, X., Ortega, R., Carrasco, R., Vivallo, W., Mateo, L., Pantoja, G., Ulloa, M., Ercilla, O., Ridelle, E., 2017. Depósitos minerales de la Región de Coquimbo. Servicio Nacional de Geología y Minería: Santiago.

Creixell, C., Arévalo, C., 2009. Geología del cuadrángulo El Tofo, Región de Coquimbo. Servicio Nacional de Geología y Minería: Santiago.

Emparan, C., Pineda, G., 2000. Área La Serena-La Higuera, Región de Coquimbo. Servicio Nacional de Geología y Minería: Santiago.

Gehrels, G.E., Valencia, V., and Ruiz, J., 2008, Enhanced precision, accuracy, efficiency, and spatial resolution of U-Pb ages by laser ablation-multicollector-inductively coupled plasma-mass spectrometry: Geochemistry Geophysics Geosystems 9, Q03017.

Johnson, D.M., Hooper P.R., Conrey, R.M., 1999. XRF analysis of rocks and minerals for major and trace elements on a single low dilution Li-tetraborate fused bead. Advances in X-ray Analysis 41, 843-867.

Liu, Y., Hu, Z., Zong, K., Gao, C., Gao, S., Xu, J., Chen, H., 2010. Reappraisement and refinement of zircon U-Pb isotope and trace element analyses by LA-ICP-MS. Chinese Science Bulletin 55 (15), 1535-1546.

Ludwig, K., 2010. Isoplot/Ex version 4.1, a geochronological toolkit for Microsoft Excel. Berkeley Geochronology Center, Special Publication 4.

Paton, C., Hellstrom, J., Paul, B., Woodhead, J., Hergt, J., 2011. Iolite: Freeware for the visualization and processing of mass spectrometric data. Journal of Analytical Atomic Spectrometry 26, 2508-2518.

Sláma, J., Košler, J., Condon, D.J., Crowley, J.L., Gerdes, A., Hanchar, J.M., Whitehouse, M.J., 2008. Plešovice zircon - a new natural reference material for U-Pb and Hf isotopic microanalysis. Chemical Geology 249, 1-35.

Vivallo, W., Díaz, A., Jorquera, R., 2008. Yacimientos metalíferos de la Región de Atacama. Servicio Nacional de Geología y Minería: Santiago.

Welkner, D., Arévalo, C., Godoy, E., 2006. Geología del área Freirina-El Morado, Región de Atacama. Servicio Nacional de Geología y Minería: Santiago.

Wiedenbeck, M., Allé, P., Corfu, F., Griffin, W.L., Meier, M., Oberli, F., Quadt, A.V., Roddick, J.C., Spiegel, W., 1995. Three natural zircon standards for U-Th-Pb, Lu-Hf, trace element and REE analyses. Geostandards Newsletter 19 (1), 1-23.

Yu, Z., Robinson, P., McGoldrich, P.J., 2009. An evaluation of methods for the chemical decomposition of geological materials for trace element determination using ICP-MS. Geostandards and Geoanalytical Research 25, 199-217.

Figure legends

Supplementary Figure 1. Sr/Y, to estimate crustal thickness (ref. 32).

Supplementary Table 1. Geographic location, age and main characteristics of the studied plutonic complexes

Plutonic Complex	UTM Location		General description	Main rock types	Reported age (Ma)	References
	N	E				
Carrizal Bajo	6895000	295000	Group of tabular plutonic bodies that are in contact with the Chañaral Epimetamorphic complex and the Algodones granite	Mg, Gdt (Bt + Amp) Dt, Dqz (Px + Amp + Bt)	208-206	Arévalo and Welkner (2008) Welkner et al. (2006)
Algodones Granite	6895000	305000	Ellipsoidal, NE oriented pluton that is in contact with the Chañaral Epimetamorphic complex and Carrizal Bajo plutonic complex to the west	Mg, Gdt (Amp + Bt) Dqz (Amp + Bt)	203-197	Arévalo and Welkner (2008)
Capote Granodiorite	6860000	304000	Tabular and elongated, NE oriented homogeneous pluton that intrudes the Chañaral Epimetamorphic complex and Canto del Agua Fm. to the west and the La Negra Fm. to the east	Gdt (Bt + Amp) Md, Dt (Bt + Amp $\pm$ Px)	190-183	Arévalo and Welkner (2008)
Dioritic intrusions, north of La Serena city	6715000	278000	A group of irregular bodies that outcrop in the coast north of La Serena city in a belt of 55 km. Intrude the Agua Salada Fm.	Mdqz, Dqz (Bt + Amp + Px) Md, Dt (Bt + Amp $\pm$ Px)	145	Emparán and Pineda (2000)
San Antonio Diorite	6890000	315000	Ellipsoidal, NNE oriented homogeneous pluton that is in contact with the Chañaral Epimetamorphic complex to the west, Canto del Agua to the south, and La Negra Fm. to the east	Dt (Px + Amp)	152-149	Arévalo and Welkner (2008)
Infiernillo	6852000	307000	An elongated, tabular body outcropping to the west of the AFS for more than 70 km in NNE orientation. To the west it intrudes the Chañaral Epimetamorphic complex and La Negra Fm., Punta del Cobre Fm. to the west	Dt (Px + Amp) Gdt (Amp + Bt $\pm$ Px)	131-129	Arévalo and Welkner (2008) Arévalo et al. (2009) Welkner et al. (2006)
La Jaula Diorite	6866400	333000	A group of irregular bodies of limited extension that intrude La Higuera plutonic complex to the south	Dt (Px + Amp)	128	Arévalo and Welkner (2008)
El Trapiche	6735000	295000	Tabular, NNE elongated body composed of three tabular units. It intrudes the Punta del Cobre Fm. and is in contact with the Agua Grande plutonic complex to the east	Md (Opx + Clpx + Bt) Dt (Opx + Clpx + Amp) Mdqz, Gdt (Bt + Amp)	121-117	Creixell and Arévalos (2009) Arévalos and Creixell (2009)

Jilguero Granodiorite	6833000	339000	Small, elongated, NS oriented body that intrudes the Punta del Cobre and Totoralillo Fms.	Gdt, Tn (Amp + Bt)	93	Arévalo et al. (2009)
Camarones	6818000	332000	Composed, lenticular bodies of limited outcropping extension (8 km^2), which intrude the Punta del Cobre, Nantoco and Totoralillo Fms.	Gdt (Bt + Amp) Dt (Amp + Px)	96-91	Arévalo et al. (2009)

Notes: UTM coordinates according to Datum WGS84, Zone 19S. Main rock types from: Emparan and Pineda (2000), Welkner et al. (2006), Arévalo and Welkner (2008), Vivallo et al. (2008), Arévalo and Creixell (2009), Arévalo et al. (2009), Creixell and Arévalos (2009), Arredondo et al. (2017).
Abbreviations: Qz, quartz; Alkfs, alkali feldespars; Pl, plagioclase; Px, pyroxene; Amp, amphibole; Bt, biotite; Msc, muscovite; Opx, orthopyroxene; Clpx, clinopyroxene; Mg, monzogranite; Sg, sienogranite; Gn, granite; Gdt, granodiorite; Tn, tonalite; Dt, diorite; Gb, gabbro; Dqz, quartz diorite; Md, monzodiorite; Mqz, quartz monzonite; Mdqz, quartz monzodiorite.

Supplementary Table 2. Sample location, main characteristics and weighted average $^{206}Pb/^{238}U$ age for the studied plutonic complexes.

Sample ID	UTM Location N	E	Plutonic Complexes	Lithology	Textures	Modal composition (%) Qz-Kfeld-Plg-Px-Amp-Bt-Ms	Zircon U-Pb age (Ma) (MSWD; n)
JJJD_68	6881928	288087	Carrizal Bajo	Mg (Msc + Bt)	Faneritic, inequigranular, euhedral to anhedral (~2 mm, up to 10)	35-20-30-a-3-7-5	215.7 ± 0.8 (0.77; 28)
JJJD_69*	6846509	282040		Dt / Dqz (Amp ± Px ± Bt)	Faneritic, inequigranular, euhedral to subhedral (~5 mm, up to 50)	3-7-55-<5-30-<3-a	210.0 ± 0.9 (0.20; 14)
JJJD_65*	6889940	294312		Dqz (Amp + Bt)	Faneritic, inequigranular, euhedral to subhedral (~5 mm, up to 20)	10-5-45-a-15-25-a	208.0 ± 0.8 (0.99; 19)
JJJD_64	6887240	294983	Algodones Granite	Mg (Amp + Bt)	Faneritic, inequigranular, euhedral (~5 mm, 30 to 5)	35-18-30-a-7-10-a	197.4 ± 0.7 (0.29; 43)
JJJD_71*	6858886	304334	Capote Granodiorite	Gdt (Bt + Amp)	Faneritic, inequigranular, subhedral to anhedral (~3 mm, 10 to < 1)	20-5-40-<3-12-20-a	197.3 ± 0.6 (0.70; 53)
JJJD_73*	6859399	305264		Gdt (Bt + Amp)	Faneritic, inequigranular, euhedral to anhedral (~5 mm, 15 to < 2)	20-3-40-<3-15-20-a	190.8 ± 0.7 (0.19; 43)
JJJD_43*	6714881	276743	Dioritic intrusions, north of La Serena city	Mdqz (Amp + Bt + Px)	Seriated, euhedral to subhedral (~1 mm, 15 to < 0.5 mm)	5-16-37-7-20-15-a	155.1 ± 0.6 (0.55; 31)
JJJD_44	6714881	276743		Mdqz (Amp + Px + Bt)	Faneritic, equigranular, subhedral (~0.5 mm)	5-15-35-10-25-10-a	151.0 ± 0.8 (0.54; 32)
JJJD_41*	6705477	280738		Dqz (Amp + Bt ± Px)	Faneritic, inequigranular, subhedral to anhedral (~0.5 mm, 5 to < 0.2)	3-<3-40-5-30-20-a	120.6 ± 0.7 (0.64; 45)
JJJD_59*	6884433	312480	San Antonio Diorite	Dt (Px + Amp)	Faneritic, inequigranular, euhedral to anhedral (~5 mm, 15 to < 1)	<3-a-55-20-20-<3-a	146.2 ± 1.6 (0.28; 20)
JJJD_70*	6852201	305182	Infiernillo	Gdt (Amp + Bt)	Faneritic, inequigranular, euhedral to anhedral (~2 mm, 10 to < 0.5)	25-15-30-<1-12-18-a	136.3 ± 0.7 (0.76; 30)
JJJD_57*	6876286	320753		Gdt (Amp + Bt ± Px)	Faneritic, inequigranular, euhedral to subhedral (~1 mm, 5 to < 0.2)	18-10-30-<3-20-20-a	128.4 ± 1.1 (0.38; 29)
JJJD_56*	6866336	332867	La Jaula Diorite	Gdt (Amp + Px)	Faneritic, inequigranular, subhedral (~10 mm, 30 to < 1)	23-15-47-5-10-a-a	127.2 ± 0.8 (0.37; 31)
JJJD_48	6742145	288393	El Trapiche	Gdt (Bt + Amp)	Seriated, euhedral to anhedral (~3 mm, 10 to < 0.5 mm)	20-20-25-a-15-20-a	117.1 ± 0.5 (1.2; 33)
JJJD_47*	6742145	288393		Mg (Bt + Amp)	Faneritic, equigranular, euhedral to anhedral (~5 mm)	23-20-25-a-12-20-a	115.9 ± 1.2 (0.15; 35)
JJJD_55*	6836763	339725	Jilguero Granodiorite	Gdt (Amp + Bt)	Faneritic, inequigranular, euhedral to subhedral (~2 mm, 20 to < 0.5)	25-15-35-a-15-10-a	95.9 ± 1.3 (0.37; 9)
JJJD_77	6820818	327209	Camarones	Dt (Amp + Bt + Px)	Faneritic, inequigranular, euhedral to subhedral (~15 mm, 30 to < 5)	10-3-40-12-20-15-a	97.3 ± 0.7 (0.20; 27)
JJJD_78	6820818	327209		Gdt (Bt + Amp)	Seriated, euhedral to anhedral (~1	18-10-37-a-15-20-a	97.3 ± 0.5

				mm, 5 to < 0.2 mm)		(0.33; 35)
JJJD_76*	6820818	327209	Gdt (Bt + Amp)	Faneritic, inequigranular, euhedral to subhedral (~5 mm, 15 to < 1)	30-25-35-a-5-15-a	96.2 ± 1.7 (0.24; 31)
JJJD_79	6820818	327209	Gdt (Bt + Amp)	Faneritic, equigranular, euhedral to subhedral (~10 mm, 20 to < 2)	20-10-35-a-15-20-a	95.1 ± 0.4 (0.15; 34)
JJJD_54	6815405	326156	Gdt (Bt + Amp)	Faneritic, inequigranular, euhedral to subhedral (~15 mm, 25 to < 5)	22-13-35-a-10-20-a	94.8 ± 1.2 (1.5; 23)

*: Indicates samples analyzed for zircon U-Pb geochronology/trace element and whole-rock geochemistry.

Abbreviations: Qz, quartz; Alkfs, alkali feldespars; Pl, plagioclase; Px, pyroxene; Amp, amphibole; Bt, biotite; Msc, muscovite; Opx, orthopyroxene; Clpx, clinopyroxene; Mg, monzogranite; Sg, sienogranite; Gn, granite; Gdt, granodiorite; Tn, tonalite; Dt, diorite; Gb, gabbro; Dqz, quartz diorite; Md, monzodiorite; Mqz, quartz monzonite; Mdqz, quartz monzodiorite. a: absent.

Supplementary Figure 1.

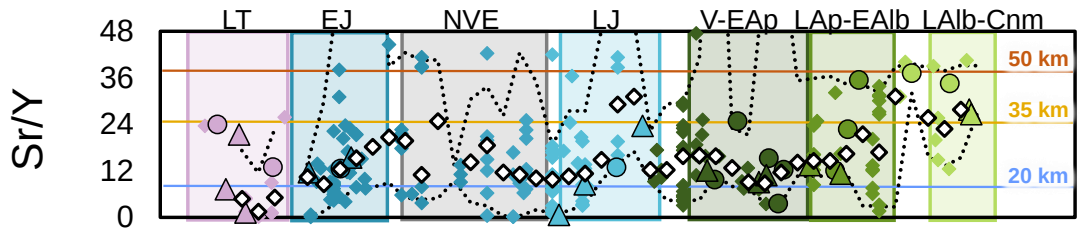

SM2. Supplementary Data 1 (SD1)

Zircon U-Pb geochronology and trace element data, Jara et al. (submitted)
Zircon U-Pb geochronology and trace element data, this study
Whole-rock geochemistry data, Jara et al. (submitted)
Whole-rock geochemistry data, this study

This supplementary material is in a spreadsheet.

SM3. Supplementary Data 2 (SD2)

Compiled dataset of radiometric ages for intrusive rocks from the study area

This supplementary material is in a spreadsheet.

SM4. Supplementary Data 3 (SD3)

Compiled dataset of whole-rock analyses for intrusive rocks from the Coastal Cordillera of Chile

This supplementary material is in a spreadsheet.